Astronomy Reports, Vol. 49, No. 5, 2005, pp. 343–353. Translated from Astronomicheskiĭ Zhurnal, Vol. 82, No. 5, 2005, pp. 387–397.

The Object CSL-1 as an Effect of Projection

M. V. Sazhin and O. S. Khovanskaya

Sternberg Astronomical Institute, Universitetskiĭ pr. 13, Moscow, 119992 Russia

Received April 23, 2004; in final form, December 3, 2004

Abstract—We discuss possible interpretations of the extragalactic double galaxy CSL-1. CSL-1 can be explained either as the projection of two morphologically identical galaxies or as the effect of gravitational lensing by a cosmic string. We discuss the first of these possibilities in detail. More accurate observations will enable unambiguous conclusions about the nature of CSL-1. © *2005 Pleiades Publishing, Inc.*

1. THE OBSERVED FEATURES OF CSL-1

The object CSL-1 (Capodimonte–Sternberg Lens candidate No. 1) was discovered in the course of a deep survey by the Capodimonte Observatory (further OACDF, Osservatorio Astronomico di Capodimonte Deep Field).

The OACDF is a deep image of a 0.5×1 square-degree area of sky at a high Galactic latitude taken in various filters [1] with the 3.5 m NTT telescope of the European Southern Observatory (ESO, La Silla, Chile). The object CSL-1 was imaged in ten filters using the NTT: the three standard broadband filters—B (blue), V (visual), and R (red)—and seven narrow-band filters, at 753, 770, 791, 815, 837, 884, and 914 nm. Later, the 3.5 m National Galileo Telescope (TNG, Canaries) was used to obtain additional images of CSL-1 in the infrared H filter (1.6 μm). The characteristics of the OACDF are presented in [1, 2]. CSL-1 is discussed by Sazhin *et al.* [3].

CSL-1 consists of two giant, slightly elliptical galaxies with absolute magnitudes $M_R = -22.3 \pm 0.1$ and the same redshift, $z = 0.46 \pm 0.008$; it could in principle correspond to a single galaxy with these properties, together with an image created by a gravitational lens. The distance from the solar system's baricenter to CSL-1 is about 1900 Mpc for a Hubble constant of $H = 65$ km s^{-1} Mpc^{-1}. The apparent angular separation of the two components is small, about 20 kpc ($1.9''$). Though the object belongs to a scattered cluster of galaxies, the field is quite sparse: other objects are located from tens of arcseconds to several arcminutes away on the sky (Fig. 1).

The appearance (the presence of metallic absorption lines) and the slope of the spectra clearly indicate that both components correspond to elliptical galaxies with redshift $z = 0.46 \pm 0.008$ (Fig. 2). The left panel of Fig. 2 shows the spectra of the CSL-1 components taken with the TNG telescope (for ease of presentation, the spectra have been shifted relative to each other along the vertical axis); the right panel shows the same for the NTT. The spikes in the spectra are due to bad pixels on the CCD chip.

The TNG spectra were taken under non-photometric conditions, and the correlation coefficient is about 0.6. The NTT observations taken under photometric conditions demonstrate that the two spectra of the CSL-1 components are strongly correlated. The correlation coefficient for the raw spectra is 0.9771 for a sample of one thousand data points. After the reduction of the spectra, the correlation coefficient was 0.8452 (Fig. 3). The spectra were background-reduced: since the two objects are both elliptical galaxies their spectra should have essentially identical slopes, and so a linear fit of one spectrum to the other was undertaken in order to remove errors due to errors in the CCD detector. The differences between the reduced spectra represent random noise without a determinate component, with the autocorrelation function being close to unity (Fig. 4). This difference corresponds to a non-Gaussian random distribution.

The width of the correlation peak corresponds to chaotic velocities of about 400 km/s in the galaxies. The radial-velocity difference is 27 ± 25 km/s.

One hypothesis that has been suggested to explain the existence of these two close images with very similar spectra is that a dust lane with a special hour-glass shape crosses the minor diameter of a single giant, very elliptical galaxy. This dust lane mimics the appearance of two separate objects with virtually undistorted round isophotes.

The two CSL-1 component galaxies have low ellipticity, so that their brightness-distribution isophotes can be approximated well by a two-dimensional de Vaucouleurs law [4]:

$$I_S(r) = I_0 \exp\left[-b\left(\frac{r}{r_c}\right)^{1/4}\right],$$

1063-7729/05/4905-0343$26.00

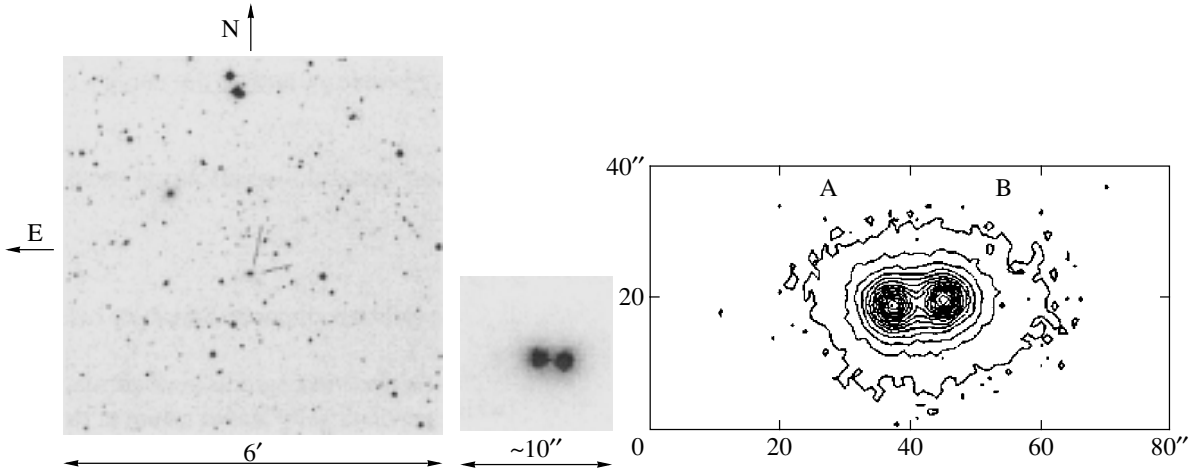

Fig. 1. The object CSL-1 in the R filter (to the left and in the middle). The distance between the brightness centers of the two components is 1.9″. One pixel of the image corresponds to 0.238″, and the resolution is about 1″. The photometric accuracy is 10%. Each of the components is a slightly elliptical giant galaxy with redshift $z = 0.46 \pm 0.008$ and absolute magnitude $M_R = -22.3 \pm 0.1$. The right panel shows the isophotes of CSL-1 in the 914 nm filter, i.e., sections of the 3D brightness distribution with reference surfaces separated by a given brightness difference. The brightness profile of CFL-1 agrees with a de Vaucouleurs law.

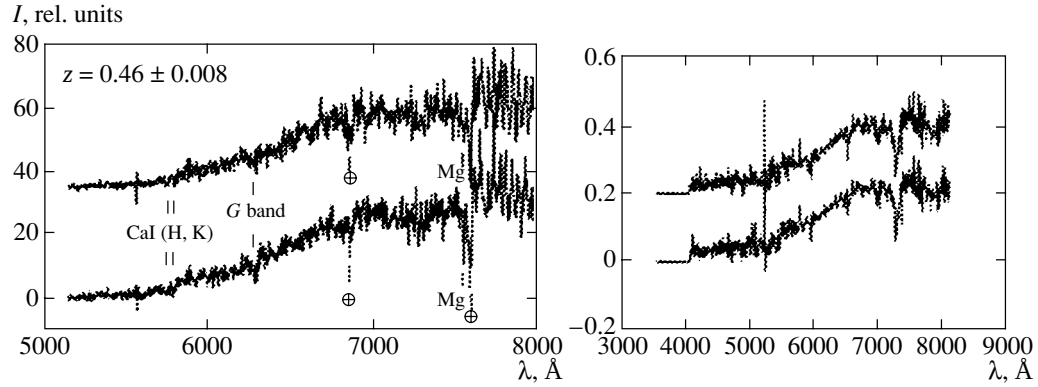

Fig. 2. Left: the TNG spectra of the components of CSL-1. The spectra have been arbitrarily shifted relative to one another for ease of presentation. Absorption lines of calcium, the G band due to metals in galaxies, night-sky lines (telluric absorption lines), and a magnesium line are evident. The lines and the slope of the spectra unambiguously show that both components are elliptical galaxies with redshift $z = 0.46 \pm 0.008$. The spikes in the spectra are due to bad pixels of the CCD chip. Right: the NTT spectra of the components.

where

$$r = \left(\frac{1+e}{2}(x^2+y^2) + \frac{1-e}{2}(x^2+y^2)\cos 2\psi + \frac{1-e}{2}xy\sin 2\psi\right)^{1/2},$$

x and y are curvilinear coordinates with their origin at the central peak of the brightness distribution, e is the eccentricity of the corresponding isophote, and ψ indicates the position angle of the isophote. This model represents the best approximation to the brightness distribution of CSL-1 [3].

It was demonstrated in [3] that modeling the dust with the extinction law characteristic of our Galaxy gave results that disagreed with the observations. The extinction law was assumed to have the form $\exp(-\tau(x))$, where x is the coordinate along the profile and the extinction coefficient is

$$\tau(x) = f(x)/\lambda^n,$$

where $f(x)$ is a geometric factor describing the distribution of dust at a given point x and n is the dust index [5–9], which assumes values in the interval [1, 2].

If an extended galaxy were crossed by a dust lane having this extinction law, a brightness peak in the infrared would have been observed between the centers of the two components of CSL-1, since the dust extinction coefficient, which is inversely proportional to the wavelength to the nth power ($n \in [1, 2]$), is small

Parameters of the CSL-1 components in various filters

Filter	FWHM, arcsec			M_A	M_B	r_e^A	r_e^A/r_e^B
	A	B	PSF				
B	1.59	1.67	1.14	22.73 ± 0.15	22.57 ± 0.15		
V	1.59	1.67	1.01	20.95 ± 0.13	21.05 ± 0.13	6.3	1.4
R	1.98	1.98	0.98	19.67 ± 0.20	19.66 ± 0.20	3.0	2.5
H	1.19	1.11	0.85				
753 nm	1.11	1.19	0.87				
770 nm	1.27	1.27	0.86			7.4	0.6
791 nm	1.67	1.59	0.97				
914 nm	1.27	1.27	0.79			8.8	1.4

in the infrared, so that the dust is transparent at these wavelengths. In fact, a gap is observed between the two components of CSL-1, indicating the presence of two separate objects rather than a single, strongly elliptical galaxy.

There are various models for the dust, however. For example, a possible dust lane in the galaxy NGC 2841 was considered in [10]; this lane is bright in the optical due to the reflection of light from the galaxy's central region, whereas it is dark in the infrared. Nevertheless, the extinction coefficient depends on the wavelength in all models. Figure 5 presents cross sections of the three-dimensional intensity distribution for the CSL-1 components at 915, 837, 815, 791, 770, and 753 nm and in the R, V, and B filters. The sections pass through the brightness maxima of the two components. We can see that, for the given photometric accuracy (10%), the order of the intensity minima in the various filters is the same as the order of the corresponding maxima. If we normalize each profile so that the highest intensity in each filter is equal to unity (Fig. 6), the minima have the same depth, and hence are frequency-independent. This enables us to rule out the dust-lane hypothesis.

Let us consider the observed properties of CSL-1.

The table presents the observed parameters for the components of CSL-1. It is important that CSL-1 is resolved. Since the uncertainty of a Gaussian function is 1%, the difference between the telescope's resolving power (the point-spread function, PSF) and the full width at half maximum FWHM for CSL-1 is significant (see the table). The columns of the table list (1) the eight filters used for the observations, (2) and (3) the FWHMs for the two components, (4) the FWHM for the PSF in the field of CSL-1, (5) and (6) the absolute magnitudes of the components, (7) the radius of the brighter component, and (8) the ratio of the component radii. A characteristic feature of CSL-1 is the presence of undistorted isophotes for the resolved images in all the filters available for the OACDF (Fig. 1, the 914 nm filter).

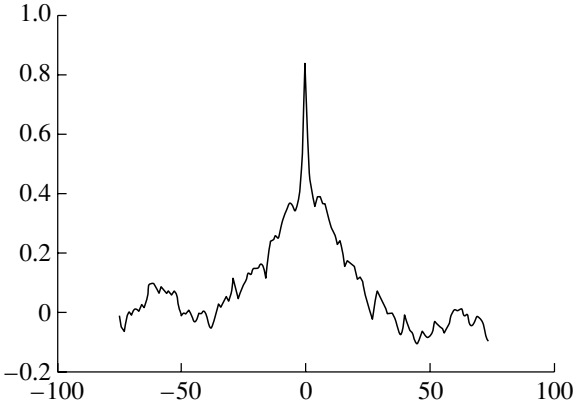

Fig. 3. Correlation coefficient for the NTT spectra of the components of CSL-1. The width of the correlation peak corresponds to chaotic velocities of about 400 km/s in the galaxies.

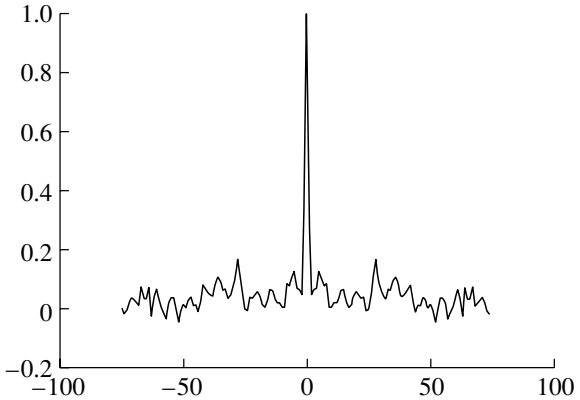

Fig. 4. Autocorrelation function for the difference of the reduced spectra of the CSL-1 components.

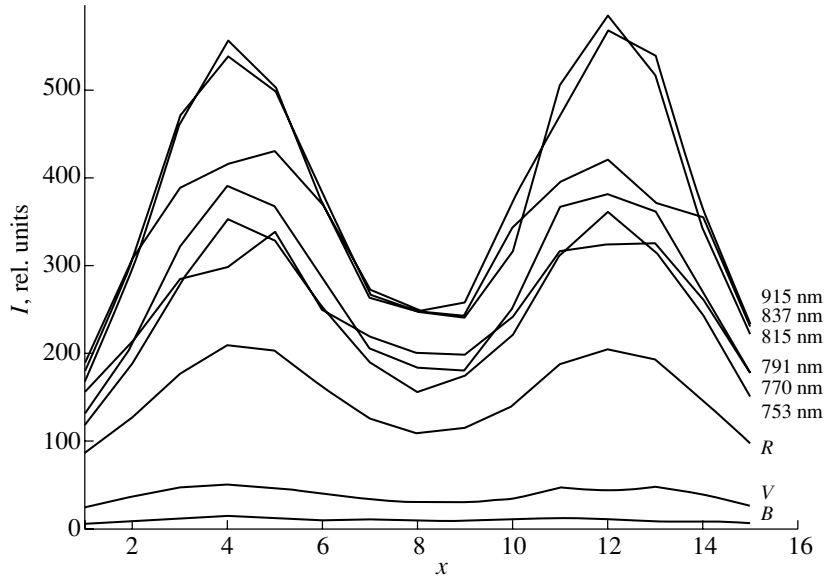

Fig. 5. Cross sections of the three-dimensional intensity distributions of the CSL-1 components at 915, 837, 815, 791, 770, and 753 nm and in the R, V, and B filters. The cross sections pass through the intensity maxima for the two components. With the given photometric accuracy, 10%, the order of the intensity minima in the various filters is the same as the order of the maxima.

Let us summarize the main characteristics of CSL-1.

1. CSL-1 is a double extended source with resolved components having the same morphology: a bright center surrounded by a halo with undistorted, almost circular isophotes.

2. The two components have the same magnitudes and colors. The two images are similar in all the filters available for the Capodimonte Observatory deep survey: B (blue), V (visual), R (red), H (infrared, 1.6 μm) and 753, 770, 791, 815, 837, 884, and 914 nm.

3. The two components have the same redshift, $z = 0.46 \pm 0.008$, derived from two independent observations with the TNG and NTT telescopes.

4. The spectra of the two images are the same at a confidence level exceeding 99.999%.

2. PROJECTION

According to [3], the nature of an object such as CSL-1, having the properties described above, can be explained in two ways, based on fundamentally different physical mechanisms.

The first possibility is that CSL-1 is formed due to the lensing of a single, slightly elliptical giant galaxy by a cosmic string—a linear topological defect of space-time widely discussed in theoretical cosmology [11–15].

The small angular distance between the two components, the similarity of the images in all the available filters, and the similarity of the spectra suggest that CSL-1 may be a gravitationally lensed object. The undistorted isophotes of the resolved image of CSL-1 provide evidence for gravitational lensing specifically by a cosmic string [3]. However, this question needs a specialized and deep analysis that is beyond the scope of this paper.

The second possibility, which we will discuss in detail, is the following.

We may be observing two different elliptical galaxies, that have very similar morphologies and spectra. The angular distance between these galaxies projected onto the plane of the sky corresponds to 20 kpc, whereas the physical distance between the galaxies could be larger, since we observe no distortion of the isophotes suggestive of interaction. In addition, to avoid gravitational lensing of one of the galaxies by the other, we must limit the maximum distance between the galaxies: the larger this distance, the larger should be the distortion of the background galaxy's isophotes due to gravitational lensing of the more distant galaxy by the foreground galaxy.

Thus, the physical distance between the two galaxies should lie in some interval, $[L_1, L_2]$. It is possible to estimate these limits.

2.1. Tidal Interaction of the Components

Consider two isolated low-ellipticity, gravitationally interacting galaxies. The evolution of such a system has been analyzed in the literature many times, with the most correct approach being the numerical solution of the n-body problem. Note, however, that

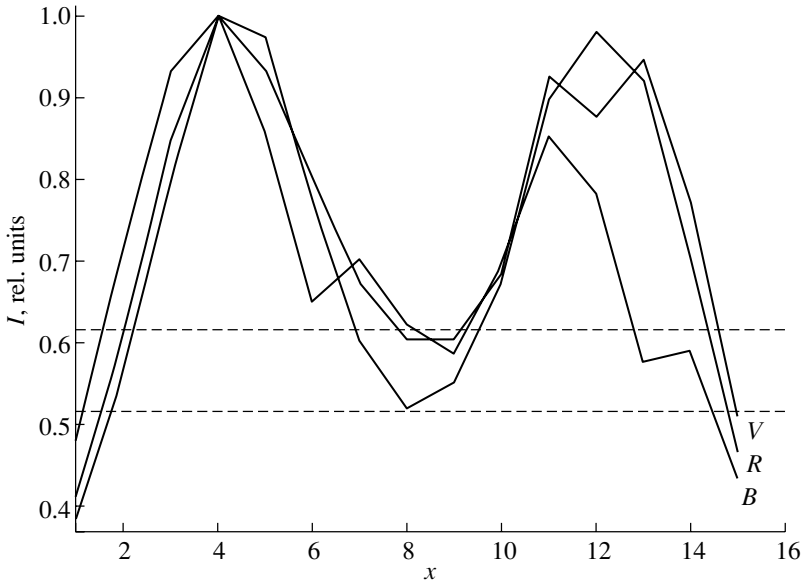

Fig. 6. Brightness profiles for the B, R, and V filters normalized so that the maximum intensity in each of the filters is equal to unity. The interval between the dashed lines corresponds to the 10% photometric accuracy. The minima are equally deep, and hence frequency-independent.

the masses of the giant elliptical galaxies considered are about $6 \times 10^{11} M_\odot$, i.e., $n \sim 2 \times 6 \times 10^{11} \sim 10^{12}$. The numerical solution of a problem with 10^{12} variables is extremely difficult from the point of view of computational resources and time.

Recent papers (for example, [16]) have considered numerical simulations of interactions between two low-ellipticity galaxies with from $n = 2 \times 10^4$ to $n = 5 \times 10^4$ stars using the NEMO software package, designed to solve the equations describing the gravitational interactions in n-body systems with various initial configurations. The simulation results, as well as observations of interacting elliptical galaxies (see, for instance, [17]), are in agreement with the approximate qualitative method we will use to estimate the galaxies' tidal distortion.

Let us find the minimum distance between two galaxies, L_1, for which the gravitational interaction due to tidal forces is not significant. This means that, if the galaxies are separated by a distance smaller than L_1, a significant distortion of isophotes due to mass transfer will be observed. Whether this distortion is "significant" is determined by the available photometric accuracy of the observations, namely 10%.

We solved this problem using the following model.

Galaxy A, whose tidal distortion due to galaxy B is being studied, is approximately a gaseous sphere with polytropic index n. We will study distortions of the sphere for the simplest case of an incompressible fluid of constant density ($n = 0$) and constant pressure, as well as for the case of variable density that decreases to zero towards the periphery ($n = 4$).

Galaxy A has mass M, density ρ, and pressure $P = P(\rho)$. We assume that both galaxies have low rotational velocities, and so neglect their rotation. This assumption is valid for low-ellipticity galaxies. We do not consider distortions of galaxy B, and so for simplicity replace it with a point mass with mass M' equal to the mass of the galaxy.

With the photometric accuracy of 10%, and having in mind that we wish to estimate only the distance L_1, we neglect the mutual gravitational interactions of the individual stars, which would require a cumbersome numerical solution of an n-body problem. We consider only the condition of hydrostatic equilibrium of galaxy A relative to its center of mass, under the action of its own gravitation with the potential V, the internal pressure of galaxy A, and the tidal force from the point B with the potential V':

$$-\frac{1}{\rho}\frac{dP}{dr} = \frac{d}{dr}\left(V + V' - \frac{GM'}{L^2}x\right).$$

Here, L is the distance between the centers of mass of galaxies A and B. The last term shows that we consider equilibrium at the center of mass of the body A.

If the pressure is constant and density-independent, we obtain the simplest case of hydrostatic equilibrium for an incompressible fluid (a polytrope with index $n = 0$ and constant pressure). The equilibrium condition can be written

$$V + V' - \frac{GM'}{L^2}x = \text{const}. \qquad (1)$$

To within the second-order infinitesimals x/L, y/L, and z/L, the potential of the tidal force, V', is

$$V' = \frac{GM'}{\sqrt{(L-x)^2+y^2+z^2}} \simeq \frac{GM'}{L}\left(1+\frac{x}{L}+\frac{2x^2-y^2-z^2}{2L^2}\right),$$

where x, y, z is an arbitrary point on the equipotential surface of galaxy A.

The equilibrium figure of galaxy A is sought as an ellipsoid of rotation:

$$\frac{x^2}{a^2}+\frac{y^2+z^2}{b^2}=1, \qquad (2)$$

whose minor axis is perpendicular to the line connecting the centers of mass of galaxies A and B. Thus, the potential V of galaxy A should be [18]:

$$V = \text{const} - Px^2 - Qy^2 - Rz^2,$$

$$P = \pi G\rho ab^2 \int_0^\infty \frac{ds}{(a^2+s)^{3/2}(b^2+s)},$$

$$Q = R = \pi G\rho ab^2 \int_0^\infty \frac{ds}{(a^2+s)^{1/2}(b^2+s)^2}.$$

The equilibrium condition requires the equality of the left-hand side of the equipotential-surface equation (1) and the left-hand side of the equation for the surface of the ellipsoid of rotation (2):

$$x^2\left(P-\frac{GM'}{L^3}\right)+(y^2+z^2)\left(Q+\frac{GM'}{2L^3}\right) = \frac{x^2}{a^2}+\frac{y^2+z^2}{b^2}.$$

Equating the expressions for corresponding variables in the left-hand and right-hand sides of the equation yields

$$\left(\frac{a}{b}\right)^2 = \frac{Q+GM'/2L^3}{P-GM'/L^3}. \qquad (3)$$

For an approximate computation of the integrals in the expressions for P and Q, let us define the semiaxes of the distorted ellipsoid A as $a = R+\delta R$, $b = R-\delta R$, where $x = \delta R/R \ll 1$ is the relative distortion of galaxy A relative to its spherically symmetrical configuration. The significance of the distortion x is determined using the photometric accuracy: $x = 0.1$. Thus, Eq. (3) defining the relation between the relative distortion x and the distance L between the centers of mass of galaxies A and B can be rewritten

$$\left(\frac{1+x}{1-x}\right)^2 = \frac{\frac{1}{2}+\frac{2}{5}x-\frac{4}{35}x^2+\left(\frac{R}{L}\right)^3\frac{1}{2}\frac{M'}{M}}{\frac{1}{2}-\frac{4}{5}x+\frac{8}{35}x^2-\left(\frac{R}{L}\right)^3\frac{M'}{M}}.$$

Transforming the last expression and keeping terms to second-order in infinitesimals of x, we obtain

$$\frac{R}{L} \simeq \left(\frac{M}{M'}\right)^{1/3}(0.81x^{1/3}-0.33x^{4/3}).$$

If the pressure is a function of density of the form $P = P(\rho) = \text{const}\Theta^{n+1}$, $\rho = \Theta^n$ (a polytropic Lane–Emden sphere [19]), then, generally speaking, the equilibrium configuration does not coincide with the ellipsoid of rotation, and is pear-shaped. A similar situation was considered in detail by Krat [20]. The largest relative deviation from a spherically symmetric configuration is

$$x = \frac{M'}{M}\left[\Delta_2\left(\frac{R}{L}\right)^3+\Delta_3\left(\frac{R}{L}\right)^4+\Delta_4\left(\frac{R}{L}\right)^5\right],$$

where Δ_2, Δ_3, and Δ_4 are numerical constants that are equal to unity to the second figure after the decimal point.

Thus, two extreme possibilities for the relation between pressure and density have been considered using the polytrope model: an incompressible fluid and a large polytropic index. The actual behavior of interacting galaxies is expected to be between these two extremes, whose differences are insignificant.

Figure 7 shows the dependence of the total relative distortion of galaxy A on the distance between galaxies A and B, in units of the radius of galaxy A. The total distortion is due to both tidal forces and gravitational lensing of galaxy A by galaxy B, the effect to be considered below. It is clear that the main contribution at small distances between the galaxies comes from the tidal forces. On larger scales, the effect of gravitational lensing begins to dominate. The left side of the graph displays the contribution of the tidal forces to the total distortion.

Given the observed properties of CSL-1, we assumed equal masses for the two galaxies. The relative distortion by tidal forces is inversely proportional to the cube of the distance between the galaxies, and becomes significant only at distances comparable to the galaxy's undistorted radius.

Thus, for $x = 0.1$, the lower limit $L = L_1$ of the desired distance range is about 30 kpc. Obviously, this distance will grow as $x^{-1/3}$ as the photometric accuracy improves. For example, for $x = 0.01$, $L_1 = 57$ kpc, and for $x = 0.001$, $L_1 = 123$ kpc.

This model enables us to obtain an approximate, qualitatively correct estimate of the behavior of low-ellipticity interacting galaxies, which is confirmed by numerical simulations [16] of tidal interactions between two low-ellipticity galaxies containing about 10^4 gravitationally interacting bodies (Fig. 8).

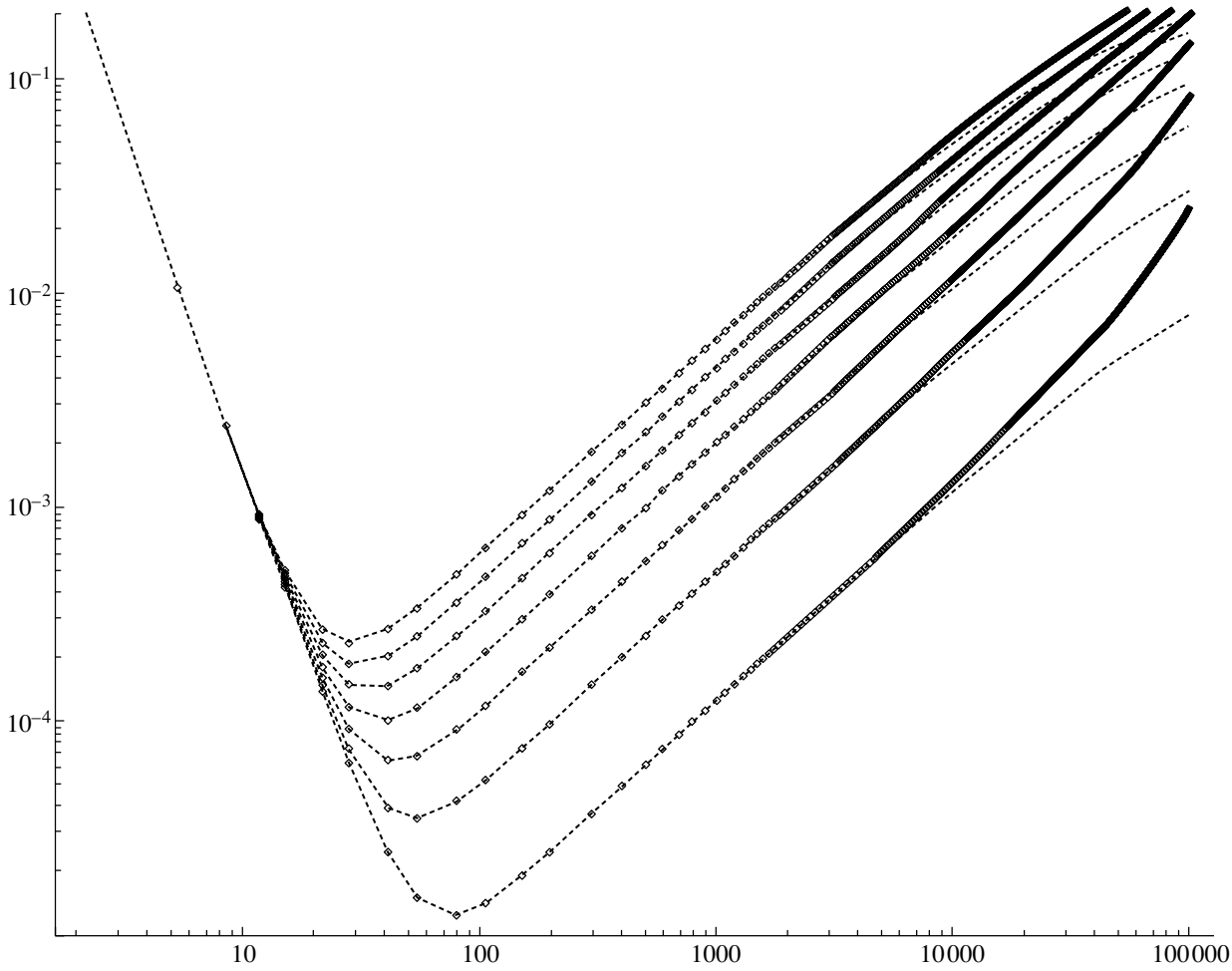

Fig. 7. Relation between the total relative distortion of galaxy A and the distance between galaxies A and B, expressed in units of the radius of galaxy A. For ease of presentation, we show seven graphs for different galaxy masses corresponding to virial velocities (from top to bottom) of $v = 700$, 600, 500, 400, 300, 200, and 100 km/s. The main contribution at small distances between the galaxies is from tidal forces. The plot is for a polytrope model with index $n = 4$. For larger distances, the main contribution is from gravitational lensing. The solid curves are for the case $D_d = 1.9 \times 10^9$ pc, and the dotted curves are for $D_d + L_2 = 1.9 \times 10^9$ pc. The distance between the galaxies corresponding to minimum relative distortion decreases with increasing mass.

2.2. Gravitational Lensing of a Component by Its Companion

Let us now derive the largest possible distance between the galaxies, L_2, from the condition that, within the given photometric accuracy, we observe no distortions due to the gravitational lensing of the more distant galaxy by the closer galaxy.

We introduce the following notation [21]:

M is the mass of the lensing galaxy (the gravitational lens);

D_{ds} is the distance from the lens to the lensed background galaxy;

D_d is the distance from the lens to the solar system's baricenter;

θ is the angle between the directions toward the lens and the true position of the lensed background galaxy;

θ_1 is the angle between the directions toward the lens and the position of the brighter image of the background galaxy;

θ_0 is the angular size of the Einstein–Chwolson cone.

The angles θ, θ_1, and θ_0 are related as $\theta_1 = 1/2(\theta + \sqrt{\theta^2 + 4\theta_0^2})$. The size of the Einstein–Chwolson cone is

$$\theta_0^2 = \frac{4GM}{c^2}\frac{D_{ds}}{(D_{ds} + D_d)D_d}.$$

Let the undistorted configuration of the background galaxy be a sphere of radius R. We assume that the two galaxies have equal masses and that their undistorted configurations have equal radii. If the two galaxies are separated by some distance to be determined, $D_{ds} = L_2$, then the background galaxy

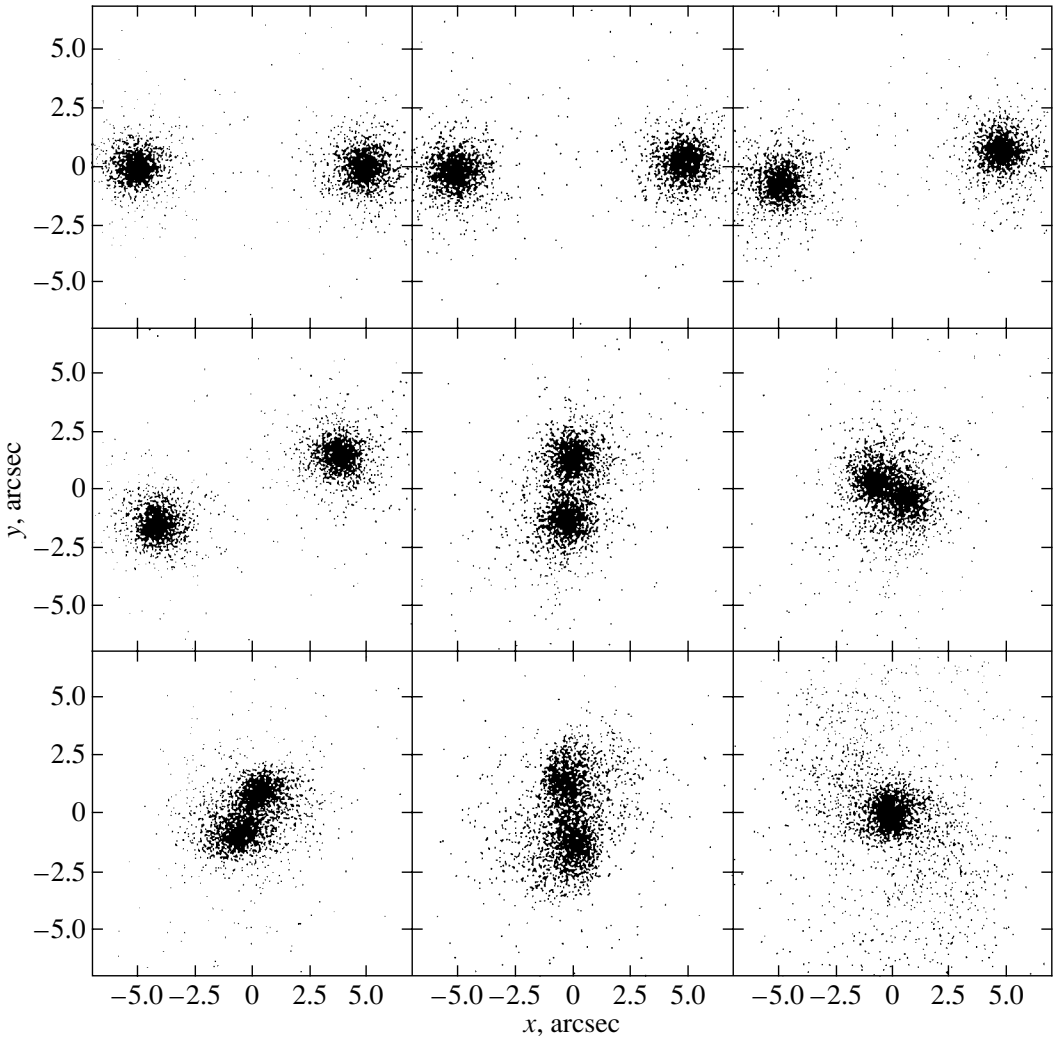

Fig. 8. Numerical simulations of interacting elliptical galaxies.

is subject to gravitational lensing according to the following scheme.

For simplicity, we will assume that the matter in the galaxies is distributed according to a Schwarzschild law; then only two images of the background galaxy will appear, one of them negligibly small and the other virtually coincident with the actual position of the background galaxy. The differences in the positions of the real source and of its image are the following: first, the brightness center of the real source will be displaced by $\theta_1 - \theta$, a value much less than its radius, and second, the image will assume a shape close to that of an ellipsoid of rotation (in the case of small distortions), with its semimajor axis perpendicular to the line connecting the gravitational lens and the background galaxy.

The semimajor axis, a, can be approximately evaluated from the similitude ratio [21]:

$$\frac{\theta}{\theta_1} = \frac{R}{a} \qquad \Longrightarrow \qquad a = \frac{R}{2}\left(1 + \sqrt{1 + \frac{4\theta_0^2}{\theta^2}}\right).$$

To find the semiminor axis, b, we use the condition that lensing maps θ into θ_1, and thus, $\theta + R$ is mapped into

$$\theta_1^+ = 1/2(\theta + R + \sqrt{(\theta + R)^2 + 4\theta_0^2}),$$

and $\theta - R$ is mapped into

$$\theta_1^- = 1/2(\theta - R + \sqrt{(\theta - R)^2 + 4\theta_0^2}).$$

Thus,

$$b = \theta_1^+ - \theta_1^- = R + 1/2\sqrt{(\theta + R)^2 + 4\theta_0^2} - 1/2\sqrt{(\theta - R)^2 + 4\theta_0^2}.$$

For convenience in our further computations, we introduce the function $V(\theta) = \sqrt{\theta^2 + 4\theta_0^2}$. Then,

$$\Delta V = V(\theta + R) - V(\theta - R) \simeq \frac{dV}{d\theta}\Delta\theta = \frac{2R}{\sqrt{1 + 4\theta_0^2/\theta^2}}.$$

Note that $2R \simeq 2'' \simeq 10^{-5}$ and, since $4\theta_0^2/\theta^2 \ll 1$, we have $dV/d\theta \simeq 1$. Thus,

$$b \simeq \frac{1}{2}\left(R + \Delta V/2\right) = \frac{R}{2}\left(1 + (1 + 4\theta_0^2/\theta^2)^{-1/2}\right).$$

We will describe the distortion of the background galaxy's image using the parameter $\delta = (a - b)/a$. Note that $\delta \approx 2x$, where $x = \delta R/R$ is the galaxy's relative distortion introduced in the previous section. Estimating the mass of the lensing galaxy from the virial theorem, we obtain

$$\delta = 1 - \left(1 + \frac{16R}{D_d}\frac{1}{\theta^2}\frac{v^2}{c^2}\frac{1}{1+q}\right)^{-1/2}, q = \frac{D_d}{L_2}.$$

Estimating the value of

$$\frac{16R}{D_d}\frac{1}{\theta^2}\frac{v^2}{c^2}$$

for $v = 400$ km/s [3] (a typical virial velocity of an elliptical galaxy), $R = 10^4$ pc, $D_d = 1.9 \times 10^9$ pc, and $\theta \simeq 10^{-5}$, we obtain

$$\delta \simeq 1 - \left(1 + \frac{1.5}{q+1}\right)^{-1/2}.$$

As in our study of tidal forces, the significance of the relative distortion of the lensed galaxy's isophotes is determined by the observational photometric accuracy, $x = 0.1$. If the distortion exceeds this value, then the last equation will lead to $L_2 \geq D_d/1.6$; i.e., the largest distance between the galaxies should not exceed approximately 1144 Mpc. The largest possible distance between the galaxies rapidly decreases as the photometric accuracy improves. We obtain $L_2 \geq 54$ Mpc for $x = 0.01$ and $L_2 \geq 5$ Mpc for $x = 0.001$.

The right side of the graph in Fig. 7 is the relation between the distance separating the galaxies in units of their radii and the relative distortion due to gravitational lensing.

The dotted line in Fig. 7 is the same relation, but takes into account the fact that the value 1.9×10^9 pc derived from the observations could correspond, not to the distance from the lensing galaxy to the observer, but instead to the distance from the observer to the lensed background galaxy; i.e., $D_d + L_2 = 1.9 \times 10^9$ pc. These two situations cannot be distinguished from the observer's point of view, though, obviously, the galaxies' peculiar velocities should be different in these two cases. In the latter case, the desired distance becomes smaller, being about 519 Mpc for $x = 0.1$, with $L_2 \geq 51$ Mpc for $x = 0.01$ and $L_2 \geq 5$ Mpc for $x = 0.001$.

An additional constraint on the largest possible distance between the two components can be derived based on the two galaxies' peculiar velocities. The redshifts of the two galaxies are the same to within 0.8%, and thus the difference in their peculiar velocities, ΔV, depends on the distance between the galaxies, ΔL, as $\Delta V \approx H\Delta L \leq 1000$ km/s [22]. This gives $\Delta L \leq 15$ Mpc.

2.3. Probability of Projection Effects

If we interpret CSL-1 as a projection effect, a number of constraints for the distance between the component galaxies will follow, as is discussed in detail in the previous sections. If observations with better photometric accuracy or with better angular resolution are available, the permitted interval of distances between the galaxies will become narrower. Two galaxies outside the permitted interval will possess distinctive distortions of their isophotes.

It is important to realize, however, that the derived constraints do not enable us to judge the probability of the presence of two giant, undistorted, low-ellipticity galaxies with strongly correlated spectra and redshifts equal to 0.8% within a single $2'' \times 2''$ field. It is important to estimate this probability: if there are many pairs with such properties in the Universe, this will provide weighty evidence that CSL-1 is the result of a projection effect, rather than the result of gravitational lensing by a cosmic string.

It is known that the sample correlation coefficient of the two spectra is 0.8452 for a sample of one thousand data points. Thus, the spectra are correlated at a significance level, α, that is better than 10^{-200}. The significance level can be evaluated as follows [23].

To estimate the uncertainty of the sample correlation coefficient, r_{xy}, where $x = \{x_i\}$ and $y = \{y_i\}$ ($i = 1...1000$) are the spectra of the two components, we introduce the function

$$w = \frac{1}{2}\ln\frac{1 + r_{xy}}{1 - r_{xy}},$$

whose distribution is approximately normal, with the mean value and dispersion

$$\mu_w = \frac{1}{2}\ln\left(\frac{1 + \rho_{xy}}{1 - \rho_{xy}}\right),$$

$$\sigma_w^2 = \frac{1}{N - 3},$$

where ρ_{xy} is the correlation coefficient of the parent population and $N = 1000$ is the number of elements in the sample. These last relations enable us to derive confidence intervals for the parent population's correlation coefficient from the sample estimate of the correlation coefficient. For the problem at hand, the hypothesis of zero correlation between the spectra is rejected at a significance level better than 10^{-200}.

Thus, the probability that the two galaxies' spectra differ, with a correlation coefficient of $r_{xy} = 0.8452$ for $N = 1000$, is lower than 10^{-200}. Hence, the probability that CSL-1 consists of two physically different galaxies is likewise negligibly small.

We can derive a rough estimate of the mean number of noninteracting pairs of giant elliptical galaxies having spectra with the corresponding high correlation level and separated by an apparent angular distance of $2''$.

The mean number of galaxies in the Universe is $N_{galaxy} = m_{total}/m_{galaxy}$. The total mass of matter in galaxies can be approximated as

$$m_{total} = \frac{4}{3}\pi R_{Univ}^3 \rho_{matter} = \frac{1}{2} d_A^3 \frac{(\Omega_m h^2) H^2}{G},$$

where d_A is the angular diameter distance to the decoupling sphere [24], $\Omega_m h^2$ is the dimensionless matter density, H is the Hubble constant, and G is the gravitational constant. According to current estimates of cosmological parameters, $m_{total} \approx 3.5 \times 10^{56}$ g. The mean mass of a galaxy (excluding dwarf galaxies) is $m_{galaxy} = 10^{11} M_\odot \approx 2 \times 10^{44}$ g. Thus, the number of galaxies is $N_{galaxy} \approx 1.75 \times 10^{12}$. The fraction of giant elliptical galaxies among them is $0.1 \times 21\%$ [25]. The galaxies must also lie within a $2'' \times 2''$ field. The density of elliptical galaxies in such a field is $\approx 3.09 \times (10^{-4} - 10^{-3})$, depending on the particular cosmological model adopted [26]; i.e., the mean number of giant elliptical galaxies (neglecting clustering) in a $2'' \times 2''$ field is

$$N_{eg} \approx 10^8,$$

which yields a number that is much below unity when multiplied by the above probability.

3. CONCLUSION

Observations with higher resolution, for example using the HST, which has an angular resolution of about 40 milliarcseconds, would make it possible to draw unambiguous conclusions about whether we are dealing with a chance projection of two morphologically similar galaxies or with the first observed case of the gravitational lensing of a single galaxy by a cosmic string.

At high resolution, the two galaxies will still have round, undistorted isophotes if they are in the distance range derived for the corresponding photometric accuracy. If the two galaxies are outside this range, distortions of their isophotes will be due either to mutual gravitational effects or to the gravitational lensing of the more distant by the closer galaxy. Clearly, both effects are well understood and can be unambiguously identified from the appearance of the isophote distortions.

Attempts to explain CSL-1 as the projection of two galaxies encounter a number of difficulties: a particular choice of peculiar velocities and distances between the galaxies is needed to avoid mass transfer and to have no significant gravitational lensing of one galaxy by the other. In addition, the probability of the configuration required for such a projection effect is extremely low.

ACKNOWLEDGMENTS

The authors thank Dr. O.K. Sil'chenko for fruitful discussions and a number of helpful comments. This study was supported by the Russian Foundation for Basic Research (project no. 04-02-17288).

REFERENCES

1. M. Capaccioli *et al.*, ESO Press Release 15a-f/01 (2001); http://www.eso.org/outreach/press-rel/pr-2001/phot-15-01.html.
2. M. Capaccioli, J. M. Alcala, M. Radovich, *et al.*, in *Survey and Other Telescope Technologies and Discoveries* (Waikoloa, Hawaii, 2002), Proc. SPIE, p. 406.
3. M. Sazhin, G. Longo, M. Capaccioli, *et al.*, Mon. Not. R. Astron. Soc. **343**, 353 (2003).
4. G. de Vaucouleurs, Ann. Astrophys. **11**, 247 (1948).
5. S. B. Pikel'ner and S. A. Kaplan, *Physics of Interstellar Medium* (Nauka, Moscow, 1979) [in Russian].
6. R. H. Hildebrand, Quart. J. R. Astron. Soc. **24**, 267 (1983).
7. F. Ferrari, M. G. Pastoriza, F. D. Macchetto, *et al.*, Astron. Astrophys. **389**, 355 (2002).
8. R. Chini, P. G. Mezger, E. Kreysa, and H.-P. Gemuend, Astron. Astrophys. **135**, L14 (1984a).
9. R. Chini, P. G. Mezger, E. Kreysa, and H.-P. Gemuend, Astron. Astrophys. **137**, 117 (1984b).
10. D. L. Block *et al.*, Astrophys. J. Lett. **522**, L25 (1999).
11. T. W. Kibble, J. Phys. A: Math. Gen. **9**, 1387 (1976).
12. Ya. B. Zeldovich, Mon. Not. R. Astron. Soc. **192**, 663 (1980).
13. A. Vilenkin, Phys. Rev. D **23**, 852 (1981).
14. J. R. Gott III, Astrophys. J. **288**, 422 (1985).

15. A. Dolgov, M. Sazhin, and Ya. Zeldovich, *Basics of Modern Cosmology* (Editions Frontieres, Gif-sur-Yvette, 1990).
16. E. A. Evstigneeva, V. P. Reshetnikov, and N. Ya. Sotnikova, in *JENAM-2000, Morphology and Dynamics of Stellar Systems: Stellar Clusters, Galactic Arms and Rings* (Moscow, 2000).
17. P. G. van Dokkum, S. A. Stanford, B. P. Holden, *et al.*, Astrophys. J. Lett. **552**, L101 (2001).
18. G. N. Duboshin, *Celestial Mechanics. Main Problems and Methods* (Nauka, Moscow, 1975) [in Russian].
19. Ya. B. Zel'dovich and I. D. Novikov, *Gravitational Theory and Stellar Evolution* (Nauka, Moscow, 1971) [in Russian].
20. V. A. Krat, *Equilibrium Figures of Celestial Bodies* (Gostekhizdat, Moscow, 1950) [in Russian].
21. A. Zakharov and M. Sazhin, Usp. Fiz. Nauk **168**, 1041 (1998) [Phys. Usp. **41**, 945 (1998)].
22. E. Hawkins, S. Maddox, S. Cole, *et al.*, astro-ph/0212375 v2 (2003).
23. J. S. Bendat and A. G. Piersol, *Random Data. Analysis and Measurement Procedures* (Wiley, New York, 1986; Mir, Moscow, 1989).
24. D. N. Spergel, L. Verde, H. V. Peiris, *et al.*, astro-ph/0302209 v3 (2003).
25. S. R. Folkes, O. Lahav, and S. J. Maddox, Mon. Not. R. Astron. Soc. **283**, 651 (1996).
26. J. P. Gardner, Publ. Astron. Soc. Pac. **110**, 291 (1998).

Translated by N. Samus'

Astronomy Reports, Vol. 49, No. 5, 2005, pp. 354–361. Translated from Astronomicheskiĭ Zhurnal, Vol. 82, No. 5, 2005, pp. 398–406.

Corotation Resonance and the Radial Distribution of Oxygen in a Spiral Galaxy

I. A. Acharova[1], J. R. D. Lépine[2], and Yu. N. Mishurov[1]

[1] *Department of Space Research, Rostov State University, Zorge street 5, Rostov-on-Don, 344090 Russia*

[2] *Instituto de Astronomia, Geofisica e Ciéncias Atmosféricas, Universidade de São Paolo, Cidade Universitaria, São Paolo, SP, Brazil*

Received March 5, 2004; in final form, December 3, 2004

Abstract—A theory is proposed for the formation of the bimodal radial distribution of oxygen in the Galaxy, which displays a steep abundance gradient in the inner region and becomes flat in the middle and outer regions. The formation of this structure is associated with the following effects. First, type II supernovae, which are sources of oxygen, are concentrated in the spiral arms. Second, the enrichment rate is proportional to the rate at which a chemical element enters the spiral arm, which has the form of a density wave. This implies that the rate of oxygen production is substantially suppressed in most of the corotation circle due to the low relative velocity of the Galactic material with respect to the spiral arms and the low rate at which the arms are crossed by the Galactic material. Third, the corotation radius is near the Sun. The net result of these effects combined with turbulent diffusion is the development of the structure discussed in the paper. © *2005 Pleiades Publishing, Inc.*

1. INTRODUCTION

The distribution of chemical elements in the Galaxy provides important clues to its structure and evolution. Various means have been devised to determine the origin of the global radial abundance gradient in the Galactic disk (see, e.g., [1, 2]). At the same time, data concerning various features in the radial distributions of elements in the Galaxy have been published over the last few decades, in particular, with regard to the nonmonotonic gradients of the abundances. Twarog *et al.* [3] were the first to point out such features; earlier, it was assumed that the radial distribution of metallicity in the Galaxy could be described by a simple linear function—see papers cited in [3]. Searches for such characteristic features and their origin can constrain classes of models for the Galactic synthesis of heavy elements.

In this paper, we consider the bimodal distribution of heavy elements with Galactocentric distance r found by Andrievsky *et al.* [4] in their analysis of Cepheid abundances. In their latest paper, which, like [4], was based on detailed spectroscopic analysis and not on photometric indices, Andrievsky *et al.* [5] showed that this bimodal structure is clearly discernible in the distributions of various elements. The distributions display a fairly steep negative gradient in the inner part of the disk for r smaller than about 7 kpc and are flat in the outer regions out to 10–11 kpc (we will take the solar Galactocentric distance to be 8.5 kpc, as was recommended by the IAU, although many studies have suggested a much shorter Galactic distance scale). It is this structure that we analyze here.

We also use the observational data for planetary nebulae of Maciel and Quireza [6], who concluded that the radial distribution of oxygen in the Galaxy has a minimum near the Sun.

We will focus on oxygen. It goes without saying that the most complete information—including information about the time variability—can be obtained only by analyzing the evolution of all elements together. However, iron and oxygen remain the only elements to have more or less consistent estimates of their production in stars [1, 7]. We chose to study oxygen for the following reasons. Many authors have suggested that the spiral arms of the Galaxy affect the synthesis of heavy elements (see, e.g., [2]). Oort [8] was possibly the first to point this out. Since then, various authors have developed this idea (e.g., in our previous paper [9], we allowed for the effect of the closeness of the corotation resonance to the solar circle on the asymptotic metallicity distribution). Type II supernovae (SNII) are now believed to be the main source of oxygen (see, e.g., [1]), and these stars are known to be concentrated in the spiral arms [10] and to have asymmetric distributions across the arms characteristic of a Galactic shock [11], further supporting the close association between SNII and spiral arms. Moreover, the progenitors of stars of this type have very short lifetimes, implying

1063-7729/05/4905-0354$26.00

that SNII have not moved significantly from their birthplaces. On the other hand, the progenitors of the sources of most of the iron (∼70%)—type Ia supernovae (SNIa)—may be several billion years old (see, e.g., [1, 12], etc.). Even if they were born inside an arm, such objects have had enough time to move far from their birth place. Furthermore, SNIa progenitors can also originate outside spiral arms, and even outside the Galactic disk. Therefore the concentration of SNIa to spiral arms is much less conspicuous, as is evident from the data of Bartunov *et al.* [10]. They occupy a much greater volume around the spiral arms compared to that occupied by HII regions, which, according to [10], show a well-defined spatial correlation with SNII. Thus, given our current understanding of the production of chemical elements in stars, oxygen should be the most accurate indicator of the effect of spiral arms on the chemical evolution of the Galactic disk.

Our aim is to analyze the effect of the spiral arms on the characteristic features of the radial distribution of heavy elements. Therefore, to keep our analysis "clean," we chose to focus on oxygen, since it is produced by SNII, which, as we said above, are closely "tied" to the spiral arms.

The angular velocity of the spiral pattern, Ω_P, is one of the most important parameters of the Galactic density wave responsible for the spiral arms. This pattern speed determines the location of the so-called corotation resonance—the region where the pattern speed equals the angular rotational velocity of the Galactic disk.[1]

The corotation resonance and its position within the galaxy is one of the fundamental properties of a spiral galaxy [13]. One of our aims here is to analyze the effect of the corotation resonance on the radial distribution of oxygen in the disk. This problem has acquired particular interest because, as was first shown by Marochnik *et al.* [14], the corotation resonance is located near the solar circle. Creze and Mennesier [15] came to the same conclusion, based on quite different data. This idea is now gaining popularity (see, e.g., [16–24] and other papers). At the same time, a number of studies have explored the possibility that the corotation resonance is located in the inner part of the Galaxy, at $r = 3$–4 kpc [25–27]. Analyses of the radial distribution of heavy elements may make it possible to choose between these models.

[1] It is significant that the spiral wave pattern rotates as a rigid body ($\Omega_P = \text{const}$), whereas the Galactic disk rotates differentially (Ω is a function of Galactocentric distance r). The distance r_C at which the two angular velocities coincide ($\Omega(r_C) = \Omega_P$) is referred to as the corotation radius.

2. OBSERVATIONAL DATA

We used data on the radial distribution of oxygen in the Galaxy derived from observations of Cepheids and type II planetary nebulae. These are bright objects observable at great distances, and so represent the distribution of elements throughout a fairly large region of the Galaxy. These objects are believed to undergo no significant changes in their oxygen abundance throughout their lifetimes.

To reveal the systematic trend in the oxygen distribution more clearly, we subdivided the radial distances into 0.5 kpc bins and averaged the abundances within these bins. We adopted the Cepheid oxygen abundances from Andrievsky *et al.* [4, 5] and the planetary-nebula abundances from Maciel and Quireza [6]. Figure 1 shows the averaged abundances relative to the solar value; to illustrate the effect of the bin size, we show results for two choices of averaging bins. It is obvious that the overall pattern of the averaged radial distribution of the oxygen abundance in the Galaxy is independent of the choice of averaging bins. Both types of object show a well-defined bimodal pattern, as described above, with a steep gradient in the inner part and a fairly flat dependence at $r = 7$–11 kpc and $r = 7$–9 kpc for Cepheids and planetary nebulae, respectively. It is this structure that we analyze here.[2]

3. BASIC EQUATIONS AND MODELS

The chemical-evolution equations that we used are close to the traditional equations [29], and have the form

$$\frac{\partial \mu_S}{\partial t} = (1 - R)\psi, \tag{1}$$

$$\frac{\partial \mu_g}{\partial t} = -(1 - R)\psi + f, \tag{2}$$

$$\mu_g \frac{\partial Z}{\partial t} = P_Z \psi + f(Z_f - Z) + \frac{1}{r}\frac{\partial}{\partial r}(r\mu_g D \frac{\partial Z}{\partial r}), \tag{3}$$

where Z is the abundance of heavy elements (oxygen in our case), μ_S and μ_g are the surface densities of the stellar and gaseous disks, ψ is the star-formation rate (SFR), f is the rate of mass infall onto the Galactic disk, Z_f is the heavy-element abundance

[2] Note the possible selection effect that objects at greater Galactocentric distances are located systematically higher above the Galactic plane, which could result in underestimated abundances for these objects due to the negative vertical abundance gradient [28]. However, our estimates based on the gradient presented in [28] show this bias to be insignificant. Moreover, this effect should make the bimodal structure even more conspicuous.

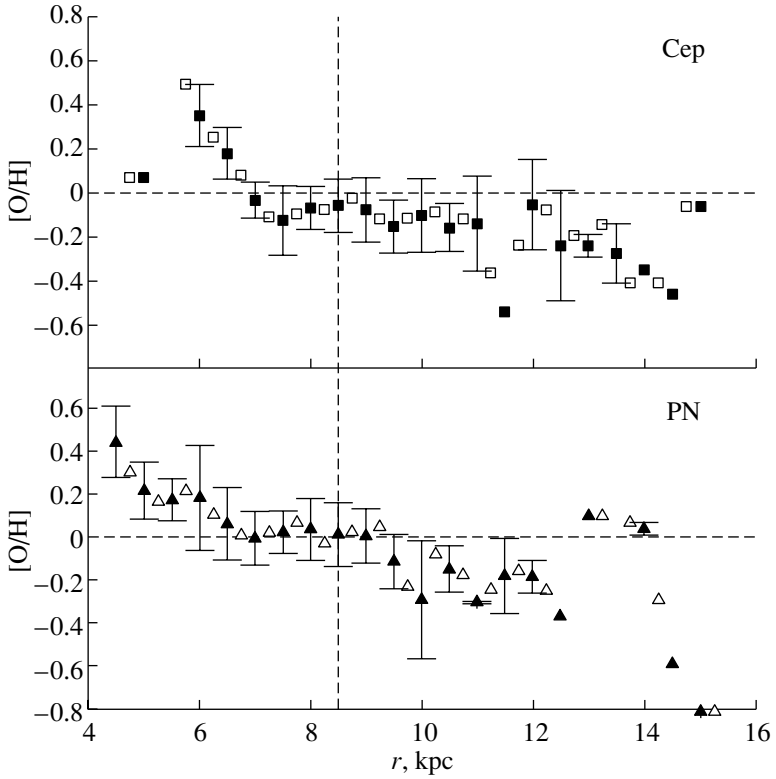

Fig. 1. Radial distributions of oxygen averaged over 0.50 kpc bins derived from data for Cepheids (top) and planetary nebulae (bottom). Open and filled symbols correspond to different positions of the averaging bins: the centers of filled-symbol bins are located at integer and half-integer r values, while the centers of open-symbol bins are shifted by 1/4 kpc relative to these values. The bars show the standard errors of the mean abundances within each bin. The lack of a bar means that the corresponding bin contains only one data point. Objects of both types show a clear bimodal structure—a steep gradient in the inner part of the Galaxy at $r < 7$ kpc and fairly flat distribution in the outer part (out to $r \approx 11$ and $\approx$9 kpc for Cepheids and planetary nebulae, respectively). The data points at the greatest Galactocentric distances should have the largest errors in both the distances and oxygen abundances (see references in the text).

of the matter falling onto the Galactic disk (following Tinsley [29], we adopted $Z_f = 0.17Z_\odot$), R is the mass fraction of the matter returned to Galactic gas from the stellar component, and P_Z is the fraction of the stellar mass that is ejected into the interstellar medium in the form of newly synthesized elements [29]. The last term in (3) describes the diffusion of elements with the diffusion coefficient D. We take this diffusion to be due to various kinds of turbulence in the interstellar medium. We represent the turbulent interstellar medium as a system of chaotically moving clouds, and can phenomenologically estimate the diffusion coefficient in a gas-kinetic approach:

$$D = \frac{HV_T}{3\pi\sqrt{2}\mu_g}\frac{m_c}{a^2}, \qquad (4)$$

where H is the thickness of the gaseous disk, V_T is the one-dimensional dispersion of the chaotic velocities of the clouds, and m_c and a are the mass and radius of the clouds. In our computations, we adopted $H = 130$ pc, $V_T = 6.6$ km/s, and $m_c/a^2 = 100M_\odot/\mathrm{pc}^2$ [30]. Thus, unlike the standard equations describing the chemical evolution of the Galaxy, our equations allow for the diffusion of elements. The effects of this diffusion are weak in the case of small gradients, but become appreciable in the case of large gradients. Note also that diffusion smooths the distribution of elements, but not the overall density.

Let us now analyze how the spiral arms affect the synthesis of heavy elements. The effect of the spiral arms can be manifest through three channels: (1) radial flows of interstellar gas due to the spiral arms, (2) the star-formation rate, and (3) the rate of injection of elements into a given volume of the interstellar medium. Let us discuss these three possibilities.

The additional divergent term in (3) describes the effect of radial flows, including those emanating from spiral arms. These effects were analyzed by Mishurov *et al.* [9], Lacey and Fall [31] and Portinari and Chiosi [32], and we do not consider them further here. Let us now turn to remaining two mechanisms.

Based on the idea of Roberts [11] and Shu *et al.* [33] that spiral arms trigger star formation,

Oort [8] suggested that the SFR $\psi(r,t)$ is proportional to the difference $\Omega - \Omega_P$—this is the second way in which the spiral arms can affect the radial distributions of elements in the Galaxy.[3] This representation was later used by a number of authors, e.g., Portinari and Chiosi [32] and Wyze and Silk [34].

At present, there is no consensus as to whether spiral arms trigger star formation. Contrary to the opinion expressed by Roberts [11], some authors, e.g., Elmegreen [35] and Casse *et al.* [36], have suggested that spiral arms do not trigger star formation. On the other hand, there is indeed evidence supporting the opposite view [37]. On the whole, the only thing that we can now state with certainty is that the most massive stars, including the precursors of the SNII that act as sources of oxygen, are concentrated in the spiral arms. At the same time, the above equations contain the SFR for stars of all masses, including low-mass stars.

To illustrate the effect of the spiral arms on the radial distribution of oxygen, we now follow the traditional approach and use simplified equations for the chemical evolution in the instantaneous recycling approximation. This is why ψ represents the rate at which matter is transformed from a gaseous form into stars of all masses, and not just into the massive stars that explode as SNII. If we assume, following Oort [8], that $\psi \propto |\Omega - \Omega_P|$, we then find for a monotonic dependence (as a function of Galactocentric distance r) of the rate of mass infall onto the Galactic disk, according to (1) and (2), that the stellar and gas densities have their minimum and maximum, respectively, in the vicinity of the corotation radius—a pattern that has not been observed (although this does not rule out the possibility that this effect might show up in more accurate future observations). This is why we suggest a different interpretation of the effect of spiral arms on the production of oxygen, although it will become evident below that, mathematically, our representation does not differ from that of Oort [8].

Unlike in the first two mechanisms, in the third means by which the spiral arms can influence the radial abundances of elements, the rate of oxygen enrichment, P_Z, cannot be taken to be a constant. This rate should clearly be proportional to the rate at which a given volume of matter crosses the spiral arms. Indeed, as we pointed out above, the SNII acting as sources of oxygen are strongly concentrated in the spiral arms. A specific volume of interstellar gas will be enriched in oxygen only when it passes near sources of this element; i.e., in the arms where SNII are concentrated. The more time this volume of gas spends inside the arms, the higher the rate of oxygen enrichment. The rate at which a given gas volume element enters spiral arms is determined by the difference $|\Omega - \Omega_P|$. We therefore have

$$P_Z = \eta|\Omega - \Omega_P|\Theta, \qquad (5)$$

where η and Θ are normalization and cutoff factors, respectively (see below).

Our final formula for the product $P_Z\psi$ appearing in (3) is the same as that of Oort. Note that the arguments Oort [8] used to argue for his description of the effect of the spiral arms on the rate of production of heavy elements are similar to those we employ here—the enrichment rate for a given gas volume will increase in proportion to the time it spends in the vicinity of sources of heavy elements, i.e., in spiral arms.

Strictly speaking, as was pointed out by the anonymous reviewer, we should analyze in a self-consistent way the simultaneous effect of the spiral arms on both the chemical evolution of the Galactic disk and the transformation of matter from the gaseous into the stellar phase. However, this is not possible in the instantaneous recycling approximation: the equations for the transformation of matter from the gaseous into the stellar phase and the chemical-evolution equation contain different SFRs, corresponding to stars of all masses and only massive stars, respectively, whereas a single SFR appears in the above equations. Moreover, the very popular model describing the infall of mass onto the Galactic disk using a monotonic radial function, which has yielded the current density distributions for the stellar and gaseous components, is a rather crude approximation. A more adequate model should allow for the azimuthal structure of the Galactic disk and the irregularity (clumpiness) of the mass falling onto the Galactic disk. We plan to address this problem in a future paper.

Let us now discuss the formula for the cutoff factor Θ. The wave zone for spiral-density waves is constrained between the outer and inner Lindblad resonances [38]. The object of this study is oxygen, whose sources (SNII) are closely associated with spiral arms (we do not consider here the central region of the Galaxy, which is dominated by the influence of the bulge and the bar). Therefore, $\Theta = 1$ between the Lindblad resonances and $\Theta = 0$ beyond them. The position of the wave zone, in turn, is determined by the condition $|\nu_m| < 1$, where $\nu_m = m(\Omega - \Omega_P)/\kappa$ is the

[3] When considering the dependence of the SFR on the parameters of the spiral wave, it is natural to expect that the SFR should be a function of the intensity of the spiral shock and not of the difference $\Omega - \Omega_P$, which characterizes the rate at which a given volume of interstellar gas crosses the spiral arm. At the same time, the intensity of the shock turns out to be approximately proportional to $\Omega - \Omega_P$. This is therefore consistent with Oort's approximation, although his arguments actually reduce to the rate at which a given gas volume crossed the spiral arms; i.e., to the third mechanism noted above.

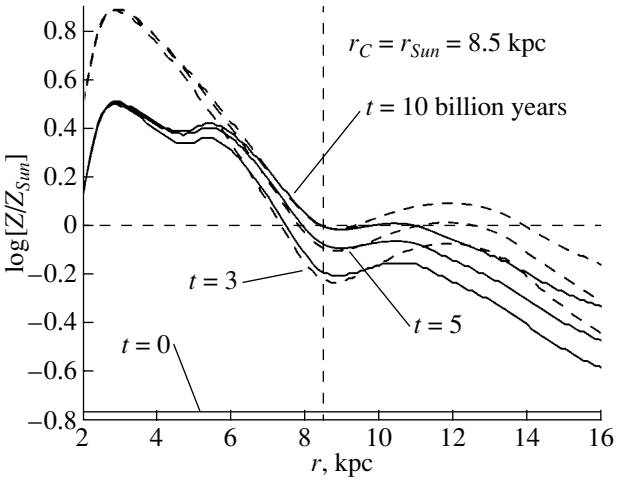

Fig. 2. Evolution of the radial distribution of oxygen in the *stationary* model. The dashed line shows a purely two-armed pattern and the solid line a pattern formed by the superposition of a two-armed and a four-armed harmonic. The corotation radius is located at the solar radius. The radial distribution evolves fairly rapidly during the first five Gyr, after which it slows appreciably.

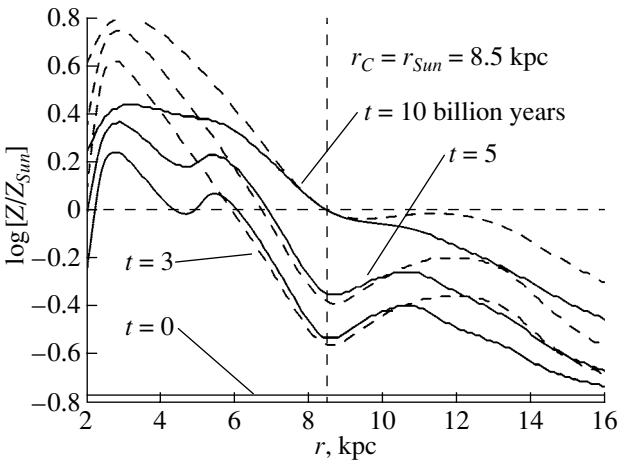

Fig. 3. Same as Fig. 2 for the *nonstationary* model. The enrichment in the initial stages of the evolution of the Galaxy is slower than in the previous case, and the gradient flattens during the last stage of the Galaxy's evolution.

dimensionless frequency of the wave, m is the number of spiral arms (two or four), and κ is the epicyclic frequency [38].

We must also consider another point. Various different models have been suggested for the wave pattern in our Galaxy. In models in which the pattern can be described by a single harmonic, Θ can be found as above. However, in some models, the spiral pattern has the form of a superposition of two- and four-armed harmonics [19, 20]. In this case, Θ can be written in the form $\Theta = \Theta_2 + 2\Theta_4$, where the subscripts refer to the corresponding harmonics and the cutoff Θ_m is determined by the dimensionless wave frequency ν_m. The factor of two in the second term is due to the fact that the four-armed pattern is crossed twice as often as the two-armed pattern.

Our computations used the rotation curve of Allen and Santillan [39].

Let us now turn to models for the SFR. The following Schmidt-type representation is very popular in the theory of the chemical evolution of galaxies:

$$\psi = \beta\mu_g^k. \tag{6}$$

Here, β is a normalization factor and the exponent k varies from 1 to 2. Our computations using various exponents yielded similar results; we show below the results obtained for $k = 1.5$ [40]. We also assume, in accordance with Lacey and Fall [31] and Portinari and Chiosi [32], that the rate of mass infall onto the Galactic disk is equal to $f(r,t) = A(r)\exp(-t/\tau)$, where $A(r)$ is determined by the final (i.e., corresponding to the present epoch $t = T_D$, where $T_D =$ 10 Gyr is the age of the Galactic disk) distribution of the combined density of stars and gas in the disk (see the papers cited above) and τ is the time scale for the deceleration of the mass-infall rate. We call this the *nonstationary* model.

At the same time, some authors have advocated the so-called Besançon model developed by a group of French researchers [41, 42]. In this model, the SFR is constant (or even grows slightly in time), so that the surface density of the gaseous disk and the rate of mass infall onto the Galactic disk are also constant. It is natural to call this the *stationary* model. In this model, it follows from (2) that

$$(1 - R)\psi = f. \tag{7}$$

Combined with (1), this formula implies

$$f = \frac{\mu_S(r, T_D)}{T_D}. \tag{8}$$

Finally, in the *stationary* model, the chemical-evolution equation (3) acquires the form

$$\mu_g\frac{\partial Z}{\partial t} = \frac{P_Z f}{1 - R} + f(Z_f - Z) + \frac{1}{r}\frac{\partial}{\partial r}(r\mu_g D\frac{\partial Z}{\partial r}). \tag{9}$$

As boundary conditions, we used the so-called natural boundary conditions for diffusive processes—zero fluxes at the outer boundary and at the center (our computations showed that the results depend only weakly on the particular choice of the radius of the Galaxy, and we set it equal to 25 kpc). The effect of the bulge, bar, and strong nonradial motions of the medium must be taken into account in the central regions of the Galaxy, and we do not attempt to apply our results to the chemical evolution of the Galactic

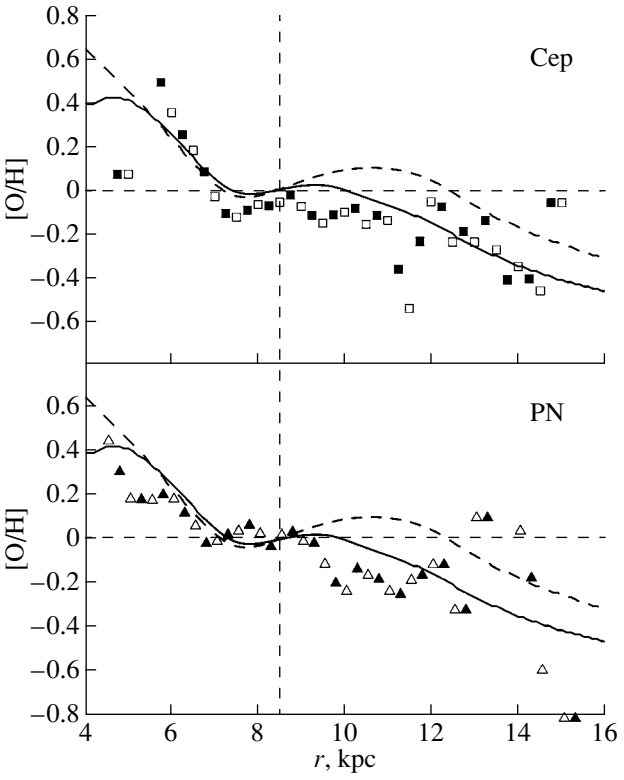

Fig. 4. Comparison of the theoretical oxygen distribution with observations in the *stationary* model. We set the corotation radius equal to 7.5 kpc. The tendency of the data for the largest distances from the Galactic center to fall away from the overall dependence may be due in part to the large errors in both the distances to these objects and their chemical compositions, as well as to the effect of another factor—the outer Lindblad resonance.

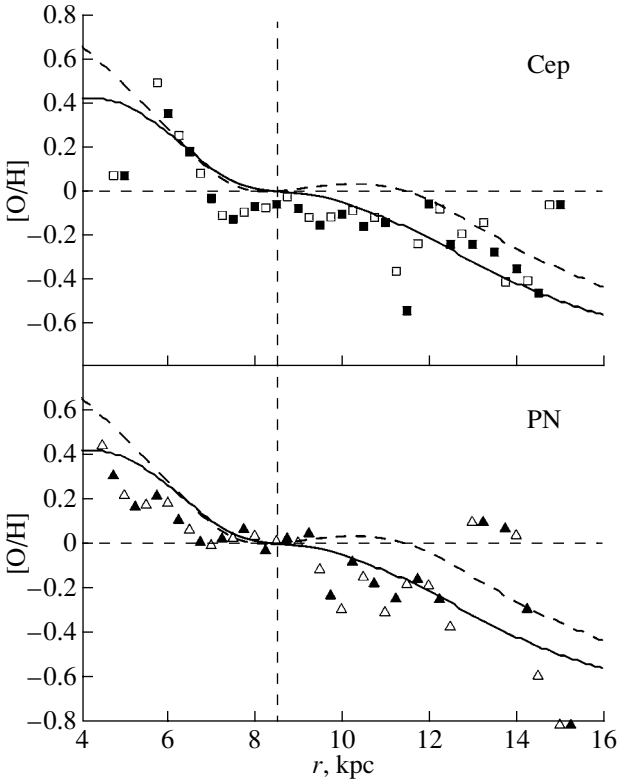

Fig. 5. Same as Fig. 4 for the *nonstationary* model.

center. The above boundary condition at the center serves only to guarantee that the abundance is finite.

We set the oxygen abundance at the initial time equal to its value in the infalling matter. The initial densities of the stellar and gaseous disks in the *nonstationary* model are equal to zero [31, 32].

The normalization factors are chosen to make the computed current densities of the gaseous and stellar components coincide with the modern values of $\mu_g(r_\odot, T_D) = 10 M_\odot/\mathrm{pc}^2$ and $\mu_S(r_\odot, T_D) = 40 M_\odot/\mathrm{pc}^2$ [42], and to ensure that the present abundance relative to the solar value is equal to zero.

4. RESULTS OF THE COMPUTATIONS

Figure 3 shows the evolution of the radial distribution of the oxygen abundance in the stationary and nonstationary models for a purely two-armed pattern and a pattern in the form of a superposition of two-armed and four-armed harmonics with the corotation resonance located at the solar radius. It is clear that the model develops a nearly bimodal structure. The physical origin of this pattern is easy to understand: the oxygen enrichment function vanishes at the corotation radius, and were it not for the spreading of material due to diffusion, the abundance there would be equal to that of the matter falling onto the Galaxy. In this case, the model should develop a two-peaked distribution, with one peak located inside and one outside the corotation radius. The diffusion in the vicinity of the corotation radius leads to a more or less flat distribution near this radius, approximately forming a plateau. In both models, the warp of the radial distribution of oxygen in the vicinity of the corotation radius is smaller for the superposition of two-armed and four-armed harmonics than for the purely two-armed pattern. This is also easy to understand: when present, the four-armed pattern embedded in the two-armed pattern makes an additional contribution to the enrichment in its narrower zone, since the gas volume crosses the four-armed pattern twice as often as it does the two-armed pattern.

Note also that the dynamics of the enrichment differ in the different models. For example, in the initial stage, the evolution is much more rapid in the stationary than in the nonstationary model, but the elemental abundances in the stationary model varied little over the last three-to-five billion years (Klochkova and Panchuk [43] were the first to point out this fact based on observational data). At the same time, the

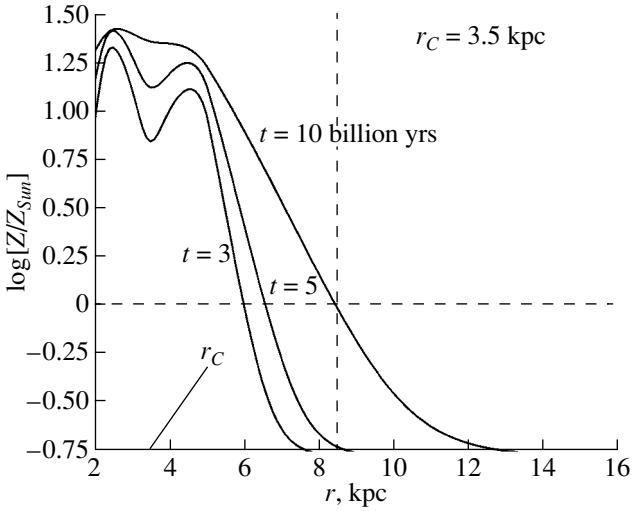

Fig. 6. Evolution of the radial distribution of oxygen in a model in which the corotation resonance is located in the inner part of the Galaxy, at $r_C = 3.5$ kpc (model [25–27]). No bimodal structure develops in this case.

overall gradient in the nonstationary model becomes flatter with time. Maciel *et al.* [44] came to this same conclusion based on their data on planetary nebulae.

Note also that the oxygen abundance beyond the solar circle may be substantially higher than in the vicinity of the solar circle.

Figures 4 and 5 compare our theoretical computations with the observed distribution of oxygen based on the data for Cepheids and planetary nebulae. It is clear that the computations agree well with observations in both models, especially if the corotation radius is located at a Galactocentric distance of about 7.5 kpc.

Quite a different picture emerges if we suppose that the corotation radius is located in the inner region, say at $r_C = 3.5$ kpc, and that there are four arms (the model of [25–27]). Figure 6 shows that this choice of parameters does not produce a bimodal structure. Thus, the observed radial distribution of oxygen does not support the idea that the corotation resonance is located in the inner region of the Galaxy. The studies of Bissantz *et al.* [45] are relevant in this connection. In their initial analysis for the inner part of the Galaxy alone [25], they obtained a rapidly rotating four-armed pattern with the corotation radius located at $r_C = 3.5$ kpc; their more recent analysis [45] suggested a composite spiral structure, with a rapidly rotating inner pattern and an outer (at $r > 4$ kpc) spiral pattern rotating with an angular velocity that is lower by a factor of two to three. This structure would obviously produce a bimodal distribution of oxygen with a warp in the solar neighborhood.

5. CONCLUSIONS

Based on our analysis of the radial oxygen distribution in the Galaxy, we suggest a theory for the formation of the characteristic radial distributions of elements produced by type II supernovae in spiral galaxies, which are strongly concentrated in the spiral arms. The combined effect of the spiral arms—the corotation resonance and diffusion—results in the development of a bimodal distribution of oxygen with Galactocentric radius, with a fairly steep negative gradient in the inner region and a relatively flat distribution in the solar neighborhood. Models in which the corotation radius is located near the Sun gave the best agreement, while models in which the corotation radius lies in the inner part of the Galaxy do not develop a bimodal distribution of the oxygen abundance.

ACKNOWLEDGMENTS

We thank B.M. Shustov and A.V. Tutukov for useful and fruitful discussions and the anonymous referee for constructive suggestions. This work was partially supported by the "Fundamental Research in the Natural Sciences" foundation of the Ministry of Education of the Russian Federation (grant no. E02-11.0-1) and the Federal program "Integration" (grant no. B0087/2122).

REFERENCES

1. F. Matteucci, in *Origin and Evolution of the Elements*, Ed. by A. McWilliam and M. Rauch (Cambridge Univ. Press, 2003), Carnegie Astrophys. Ser., p. 1.
2. D. Z. Wiebe, A. V. Tutukov, and B. M. Shustov, Astron. Zh. **78**, 977 (2001) [Astron. Rep. **45**, 854 (2001)].
3. B. A. Twarog, K. M. Ashman, and B. J. Anthony-Twarog, Astron. J. **114**, 2556 (1997).
4. S. M. Andrievsky, D. Bersier, V. V. Kovtyukh, *et al.*, Astron. Astrophys. **384**, 140 (2002).
5. S. M. Andrievsky, R. E. Luck, P. Martin, and J. R. D. Lepine, Astron. Astrophys. **413**, 159 (2004).
6. W. J. Maciel and C. Quireza, Astron. Astrophys. **345**, 629 (1999).
7. A. V. Tutukov, personal communication, 2004.
8. J. H. Oort, in *IAU Symp. No. 58: The Formation and Dynamics of Galaxies*, Ed. by J. R. Shakeshaft (Reidel, Dordrecht, 1974), p. 375.
9. Yu. N. Mishurov, J. R. D. Lepine, and I. A. Acharova, Astrophys. J. Lett. **571**, L113 (2002).
10. O. S. Bartunov, D. Yu. Tsvetkov, and I. V. Filimonova, Publ. Astron. Soc. Pac. **106**, 1276 (1994).
11. W. W. Roberts, Astrophys. J. **158**, 123 (1969).
12. C. Kobayashi, T. Tsujimoto, K. Nomoto, I. Hachisu, and M. Kato, Astrophys. J. Lett. **503**, L155 (1998).
13. B. Canzian, Astrophys. J. **502**, 582 (1998).

14. L. S. Marochnik, Yu. N. Mishurov, and A. A. Suchkov, Astrophys. Space Sci. **19**, 285 (1972).
15. M. Creze and P. O. Mennissier, Astron. Astrophys. **27**, 281 (1973).
16. Yu. N. Mishurov, I. A. Zenina, A. K. Dambis, *et al.*, Astron. Astrophys. **323**, 775 (1997).
17. Yu. N. Mishurov and I. A. Zenina, Astron. Zh. **76**, 563 (1999) [Astron. Rep. **43**, 487 (1999)].
18. Yu. N. Mishurov and I. A. Zenina, Astron. Astrophys. **341**, 81 (1999).
19. L. H. Amaral and J. R. D. Lepine, Mon. Not. R. Astron. Soc. **286**, 885 (1997).
20. J. R. D. Lepine, Yu. N. Mishurov, and S. Yu. Dedikov, Astrophys. J. **546**, 234 (2001).
21. S. von Linden, K. Otmianowska-Mazur, K. Lesch, and G. Skupniewich, Astron. Astrophys. **333**, 79 (1998).
22. E. M. Leicht and G. Vasisht, New Astron. **3**, 51 (1997).
23. D. Fernandez, F. Figueras, and J. Torra, Astron. Astrophys. **372**, 833 (2001).
24. A. M. Fridman, O. V. Khoruzhii, V. V. Lyakhovich, and V. S. Avedisova, in *XXII General Assembly of IAU,* Ed. by H. van Woerden (Netherlands, 1994), p. 167.
25. P. Englmaier and O. Gerhard, Mon. Not. R. Astron. Soc. **304**, 512 (1999).
26. W. Dehnen, Astrophys. J. Lett. **524**, L35 (1999).
27. M. D. Weinberg, Astrophys. J. **420**, 597 (1994).
28. D. S. Wiebe, A. V. Tutukov, and B. M. Shustov, Astron. Zh. **75**, 3 (1998) [Astron. Rep. **42**, 1 (1998)].
29. B. M. Tinsley, Fundam. Cosm. Phys. **5**, 287 (1980).
30. B. Elmegreen, in *Interstellar Processes*, Ed. by D. J. Hollenbach and H. A. Thronson (Reidel, Dordrecht, 1987), p. 259.
31. C. G. Lacey and S. M. Fall, Astrophys. J. **290**, 154 (1985).
32. L. Portinari and C. Chiosi, Astron. Astrophys. **350**, 827 (1999).
33. F. H. Shu, V. Millione, W. Gebel, *et al.*, Astrophys. J. **173**, 557 (1972).
34. R. F. G. Wyze and J. Silk, Astrophys. J. **339**, 700 (1989).
35. B. G. Elmegreen, in *Star-forming Regions* (Reidel, Dordrecht, 1987), p. 457.
36. M. Casse, D. Kunth, and J. M. Scalo, Astron. Astrophys. **78**, 336 (1979).
37. R. Sagar, U. Munari, and K. S. de Boer, Mon. Not. R. Astron. Soc. **327**, 23 (2001).
38. C. C. Lin, C. Yuan, and F. H. Shu, Astrophys. J. **155**, 721 (1969).
39. C. Allen and A. Santillan, Rev. Mex. Astron. Astrofis. **22**, 255 (1991).
40. R. C. Kennicutt, Astrophys. J. **498**, 541 (1998).
41. A. C. Robin and M. Creze, Astron. Astrophys. **157**, 71 (1986).
42. M. Haywood, A. C. Robin, and M. Creze, Astron. Astrophys. **320**, 440 (1997).
43. V. G. Klochkova and V. E. Panchuk, Sov. Astron. Lett. **17**, 229 (1991).
44. W. J. Maciel, R. D. D. Costa, and M. M. M. Uchida, Astron. Astrophys. **397**, 667 (2003).
45. N. Bissantz, P. Englmaier, and O. Gerhard, Mon. Not. R. Astron. Soc. **340**, 949 (2003).

Translated by A. Dambis

Astronomy Reports, Vol. 49, No. 5, 2005, pp. 362–367. Translated from Astronomicheskiĭ Zhurnal, Vol. 82, No. 5, 2005, pp. 407–413.

Supermassive Black Holes: Relation to Dark Halos

A. V. Zasov, L. N. Petrochenko, and A. M. Cherepashchuk

Sternberg Astronomical Institute, Universitetskiĭ pr. 13, Moscow, 119992 Russia

Received September 29, 2004; in final form, December 3, 2004

Abstract—Estimates of the masses of supermassive black holes (M_{bh}) in the nuclei of disk galaxies with known rotation curves are compared with estimates of the rotational velocities V_m and the "indicative" masses of the galaxies M_i. Although there is a correlation between M_{bh} and V_m or M_i, it is appreciably weaker than the correlation with the central velocity dispersion. The values of M_{bh} for early-type galaxies (S0–Sab), which have more massive bulges, are, on average, higher than the values for late-type galaxies with the same rotational velocities. We conclude that the black-hole masses are determined primarily by the properties of the bulge and not the rotational velocity or the mass of the galaxy. © *2005 Pleiades Publishing, Inc.*

The detection of supermassive black holes (SMBHs) in the nuclei of galaxies has given rise to vigorous discussions about the origin and evolution of these unique objects and their role in the evolution of the galaxies themselves. To address these questions, it is important to know how the mass of the black hole is related to the parameters of the various components of the galaxy. First and foremost, it was established that the mass of the SMBH was correlated (although with a large dispersion) with the luminosity of the spheroidal components of the galaxy. This conclusion, first made in the 1990s [1], was subsequently confirmed: the most massive SMBHs are found in the nuclei of high-luminosity lenticular and elliptical galaxies. However, it is not yet clear whether the mass of the SMBH governs the processes occurring in the vicinity of the nucleus or whether this relation is associated with some mechanism for the joint formation of the galaxy as a whole and SMBH. Both possibilities have been discussed in the literature.

In the former case, the growth in the mass of the SMBH to its observed value is due to the accretion of matter in the gravitational field of the galactic bulge (see the discussion of this question in [2, 3]). One possible mechanism that could bring material into the neighborhood of the SMBH is radiative deceleration of the interstellar medium in the radiation field of the bulge [4, 5]. This can explain the existence of a tight correlation between the mass of the SMBH and the mass (luminosity) of the bulge, or alternatively with the central stellar-velocity dispersion S_0, which reflects (in some approximation) the depth of the potential well in which the stars move in these slowly rotating systems.

The second view above is based on cosmological scenarios for the formation of galaxies as a result of the gravitational compression of an initially expanding medium that contains both baryonic matter and nonbaryonic dark matter. In this picture, the mass of the SMBH, M_{bh}, is produced not by the mass of the bulge, but by the total mass of the compressed nonbaryonic medium (the dark halo), in whose field the stellar galaxy formed. In turn, the mass of the halo is probably related to the maximum (asymptotic) rotational velocity at large distances R from the center (see the discussion of this question in [6]). An intermediate version is also possible: both the baryonic and nonbaryonic components of the galaxy play important roles in the formation of the black hole; the mass of the black hole slowly grows over the entire lifetime of the galaxy due to the accretion of stars and the non-adiabatic accretion of dark matter, reaching the observed masses over billions of years [7, 8].

Although the relation between M_{bh} and the velocity dispersion S_0 does not flow directly from this second hypothesis, the observed dependence must reflect a correlation between S_0 and the maximum rotational velocity of the galaxy V_m. This idea, which was first suggested by Ferrarese [6], found further support in [9, 10].

It stands to reason that a direct comparison of M_{bh} and the velocity V_m would be a more trustworthy means to establish a genuine correlation between these parameters. Unfortunately, only a small number of galaxies with measured masses for their SMBHs have reliably determined rotation curves, and knowledge of the galactic rotation curve is necessary to verify the hypothesis that there is a relationship between M_{bh} and either the rotational velocity or the total mass of the galaxy within some specified radius. Therefore, as a rule, conclusions about a relationship between M_{bh} and the rotational velocity have been

1063-7729/05/4905-0362$26.00

Galaxies with known rotation curves and measured SMBH masses

Galaxy	Type	$\log S_0$ (km/s)	$\log V_c$ (km/s)	i, deg	Reference	$\log M_{bh}(M_\odot)$	Reference
Milky Way		–	2.36	90	[11]	6.47	[12]
NGC 224	Sb	2.27	2.45	77	[11]	7.52	[12]
NGC 598	Sc	1.56	2.03	54	[11]	<3.18	[12]
NGC 1023	S0	2.31	2.40	70	[13]	7.59	[12]
NGC 1052	S0	2.43	2.28	44	[13]	8.29	[14]
NGC 1365	SBb	2.18	2.44	46	[11]	7.66	[14]
NGC 2273	Sba	2.09	2.34	53	[15]	7.27	[14]
NGC 2787	S0–a	2.29	2.37	55	[13]	7.59	[12]
NGC 2841	Sb	2.31	2.52	68	[11]	8.42	[14]
NGC 3031	Sab	2.21	2.38	59	[11]	7.80	[12]
NGC 3079	SBcd	2.16	2.38	90	[11]	7.65	[14]
NGC 3115	E–S0	2.41	2.57	67	[13]	8.95	[12]
NGC 3169	Sa	2.22	2.30	63	[16]	7.91	[14]
NGC 3227	SBa	2.12	2.43	56	[17]	7.59	[12]
NGC 3384	E–S0	2.17	2.39	59	[13]	7.26	[12]
NGC 3627	SBb	2.06	2.30	60	[18]	7.26	[14]
NGC 3675	Sb	2.03	2.35	60	[19]	7.11	[14]
NGC 3783	SBab	2.19	2.26	25	[20]	6.97	[12]
NGC 4051	SBbc	1.92	2.20	49	[21]	6.11	[12]
NGC 4151	SBbc	2.19	2.18	21	[22]	7.18	[12]
NGC 4203	E–S0	2.21	2.36	29	[23]	<7.08	[12]
NGC 4258	SBbc	2.13	2.32	67	[11]	7.61	[12]
NGC 4321	SBbc	1.93	2.43	27	[11]	6.80	[14]
NGC 4388	Sb	2.06	2.37	90	[24]	6.80	[14]
NGC 4395	SBm	–	1.95	71	[25]	<5.04	[12]
NGC 4450	Sab	2.11	2.30	44	[26]	7.30	[14]
NGC 4459	S0	2.24	2.48	42	[27]	7.81	[12]
NGC 4501	Sb	2.21	2.48	56	[26]	7.90	[14]
NGC 4548	SBb	2.16	2.48	38	[28]	7.40	[14]
NGC 4565	Sb	2.13	2.41	86	[11]	7.70	[14]
NGC 4579	SBb	2.19	2.50	36	[26]	7.85	[14]
NGC 4594	Sa	2.40	2.56	84	[29]	9.04	[12]
NGC 4725	Sbab	2.12	2.37	51	[25]	7.49	[14]
NGC 4736	Sab	2.02	2.26	35	[11]	7.30	[14]
NGC 4945	SBc	2.11	2.28	78	[11]	6.04	[12]
NGC 5033	Sc	2.12	2.44	55	[11]	7.30	[14]
NGC 5194	Sbc	1.98	2.41	20	[11]	6.90	[14]
NGC 6500	Sab	2.3	2.48	38	[30]	8.28	[14]
NGC 7469	Sba	–	2.08	48	[31]	6.81	[12]
Circinus	Sb	–	2.18	65	[32]	6.11	[12]
IC 342	SBc	1.89	2.30	25	[11]	<5.70	[12]

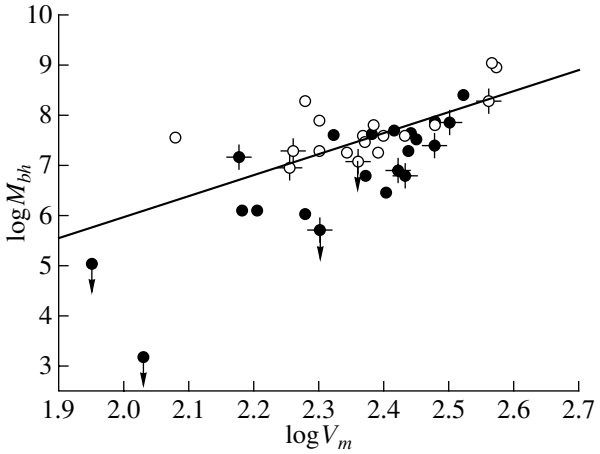

Fig. 1. Black-hole mass plotted against the maximum rotational velocity. The open symbols correspond to early-type S0–Sab galaxies. The crosses mark galaxies with disk inclinations $i < 40°$, for which the estimates of V_m are least reliable. The line shows the dependence found in [10] based on indirect measurements of V_m.

based on indirect evidence—the existence of a statistical dependence between the velocity dispersion S_0 and the circular rotational velocities of galaxies of various morphological types [9, 10]. The steeply growing number of disk galaxies (both spiral and lenticular) with measured SMBH masses provides the possibility of searching for a direct relation between the masses of the central black holes and the maximum rotational velocities derived from the galactic rotation curves $V(R)$. We present here the results of such a search.

The table contains information about the disk galaxies we used in our analysis. All of these galaxies have both estimates for the masses of their SMBHs (from [12, 14], which present a compiled list of estimates of M_{bh} obtained by various authors) and fairly reliable rotation curves—at least out to distances from the center where the curves become comparatively flat (reach a plateau) or begin to fall. The columns of the table contain (1) the name of the galaxy, (2) its morphological type, (3) the logarithm of the central velocity dispersion (in km/s), (4) the logarithm of the maximum rotational velocity in the disk (in km/s), (5) the adopted inclination (a face-on disk has $i = 0°$), (6) a reference for the rotation curve, and (7, 8) the logarithm of the black-hole mass in solar masses with the corresponding reference.

For some of the galaxies, the masses of the SMBHs have been estimated using the trustworthy technique of reverberation mapping. A comparison of the various methods used indicates that, as a rule, they lead to convergent estimates (within a factor of two to three) [12].

Searches of the literature for measurements of the velocity dispersions and rotational velocities were carried out using the "Central velocity dispersion" and "Kinematic resolved catalogue of galaxies" HYPERLEDA catalogs [33]. If rotation curves of a particular galaxy were presented in several independent papers, we gave preference to the one in which the shape of the curve was traced most clearly. If measurements were available for both absorption and emission lines, we always used the latter. For several of the early-type galaxies that have only rotation curves measured from absorption lines, we applied a correction for the stellar velocity dispersion (asymptotic drift) [13]. The presence in some cases of a maximum in the rotation curve near the nucleus, beyond which the rotation curve grows again, was disregarded in our estimates of V_m, since we took this first maximum not to be associated with the galactic halo. Galaxies with strong, large-scale, noncircular gas motions that hindered estimation of V_m were not included in our sample.

Figure 1 shows a comparison of the maximum rotational velocities V_m and the masses M_{bh}. The open symbols correspond to S0–Sab galaxies, which, as a rule, tend to have massive bulges. This diagram displays an absence of a tight correlation between these two parameters (the correlation coefficient is $k = 0.74$), although a crude correlation is obvious: slowly rotating disk galaxies (which are always low-luminosity galaxies) generally have black holes with relatively low masses. The two closely interacting galaxies that are included in the sample (NGC 3227 and NGC 5194) do not stand out among the other galaxies in the figure. The point indicating the lowest upper limit for the SMBH mass is M33.

Figure 1 shows that galaxies of early and late morphological types occupy different positions in the diagram: on average, S0–Sab galaxies possess more massive black holes than later-type galaxies with the same rotational velocities.

The straight line in Fig. 1 shows the relation obtained in [10] based on indirect estimates of V_m derived from measurements of S_0. There is only a crude agreement between this relation and the positions of the galaxies in the diagram: most of the points lie below this line.

Figure 2 presents a plot of M_{bh} versus the central velocity dispersion S_0 for the sample galaxies. This correlation is tighter than that between M_{bh} and V_m: $k = 0.90$ both for all galaxies and for the spiral galaxies of the sample. It is striking that the early-type galaxies (open symbols) lie on the same relation as the other galaxies, while they displayed systematically more massive SMBHs in Fig. 1.

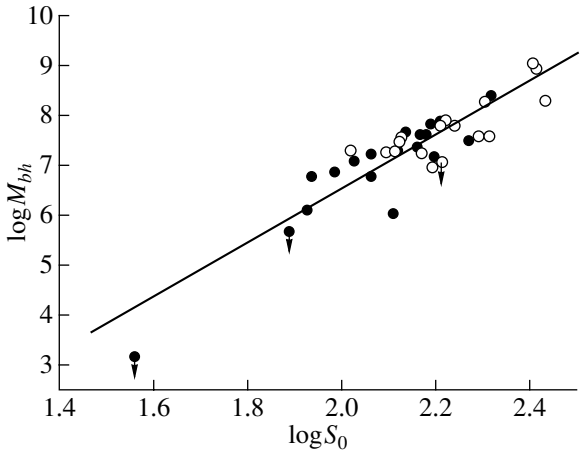

Fig. 2. Black-hole mass plotted against the central velocity dispersion. The open symbols correspond to early-type S0–Sab galaxies.

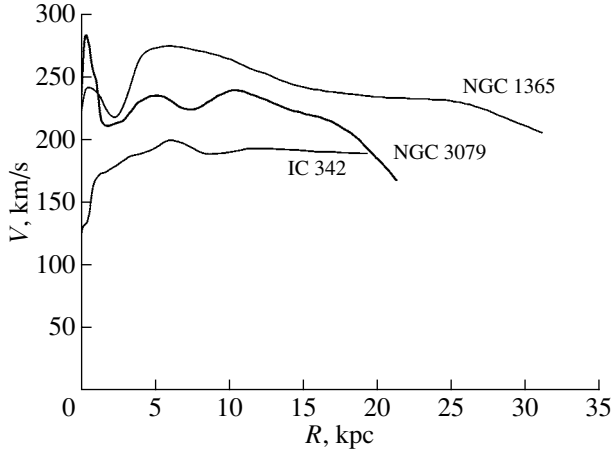

Fig. 3. Examples of galaxies with rotation curves of various forms $V(R)$ (from Sofue *et al.* [13]). The rotation curve of IC 342 enters a relatively flat plateau, the rotational velocity of NGC 3079 falls off at the edge of the galaxy, and the curve for NGC 1365 decreases monotonically in a large fraction of the disk.

In order to compare the masses of the SMBHs with V_m and S_0, it is necessary to take into consideration the fact that the rotational velocities can be determined with lower accuracy than the velocity dispersions. The main source of uncertainty in V_m is uncertainty in the angles describing the orientation of the disk (the inclination i and position angle of the kinematic major axis PA_0). Errors in the disk-orientation angles can introduce especially strong distortions in the V_m estimates for galaxies with small inclinations i (see the discussion of random and systematic errors in measurements of the orientation angles of spiral galaxies in [34]). For example, if $i = 30°$, a realistic uncertainty of $\Delta i = \pm 10°$ changes the resulting value of $\log V_m$ by -0.11 or $+0.16$, depending on the sign of the error. However, the scatter of the V_m values for a given value of M_{bh} in Fig. 1 appreciably exceeds the expected errors. Galaxies with $i < 40°$, which have the least certain V_m estimates, are marked by crosses in Fig. 1. It is obvious there is no basis to consider the inclusion of these galaxies as the main cause of the large scatter of the data points.

In some cases, estimation of V_m is hindered or less accurate for another reason—due to the complex form of the corresponding rotation curves, which by no means always exit onto a well defined plateau. Examples of galaxies with various rotation-curve shapes are presented in Fig. 3. The growth or decrease in the rotational velocity $V(R)$ at the edge of the disk often cannot be explained by uncertainty in the measurements. Indeed, analysis of the observational data shows that the sign and magnitude of the velocity gradient in the outer regions of the galaxies is systematically related to their total luminosities (masses) [25], providing evidence that these variations in the rotational velocity are real.

To decrease the uncertainty in the V_m estimates, we composed a list of the galaxies whose rotation curves were derived from the most trustworthy measurements. This list contained galaxies that appear in the representative samples of galaxies with extended rotation curves of Sofue *et al.* [11] and Casertano and van Gorkom [25]. Their rotation curves extend for no less than $0.9R_{25}$, where R_{25} is the radius of the galaxy at the 25 mag/arcsec^2 isophote. To enable a comparison with the early-type galaxies, we added to the subsample five nearby noninteracting S0 galaxies whose rotational velocities were determined reliably using a single method in [13] and the Sa galaxy with a very prominent bulge NGC 4594 (the "Sombrero" galaxy), whose extended rotation curve was determined in [29]. The rotation curves of these early-type galaxies are less extended than those for the remaining galaxies in the subsample, but can, nevertheless, be traced to distances of $R = (0.3–0.7)R_{25}$, where the initially fast growth of the curves is replaced by a nearly flat section, making it possible to estimate the maximum rotational velocity.

When the shape of the rotation curve displays a decrease in the rotational velocity at the edge of the galaxy, we considered separately the maximum rotational velocity V_m in the measured rotation curve and the rotational velocity at the maximum distance from the center $V(R_{\max})$. Since the relative contribution of the dark halo to the mass of the galaxy increases with R, we would expect the velocity $V(R_{\max})$ to be more closely related to the properties of the halo than V_m. This is indirectly supported by the fact that the Tully–Fisher relation between the luminosities of spiral galaxies and their rotational velocities becomes

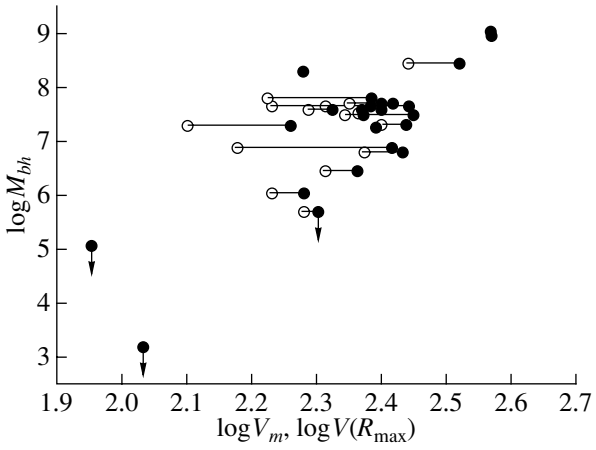

Fig. 4. Black-hole mass plotted against rotational velocity for the subsample of galaxies with the most reliably determined rotation curves. For galaxies for which the maximum rotational velocity V_m and the velocity at the edge of the rotation curve $V(R_{\max})$ are different, both values are presented, joined by a horizontal line segment.

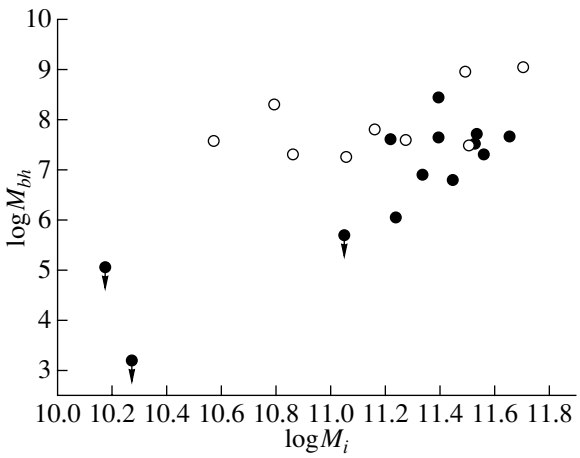

Fig. 5. Black-hole mass plotted against the indicative mass of the galaxy. The open symbols correspond to early-type S0–Sab galaxies.

tighter if velocities far from the central regions are used [35].

Figure 4 compares the SMBH masses of the subsample galaxies with both V_m and $V(R_{\max})$ (open symbols). We can see that the relation between M_{bh} and the rotational velocity is very loose for these galaxies. Using $V(R_{\max})$ in place of V_m increases rather than decreases the dispersion of the points in the diagram ($k = 0.82$ and 0.75, respectively), providing indirect evidence for a weak dependence between M_{bh} and the mass of the halo. We verified that there is likewise no dependence of the dispersion of the points in this plot on the inclination of the galactic disks.

We arrive at the same conclusion if we compare M_{bh} with the "indicative" mass of the galaxy $M_i = V_m^2 R_{25}/G$, which is close to the total mass of the galaxy within the limits of the optical image. As a rule, the mass of the dark halo within this distance is comparable to, or even greater than, the mass of the stellar component (see, for example, [36–38] and references therein). The M_i–M_{bh} diagram for the galaxies in our subsample is shown in Fig. 5. The large scatter of the points confirms the weak dependence between the black-hole masses and the total masses of the galaxies.

Let us summarize the results of this study.

The correlations between the SMBH mass and quantities characterizing the dark halo (V_m, $V(R_{\max})$, or M_i) and which are determined directly from the galactic rotation curves are appreciably weaker than the correlation with the central velocity dispersion. Since this latter quantity characterizes the depth of the potential well created by the galactic bulge, this suggests that the growth in the SMBH masses to the observed values is brought about primarily by processes associated with the stellar bulge of the galaxy. A close relationship between the black hole and the bulge is also indicated by the fact that early-type disk galaxies, which have relatively high bulge luminosities, possess systematically more massive black holes than do later-type spirals whose rotational velocities lie in the same interval (150–250 km/s). The S0–Sab galaxies lie on the same relationship as later-type spirals in a plot of SMBH mass versus central velocity dispersion (Fig. 2).

It is striking that, as we can see in Fig. 1, the dependence between the rotational velocity and black-hole mass nearly disappears for slowly rotating galaxies (although the relation between M_{bh} and the central velocity dispersion is preserved for these galaxies). It is important to take this fact into account when considering processes for the formation of the supermassive black holes.

Our conclusion that there is a connection between the SMBH and the bulge supports a scenario in which a central high-mass black hole does not form together with the galaxy, but instead grows as a result of accretion over the lifetime of the galaxy, whose intensity is determined by the conditions in the vicinity of the nucleus. Various mechanisms for the growth of the SMBH include the accretion of gas, stars, dark matter (see, for example, [6–8]), and even black holes formed in globular clusters [39]. However, it cannot be ruled out that the birth of the black hole in the galactic nucleus and its initial mass depend on the conditions under which the galaxy formed in the potential well (cusp) created by the mass of the dark halo, so that the presence of the dark halo could indirectly influence the current value of M_{bh} [7, 8].

The question of the rate at which the mass of the SMBHs varies can be answered only using direct estimates of the corresponding accretion rates. Gas accretion rates have recently been estimated for a large number of galaxies (adopting certain assumptions) based on the intensity of the [OIII] line emission of the galactic nuclei [40]. These results indicate that the characteristic times for the growth of the SMBH mass are probably very different for low-mass and massive black holes in galactic nuclei, being shorter for the former, and are probably comparable to the characteristic times for the growth of the surrounding stellar bulges. This is consistent with the conclusion that the current values of the SMBH masses are the result of process occurring (or that occurred in the past) in the bulges of these galaxies.

ACKNOWLEDGMENTS

We thank A.D. Chernin for stimulating discussions and A.V. Tutukov for valuable comments. This work was supported by the Federal Science and Technology Program "Astronomy" (contract no. 40.022.1.1.1101) and the Russian Foundation for Basic Research (project no. 04-02-16518).

REFERENCES

1. J. Kormendy and D. Richstone, Annu. Rev. Astron. Astrophys. **33**, 581 (1995).
2. D. Grupe and S. Mathur, Astrophys. J. Lett. **606**, L41 (2004).
3. J. Yoo and J. Miralda-Escude, Astrophys. J. (2005) (in press); astro-ph/0406217.
4. N. Kawakatu and M. Umemura, Astrophys. J. Lett. **601**, L21 (2004).
5. M. Umemura, Astrophys. J. Lett. **560**, L29 (2001).
6. L. Ferrarese, Astrophys. J. **578**, 90 (2002).
7. A. S. Il'in, K. P. Zybin, and A. V. Gurevich, Zh. Éksp. Teor. Fiz. **125**, 5 (2004) [JETP **98**, 1 (2004)].
8. V. A. Sirota, A. S. Ilyin, K. P. Zybin, and A. V. Gurevich, astro-ph/0403023.
9. A. Pizella, E. M. Corsini, J. C. Vega Beltran, *et al.*, Mem. Soc. Astron. Ital. **74**, 504 (2003).
10. M. Baes, P. Buyle, G. K. T. Hau, and H. Dejonghe, Mon. Not. R. Astron. Soc. **341**, L44 (2003).
11. Y. Sofue, Y. Tutui, M. Honma, *et al.*, Astrophys. J. **523**, 136 (1999).
12. A. M. Cherepashchuk, Usp. Fiz. Nauk **173**, 345 (2003) [Phys. Usp. **46**, 335 (2003)].
13. E. Neistein, D. Maoz, H.-W. Rix, and J. N. Tonry, Astron. J. **117**, 2666 (1999).
14. A. Merloni, S. Heinz, T. di Matteo, *et al.*, Mon. Not. R. Astron. Soc. **345**, 257 (2003).
15. W. van Driel and R. J. Buta, Astron. Astrophys. **245**, 7 (1991).
16. Ph. Heraudeau and F. Simien, Astron. Astrophys., Suppl. Ser. **133**, 317 (1998).
17. E. Schinnerer, A. Eskart, and L. J. Tacconi, Astrophys. J. **533**, 826 (2000).
18. H.-P. Reuter, A. W. Sievers, M. Pohl, *et al.*, Astron. Astrophys. **245**, 7 (1991).
19. A. H. Broeils and H. van Woerden, Astron. Astrophys., Suppl. Ser. **107**, 129 (1994).
20. J. A. Garsia-Barreto, F. Combes, B. Koribalski, and J. Franko, Astron. Astrophys. **348**, 685 (1999).
21. M. A. W. Verheijen and R. Sancisi, Astron. Astrophys. **370**, 765 (2001).
22. A. Bosma, R. D. Ekers, and J. Lequeux, Astron. Astrophys. **57**, 97 (1977).
23. W. van Driel, H. van Woerden, U. J. Schwarz, and J. S. Gallagher, Astron. Astrophys. **191**, 201 (1988).
24. D. Woods, G. G. Fahlman, and B. F. Madore, Astrophys. J. **353**, 90 (1990).
25. S. Casertano and J. H. van Gorkom, Astron. J. **101**, 1231 (1991).
26. A. Distefano, R. Rampazzo, G. Chincarini, and R. de Souza, Astron. Astrophys., Suppl. Ser. **86**, 7 (1990).
27. V. C. Rubin, A. H. Waterman, and J. D. P. Kenney, Astron. J. **118**, 236 (1999).
28. B. Volmer, V. Cayatte, A. Boselli, *et al.*, Astron. Astrophys. **349**, 411 (1999).
29. V. C. Rubin, D. Burstein, W. K. Ford, and N. Thonnard, Astrophys. J. **289**, 81 (1985).
30. G. Delgado, M. Rosa, and E. Perez, Mon. Not. R. Astron. Soc. **281**, 1105 (1996).
31. I. Marguez and M. Moles, Astron. Astrophys., Suppl. Ser. **120**, 1 (1996).
32. K. L. Jones, B. S. Koribalski, M. Elmouttie, and R. F. Haynes, Mon. Not. R. Astron. Soc. **302**, 649 (1999).
33. HYPERLEDA: http://www.sai.msu.ru/hypercat.
34. A. M. Fridman, V. L. Afanasiev, S. N. Dodonov, *et al.*, Mon. Not. R. Astron. Soc. (2004, in press).
35. M. A. W. Verheijen, Astrophys. J. **563**, 694 (2001).
36. P. Salucci, Mon. Not. R. Astron. Soc. **320**, L1 (2001).
37. A. V. Zasov, D. V. Bizyaev, D. I. Makarov, and N. V. Tyurina, Pis'ma Astron. Zh. **28**, 599 (2002) [Astron. Lett. **28**, 527 (2002)].
38. A. V. Zasov, A. V. Khoperskov, and N. V. Tyurina, Pis'ma Astron. Zh. **30**, 653 (2004) [Astron. Lett. **30**, 593 (2004)].
39. A. V. Tutukov, Astron. Zh. (2005, in press).
40. T. M. Heckman, G. Kauffmann, J. Brinchmann, *et al.*, Astrophys. J. **613**, 109 (2004).

Translated by D. Gabuzda

Astronomy Reports, Vol. 49, No. 5, 2005, pp. 368–373. Translated from Astronomicheskiĭ Zhurnal, Vol. 82, No. 5, 2005, pp. 414–419.

Analysis of the Color Variability of ON 231 in 1994–2002

V. A. Hagen-Thorn[1], E. I. Hagen-Thorn[1,2], L. O. Takalo[3], and A. Sillanpää[3]

[1] *Astronomical Institute, St. Petersburg University, St. Petersburg, Russia*

[2] *Main (Pulkovo) Astronomical Observatory, St. Petersburg, Russia*

[3] *Tuorla Observatory, University of Turku, Turku, Finland*

Received July 2, 2004; in final form, December 3, 2004

Abstract—We analyze multicolor observations of the blazar ON 231 obtained during coordinated observations in 1994–2002. *On average*, the spectral energy distribution of the variable component in the optical range remains constant, and can be represented by the power law $F_\nu \sim \nu^{-0.85}$. Since the radiation of the blazar is strongly polarized, there is no doubt that the variable emission that is responsible for the activity of the blazar is synchrotron radiation. There are small but significant season-to-season variations in the spectral index. © *2005 Pleiades Publishing, Inc.*

1. INTRODUCTION

The radio source ON 231 was first identified with a starlike object previously known as the variable star W Com in 1971 [1, 2]; W Com had been known to be an optical variable since 1916 [3]. Based on the observed properties of this object, it was suggested that it was an extragalactic source, and it was assigned to the class of BL Lac objects [1, 2], which are characterized by strong optical variability and a lineless continuum. The extragalactic nature of ON 231 was confirmed in 1985, when weak emission lines were detected in its spectrum, making it possible to determine its redshift, $z = 0.102$. Further, an elliptical host galaxy was distinguished [5].

Starting after 1971, ON 231 was included in monitoring observations carried out by a number of observatories. The results of these observations together with data derived from archival material were used by Tosti *et al.* [6] to construct a historical B-band light curve for ON 231 for 1892–1999 (which was subsequently supplemented with additional data in [7]).

In the 1970s and 1980s, the object was near its minimum brightness, and observations were irregular. However, in the middle of the 1990s, its brightness substantially rose, together with interest in the acquisition of new observations, especially after the detection of gamma-ray emission from this object [8, 9]. Beginning in the mid-1990s, coordinated monitoring observations in several bands began, making it possible to analyze the color variability of the sources responsible for the activity of the object. The current paper is devoted to such an analysis, based on BVR_cI_c monitoring data for ON 231 obtained in 1994–2002 and published in [10, 11].

2. OBSERVATIONAL DATA AND ANALYSIS METHOD

The observational data published in [10, 11] were obtained at four observatories. Both papers present averaged (in the case of quasi-simultaneous observations) brightness measurements for ON 231 in magnitudes. Since our analysis method (see below) requires that these data be translated into flux densities (further, for brevity, called simply "fluxes"), we translated the magnitudes into fluxes in mJy using the absolute calibration of Mead *et al.* [12]. Further, all the fluxes in each spectral band for a given Julian date were averaged (in this way, we suppress the influence of possible rapid variability of the object over the course of a night, and restrict our analysis to investigation of the color variability on time scales exceeding a day). Figure 1 presents light curves (in fluxes) constructed from the data used in our color-variability analysis.

The analysis method used is described in detail in our earlier paper [13]. The essence of this method is as follows. If in some time interval the photometric behavior of an object is determined by a single source with a variable flux but constant spectral energy distribution (SED), then the points corresponding to the observed fluxes should lie on a straight line in the N-dimensional space of data obtained in N color bands. With small caveats, the opposite is also true: if the observational data points lie on a straight line in this space, the color characteristics of the variable component are constant; the slope of the line corresponds to the ratio of the fluxes of the *variable* source in the different color bands; i.e., to the source's relative SED. We especially emphasize one important advantage of this method: it is not necessary to first

1063-7729/05/4905-0368$26.00

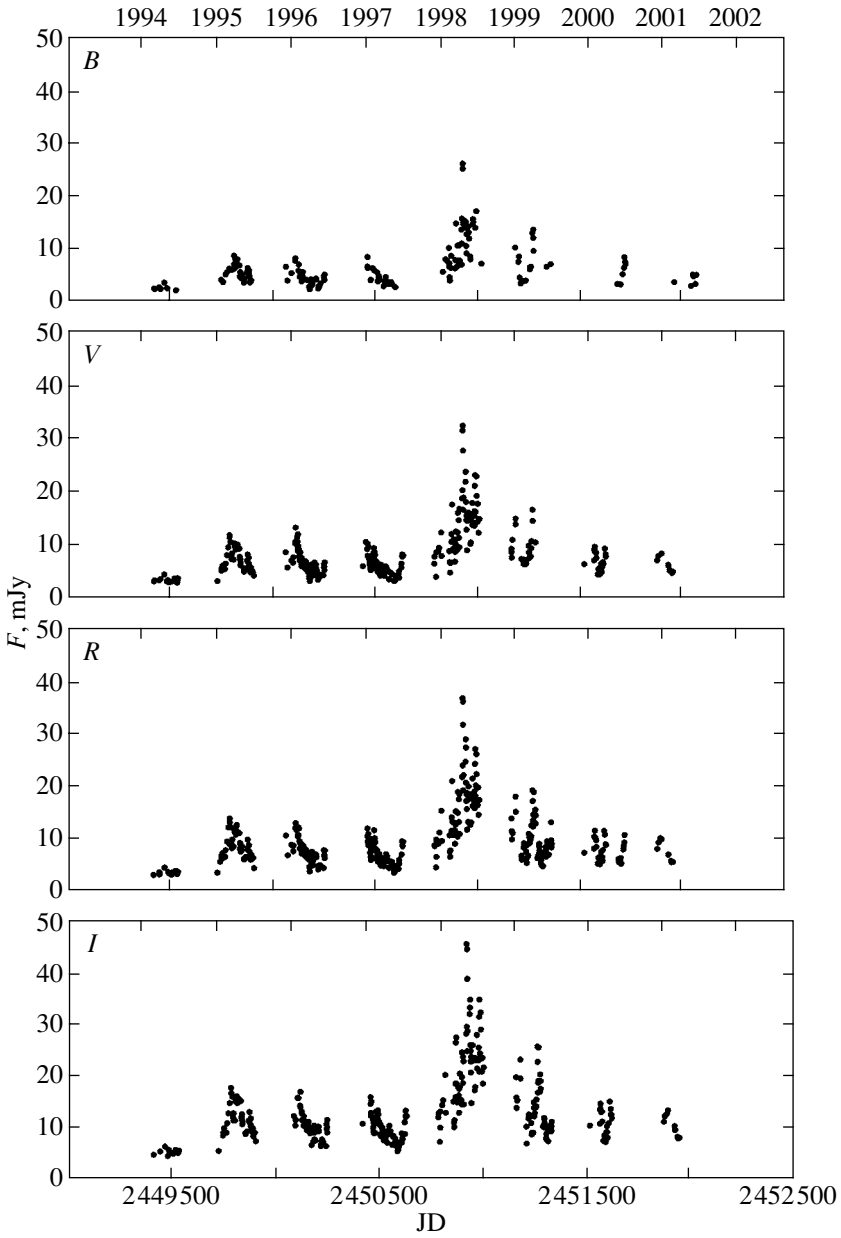

Fig. 1. Light curves of ON 231 (in fluxes) after averaging the data for each Julian date.

determine the contribution of the variable component to the observed radiation before obtaining information about its SED.

In practice, a pairwise comparison of the fluxes is carried out, with one of the two bands being chosen as the "main" band; this is usually the band for which the most observations are available, which is the R_c band in our case (further, the subscript "c" for the R_c and I_c bands will be omitted). The slope of the line in one of the flux–flux diagrams gives the ratio of the flux of the variable source in a given band to its flux in the main band; here, this will be the ratio $(F_i/F_R)_v^{obs}$. Comparison with the effective wavelengths (or frequencies) of the bands yields the *observed* relative SED of the variable component.

If required, the data must be corrected for interstellar reddening. This can be done either before constructing the flux–flux diagrams (in which case the correction is applied to each observed flux, and the resulting relative SED of the variable source is therefore corrected for interstellar reddening) or after constructing these diagrams. In the latter case, a multiplicative correction factor C_{iR} is applied, so that $(F_i/F_R)_v^{corr} = C_{iR}(F_i/F_R)_v^{obs}$.

We used the second approach (Table 1). According to [10], $A_V = 0.11^m$ in the direction of ON 231. Using

Table 1. Correction for interstellar absorption

Band	λ_e, μm	τ_{λ_e}	A_i	F^{corr}/F^{obs}	C_{iR}
B	0.44	1.32	0.15^m	1.15	1.05
V	0.55	1.00	0.11	1.11	1.02
R	0.64	0.84	0.09	1.09	1.00
I	0.79	0.62	0.07	1.07	0.98

the normal interstellar extinction curve [14] (third column in Table 1), we determined the absorption in the other bands (fourth column), then the ratio of the fluxes F_{corr}/F_{obs} (fifth column), and the factor C_{iR} (sixth column).

3. RESULTS FOR THE ENTIRE TIME INTERVAL

The flux–flux diagrams for the entire set of observational data are presented in Fig. 2; the filled symbols denote the data for the 1997–1998 season, when the largest flare ever observed in ON 231 was recorded (to avoid overlap in the diagram, the B curve has been shifted downward by five units). Figure 2 shows that all of the dependences $\langle\langle F_i - F_R\rangle\rangle$ can be well fit by straight lines; the correlation coefficients, given in the third column of Table 2, are all close to unity. This indicates that, *on average*, considering the entire interval, the SED of the variable component is constant.

The results of our analysis are presented in Table 2. The first and second columns indicate the band and corresponding logarithm of the frequency, the fourth the number of points on each of the plots, and the fifth the slopes of the straight lines and their 1σ errors (the lines were fit using the method of orthogonal regression [15], which is appropriate when there are random errors in both quantities plotted). This column presents the observed flux ratios for the variable source, $(F_i/F_R)_v^{obs}$. The sixth column gives the flux ratios after correction for reddening in the Galaxy—the relative SED of the variable component.

The seventh column of Table 2 gives the logarithms of the corrected flux ratios, which are plotted together with the logarithms of the band frequencies in Fig. 3. We can see that the points lie on a straight line (the corresponding correlation coefficient is 0.98), so that the SED of the variable source is a power law ($F_\nu \sim \nu^\alpha$). The line was found via a least-squares fit taking into account the errors in the individual values. The slope of the best-fit line (the spectral index) is $\alpha = -0.85 \pm 0.09$.

4. RESULTS FOR INDIVIDUAL SEASONS

A careful inspection of Fig. 2 suggests that the slopes of the lines for individual seasons may be somewhat different. Indeed, the filled symbols showing the data for the 1997–1998 season indicate the presence of an additional source in this season

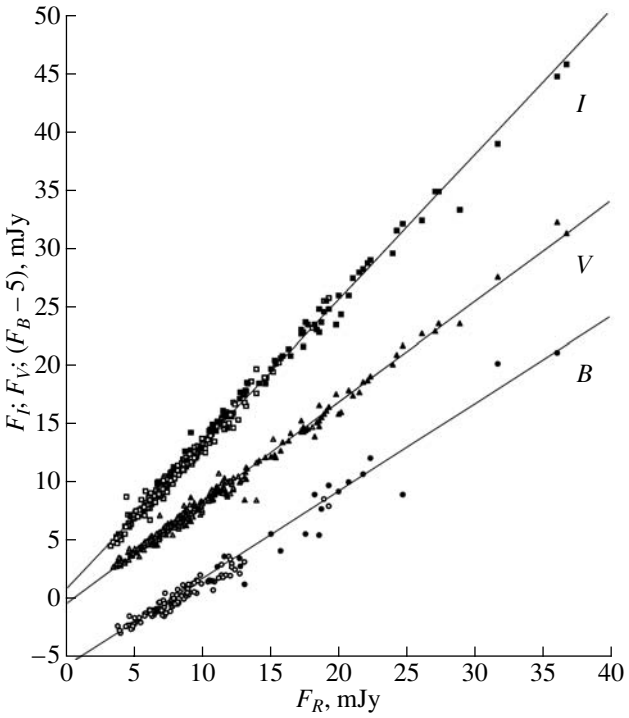

Fig. 2. Comparison of observed fluxes in the BVI_c bands with the flux in the R_c band. The dark symbols denote data for the 1997–1998 season.

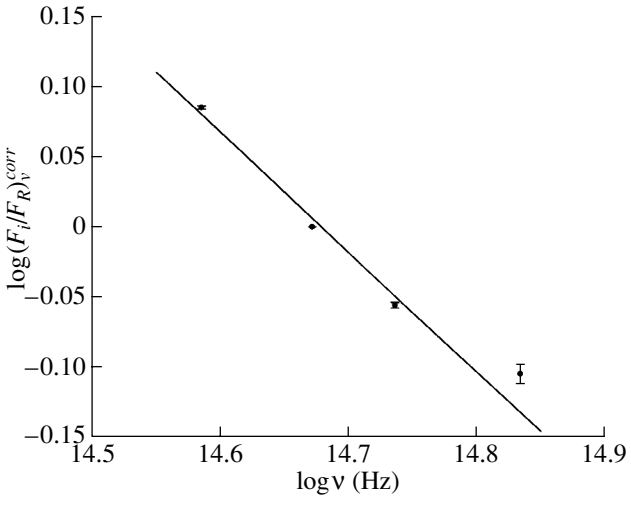

Fig. 3. Relative SED of the variable source (using the entire set of observational data).

Table 2. Results for the entire observational data set

Band	$\log\nu$	r_{iR}	n	$(F_i/F_R)_v^{obs} \pm \sigma$	$(F_i/F_R)_v^{corr} \pm \sigma$	$\log(F_i/F_R)_v^{corr} \pm \sigma$
B	14.834	0.96	132	0.748 ± 0.011	0.785 ± 0.012	-0.105 ± 0.007
V	14.737	0.99	316	0.863 ± 0.004	0.880 ± 0.004	-0.056 ± 0.002
R	14.672			1.000	1.000	0.000
I	14.585	0.99	338	1.240 ± 0.003	1.215 ± 0.003	0.085 ± 0.001

Table 3. Results for individual seasons

Season	$(F_B/F_R)_v^{obs}, (\sigma)$ $r_{BR}, (n)$	$(F_V/F_R)_v^{obs}, (\sigma)$ $r_{VR}, (n)$	$(F_I/F_R)_v^{obs}, (\sigma)$ $r_{IR}, (n)$
1994–1995	0.705, (0.039)	0.883, (0.014)	1.210, (0.014)
	0.89, (38)	0.98, (50)	0.98, (49)
1995–1996	0.625, (0.025)	0.823, (0.012)	1.280, (0.014)
	0.96, (36)	0.98, (62)	0.98, (51)
1996–1997	0.798, (0.023)	0.863, (0.017)	1.264, (0.021)
	0.98, (24)	0.96, (71)	0.96, (56)
1997–1998	0.825, (0.037)	0.889, (0.009)	1.185, (0.008)
	0.94, (23)	0.99, (69)	0.99, (70)
1998–1999	0.770, (0.046)	0.900, (0.041)	1.287, (0.011)
	0.98, (7)	0.93, (24)	0.99, (53)

that was bluer (there is a small break in the corresponding direction in all three flux–flux diagrams near $F_R \approx 15$ mJy). Accordingly, we carried out an analysis analogous to the analysis described in the previous section for each season in which there was a sufficiently large amount of data.

The results are presented in Table 3, where each entry indicates the slope of a line on a flux–flux diagram, its 1σ error, the corresponding correlation coefficient, and the number of observations. The correlation coefficients were all close to unity; i.e., the relations between the fluxes are linear and there are no evident color variations for the variable component within each season. We can see that the variable component is indeed bluer in the 1997–1998 season and redder in the 1995–1996 season, with this difference being substantial (the 3σ intervals for the quantity $(F_i/F_R)_v^{obs}$ for these two seasons do not overlap).

The relative SEDs (after correction for reddening in the Galaxy) are presented on a logarithmic scale in Fig. 4, with the different seasons shown by different symbols. Least-squares lines fit to the data for each season taking into account the indicated errors are also shown. The values for the spectral indices are given in Table 4.

5. DISCUSSION

The results for the entire time interval show that, *on average*, the SED of the variable source in ON 231 remains constant when the flux varies. The spectrum of this variable source is a relative shallow power law (Fig. 3). The spectral indices for most of the other blazars we have studied have magnitudes between 1.3 and 2.5 [16] (the only exception is 3C 66A, whose spectral index is 0.92 ± 0.12 [17]). The power-law spectrum and high degree of polarization in the optical [6] leave no doubt that the variable source has a synchrotron nature.

We have used the method described in [13] in order to distinguish the contribution of the constant and variable components in the total radiation, assuming that the constant component represents the radiation of a giant elliptical galaxy. On a flux–flux diagram, the points corresponding to galaxies with a given color index lie on a ray going outward from the coordinate origin, whose slope is determined by the color index of the galaxies. The coordinates of the point where

Table 4. Spectral indices for the variable sources in various seasons

Season	α, (σ_α)
1994–1995	−0.81 (0.02)
1995–1996	−1.14 (0.01)
1996–1997	−0.75 (0.16)
1997–1998	−0.62 (0.10)
1998–1999	−0.89 (0.11)

this ray intersects the straight line corresponding to the observed fluxes yields the fluxes of the constant component. We found the slope of the ray using the colors of a giant elliptical galaxy, taking into account interstellar reddening and the redshift of the galaxy. Applying this procedure to the flux–flux diagrams for the BVR bands yielded for the constant component $B = 17.46^m$, $V = 16.10^m$, and $R = 15.50^m$. (Note that if the constant component has this brightness, the dependence of the spectral index of the variable source on the flux found by Tosti *et al.* [10] disappears.) However, there are data in the literature that indicate a magnitude for ON 231 exceeding $V = 16.10^m$ [18]. This suggests that, in addition to the contributions of the galaxy and the variable component we have distinguished, the radiation of the object includes a contribution from an additional slowly-varying component. The multicomponent structure of the historical light curve of ON 231 was noted in [7].

Analysis of the photometric data within individual seasons indicates that, during flux variations, the points corresponding to individual series of observations are shifted in the flux–flux diagrams precisely along the straight line on which they lie. In other words, there is no difference between the data for the ascending and descending branches of the light curve. Generally speaking, an absence of evolution of the SED is not expected in the usually adopted model in which a shock propagates along a jet; in this model, the spectrum of the jet becomes steeper as the brightness decreases, due to synchrotron losses. The observed behavior is expected if the flux variations are due to variations in the quantity of relativistic electrons in the source [16] or in the directions of their motion relative to the line of sight [19].

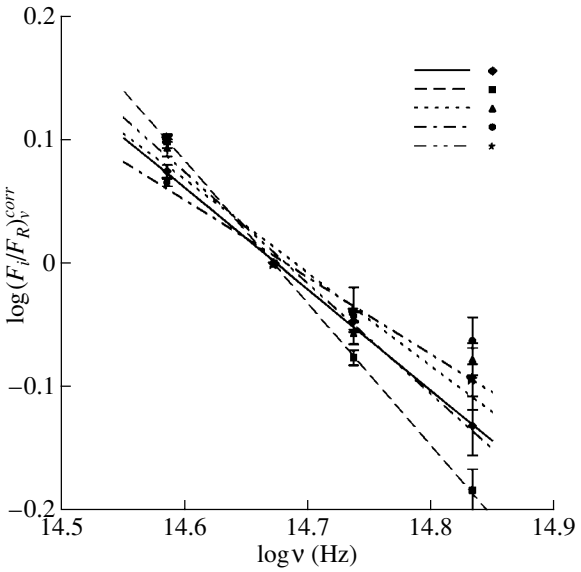

Fig. 4. Relative SED of the variable sources for various observing seasons.

In Table 4, the differences in the errors in the spectral indices for different seasons are striking. Figure 4 shows that large errors are associated with excess radiation in the B band in three seasons (just before, during and after the strong flare). Note that, at the redshift of ON 231 ($z = 0.102$), radiation with $\lambda < 0.4$ μm—i.e., the region of the "blue bump"—falls into the B band. It is possible that this appearance of excess radiation is somehow related to the high activity of the object in the 1997–1998 season. Unfortunately, there are no monitoring observations of ON 231 in the U band that could be used to test this idea.

6. CONCLUSION

Thus, our analysis shows that the spectral energy distribution of the variable source in ON 231 *on average* remained constant over eight observing seasons, and could be represented by the power law $F_\nu \sim \nu^{-0.85}$. However, there were small but significant variations in the spectral index from season to season, with the SED of the variable source remaining constant within each season. This suggests that the lifetimes of individual variable sources are of the order of a season, and that the characteristics of the individual sources are only slightly different from each other. More accurate and uniform data in not only the optical, but also the infrared and ultraviolet, are required to elucidate the origin of the observed properties of this object.

ACKNOWLEDGMENTS

V.A.H-Th. and E.I.H-Th. thank the Tuorla Observatory (Finland) for hospitality, and L.O.T. and A.S. thank the Finnish Academy of Sciences for support of this research. This work was partially supported by the Federal Science and Technology Program in Astronomy (grant no. 40.022.1.1.1001).

REFERENCES

1. I. W. A. Brown, Nature **231**, 515 (1971).
2. F. Biraud, Nature **232**, 178 (1971).
3. M. Wolf, Astron. Nachr. **202**, 415 (1916).
4. D. Weistrop, D. B. Shaffer, P. Hintzen, and W. Romanishin, Astrophys. J. **292**, 614 (1985).
5. R. Wurtz, J. T. Stocke, and H. K. C. Yee, Astrophys. J., Suppl. Ser. **103**, 109 (1996).
6. G. Tosti, M. Fiorucci, M. Luciani, *et al.*, Astron. Soc. Pac. Conf. Ser. **159**, 149 (1999).
7. M. K. Babadzhanyants and E. T. Belokon', Astron. Zh. **79**, 675 (2002) [Astron. Rep. **46**, 609 (2002)].
8. C. von Montigni, D. L. Bertsch, J. Chiang, *et al.*, Astrophys. J. **440**, 525 (1995).
9. P. Sreekumar, D. L. Bertsch, B. L. Dingus, *et al.*, Astrophys. J. **464**, 628 (1996).
10. G. Tosti, M. Fiorucci, M. Luciani, *et al.*, Astron. Astrophys. **130**, 109 (1998).
11. G. Tosti, E. Massaro, R. Nesci, *et al.*, Astron. Astrophys. **395**, 11 (2002).
12. A. R. G. Mead, K. R. Ballard, P. W. J. L. Brand, *et al.*, Astron. Astrophys. **83**, 183 (1990).
13. V. A. Hagen-Thorn and S. G. Marchenko, Baltic Astron. **8**, 575 (1999).
14. J. A. Cardelli, G. C. Clayton, and J. S. Mathis, Astrophys. J. **345**, 245 (1989).
15. A. Wald, Ann. Math. Stat. **11**, 284 (1940).
16. V. A. Hagen-Thorn, S. G. Marchenko, and O. V. Mikolaichuk, Astrofizika **32**, 429 (1990) [Astrophys. **32**, 244 (1990)].
17. V. A. Hagen-Thorn, A. V. Hagen-Thorn, S. G. Ershtadt, *et al.*, Astrofizika **44**, 347 (2001) [Astrophys. **44**, 283 (2001)].
18. P. Battistini, A. Braccesi, and L. Formiggini, Astron. Astrophys. **35**, 93 (1974).
19. M. Camenzind and M. Krockenberger, Astron. Astrophys. **255**, 59 (1992).

Translated by D. Gabuzda

Astronomy Reports, Vol. 49, No. 5, 2005, pp. 374–389. Translated from Astronomicheskiĭ Zhurnal, Vol. 82, No. 5, 2005, pp. 420–436.

Spectral Studies with the Special Astrophysical Observatory 6 m and RATAN-600 Telescopes

V. L. Afanas'ev[1], S. N. Dodonov[1], A. V. Moiseev[1], A. G. Gorshkov[2], V. K. Konnikova[2], and M. G. Mingaliev[1]

[1] *Special Astrophysical Observatory, Russian Academy of Sciences, Nizhniĭ Arkhyz, Karachaĭ-Cherkessian Republic, 357147 Russia*

[2] *Sternberg Astronomical Institute, Universitetskiĭ pr. 13, Moscow, 119899 Russia*

Received September 17, 2004; in final form, December 3, 2004

Abstract—We present optical identifications, classifications, and radio spectra for 19 radio sources from a complete sample in flux density with declinations 10°–12°30′ (J2000) obtained with the 6-m optical telescope (4000–9000 Å) and RATAN-600 radio telescope (0.97–21.7 GHz) of the Special Astrophysical Observatory. Twelve objects with redshifts from 0.573 to 2.694 have been classified as quasars, and two objects with featureless spectra as BL Lac objects. Four objects are emission-line radio galaxies with redshifts from 0.204 to 0.311 (one also displaying absorption lines), and one object is an absorption-line galaxy with a redshift of 0.214. Radio flux densities have been obtained at six frequencies for all the sources except for two extended objects. The radio spectra of five of the sources can be separated into extended and compact components. Three objects display substantial rapid (on time scales from several days to several weeks) and long-term variability of their flux densities. © *2005 Pleiades Publishing, Inc.*

1. INTRODUCTION

We present optical and radio spectra for nineteen radio sources from a complete sample in flux density having declinations 10°–12°30′ (J2000), right ascensions 0–24^h, and $|b| > 15°$. The sample was selected from the GB6 catalog [1] and contains 153 sources with flux densities above 200 mJy at 4.85 GHz [2]. We have identifications with optical objects down to 21^m for 86% of the sources with flat spectra, $\alpha_{(3.9-7.7)} > -0.5$ ($S \propto \nu^\alpha$), and 60% of the sources with steep spectra $\alpha_{(3.9-7.7)} < -0.5$.

It is necessary to obtain the redshifts of the sample sources in preparation for constructing the corresponding quasar luminosity function. Including our new results presented here, 88% of all identified sample sources have now been classified. A substantial number of the objects had been classified earlier [3]; our own previous classifications are presented in [4, 5]. The sample has been monitored in the radio since 2000.

2. RADIO AND OPTICAL OBSERVATIONS

Optical spectra of all the objects were obtained with the 6-m telescope of the Special Astrophysical Observatory (SAO) of the Russian Academy of Sciences in 2001–2002. We used the multipurpose SCORPIO spectrograph [6] in its long-slit mode with a TK1024 CCD detector (1024×1024 pixels, readout noise 3 el.). The spectral range of the spectrograph is 3800 to 9200 Å, with the dispersion being approximately 6 Å/pixel. The effective instrumental resolution was roughly 20 Å. The spectra were processed in the standard way using software developed in the Laboratory for Spectroscopy and Photometry of the SAO.

The radio observations were carried out with the RATAN-600 telescope. Seven sources were observed as part of a monitoring program to study flux-density variability on time scales of several days to several weeks. These sources were observed daily using the North sector of the RATAN-600 during September 6–November 26, 2000 (82 days), June 5–September 10, 2001 (98 days), and June 19–September 23, 2002 (97 days).

The radio flux densities of the other sources were obtained during May 31–June 4, 2001, October 31–November 19, 2001, and June 6–10, 2002 on the North sector and during October 31–November 19, 2003 on the South sector, using the flat reflector. The 2000 and 2001 observations were carried out at 0.97, 2.3, 3.9, 7.7, 11.1, and 21.7 GHz, while 0.97 GHz was excluded from the 2002 and 2003 observations. The parameters of the detectors and beams are given in [7]. A beam-modulation regime was employed at 7.7, 11.1, and 21.7 GHz.

1063-7729/05/4905-0374$26.00

Table 1. Coordinates of the objects

Radio coordinates (J2000)		Optical–radio		R	B	Reference to survey
RA	DEC	Δ RA	Δ DEC			
$01^h\ 43^m\ 31.093^s$	12° 15′ 42.95″	-0.013^s	0.07″	19.75	20.55	JVAS
02 42 29.171	11 01 00.72	−0.006	0.57	19.55		JVAS
03 15 21.039	10 12 43.12	0.081	0.09	18.69	19.89	NVSS
04 44 12.467	10 42 47.29	0.010	−0.03	18.50	19.00	JVAS
04 48 50.413	11 27 54.39	−0.001	0.21	19.08	20.01	JVAS
04 49 07.672	11 21 28.63	−0.029	0.14	18.38	20.46	JVAS
05 09 27.457	10 11 44.59	−0.001	0.08	18.53	19.18	JVAS
05 16 46.646	10 57 54.77	−0.016	0.23	17.96	19.13	JVAS
07 49 27.385	10 57 33.12	0.002	0.16	18.87	19.59	JVAS
07 58 07.658	11 36 46.05	0.072	1.80	15.95	16.29	JVAS
09 14 19.360	10 06 38.28	0.166	2.45	18.65	20.88	NVSS
13 27 54.707	12 23 08.71	−0.010	1.09	19.44	19.78	NVSS
14 53 44.241	10 25 57.57	0.003	−0.40	19.49	20.78	JVAS
15 22 12.151	10 41 30.35	0.085	−0.35	18.01		NVSS
16 27 37.032	12 16 07.11	−0.003	0.07	18.89	19.04	JVAS
17 22 44.582	10 13 35.77	−0.005	0.26		20.94	JVAS
17 28 07.051	12 15 39.48	0.007	0.55		20.88	JVAS
23 12 10.467	12 24 03.46	−0.031	−0.64	18.90	19.10	NVSS
23 15 34.250	10 27 18.57	0.095	0.05	16.92	19.27	TEXAS

The processing of the radio data is described in [2, 8]. The calibration was carried out using observations of J1347+1217, whose angular size is substantially smaller than the horizontal cross-section of the beams at all the frequencies observed. We adopted flux densities of 6.15, 4.12, 3.23, 2.36, 1.99, and 1.46 Jy at 0.97, 2.3, 3.9, 7.7, 11.1, and 21.7 GHz, respectively, for this source.

3. RADIO AND OPTICAL COORDINATES

Columns 1 and 2 of Table 1 present the J2000 coordinates of the studied objects taken from the Jodrell Bank–VLA Astrometric Survey (JVAS) catalog at 8.4 GHz [9] or the NRAO VLA Sky Survey (NVSS) catalog at 1.4 GHz [10]. The rms errors of the JVAS coordinates σ are 0.014″, while the rms errors for the NVSS coordinates are typically 0.5″. The object J2315+1027 is a double source in the NVSS; the optical object is situated at the position corresponding to the weighted average of the coordinates of the two radio sources, close to the coordinates given in the Texas Survey at 0.365 GHz [11]. Columns 3 and 4 contain the differences between the optical coordinates from the USNO astrometric survey [12] and the radio coordinates. Columns 5 and 6 present the USNO R and B magnitudes, and column 7 gives references for the coordinates. The object J0914+1006 is a double or triple source with a total extent of no less than 30″, and the difference between its optical and NVSS coordinates is substantial.

4. RESULTS

Figures 1–4 present the optical spectra of the objects, Figs. 5, 6 the radio spectra, and Table 2 data from the optical observations. The columns present (1) the name of the object, (2) the spectral lines observed, (3) their wavelengths in the rest frame of the source and as observed, (4) the redshift, (5) the spectral class, (6) the date of the observations, and (7) the exposure time in minutes. Lines marked with

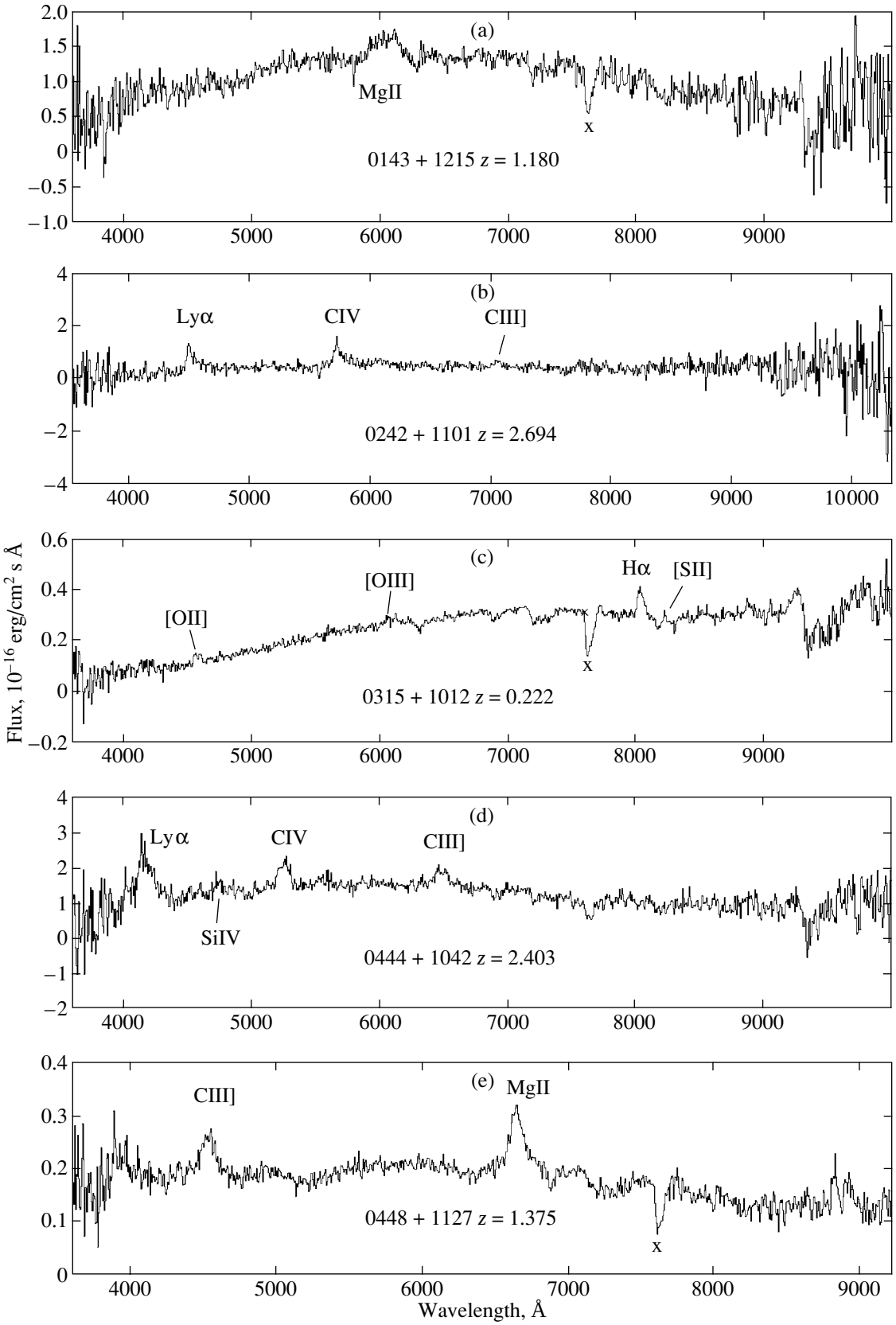

Fig. 1. Optical spectra of the radio sources J0143+1215, J0242+1101, J0315+1012, J0444+1042, and J0448+1127 obtained using the SAO 6 m telescope.

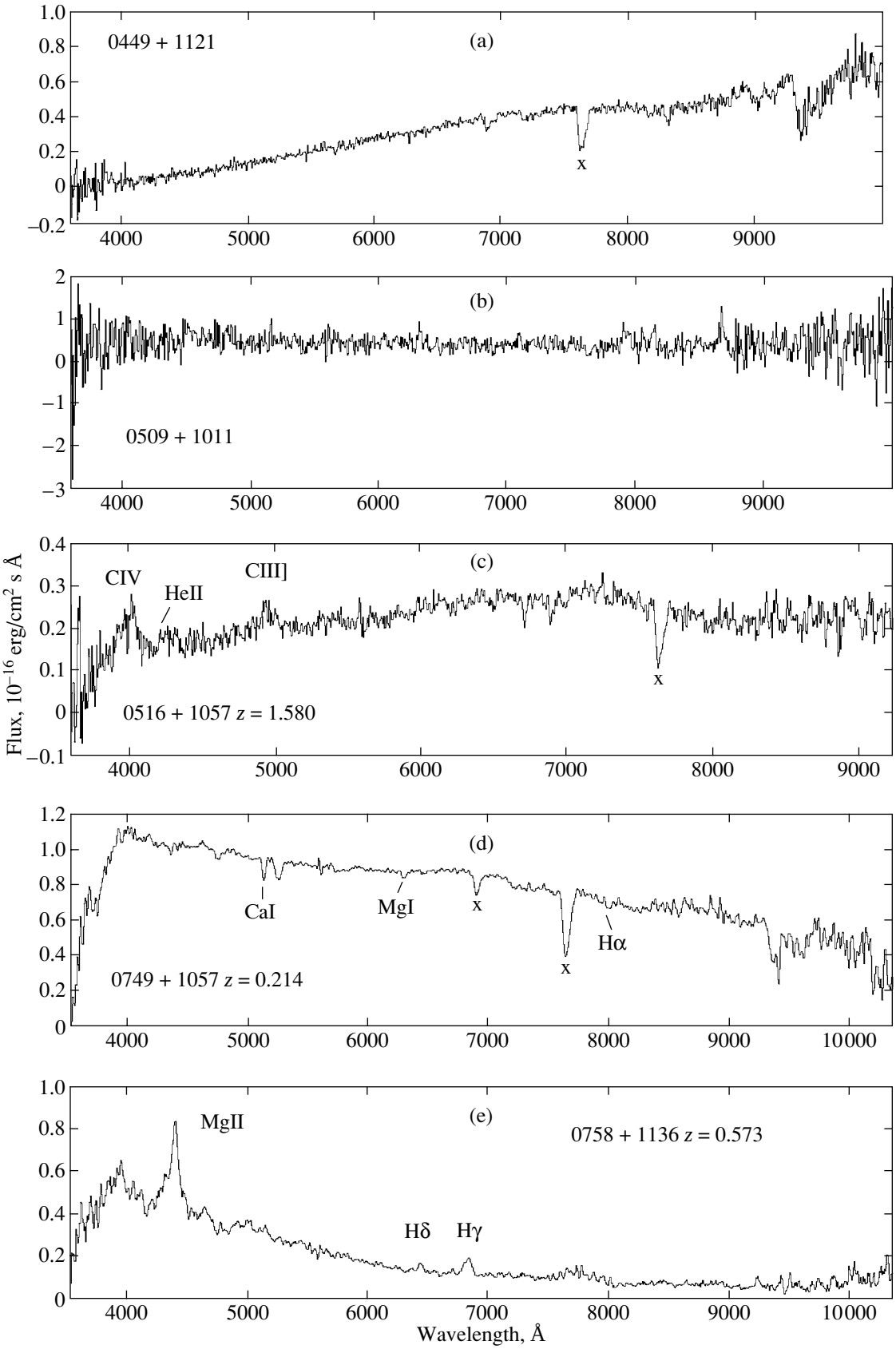

Fig. 2. Same as Fig. 1 for J0449+1121, J0509+1011, J0516+1057, J0749+1057, and J0758+1136.

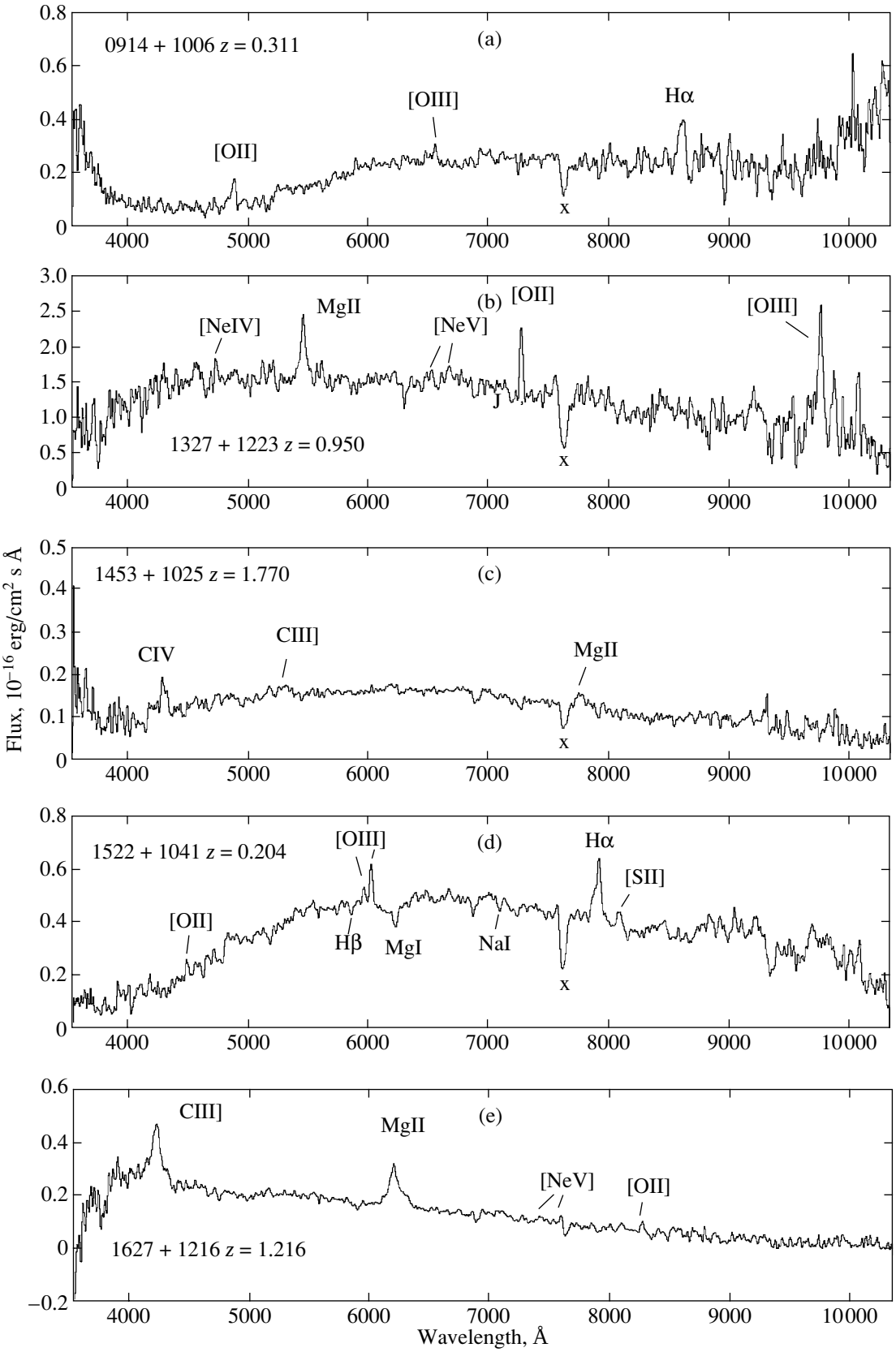

Fig. 3. Same as Fig. 1 for J0914+1006, J1327+1223, J1453+1025, J1522+1041, and J1627+1216.

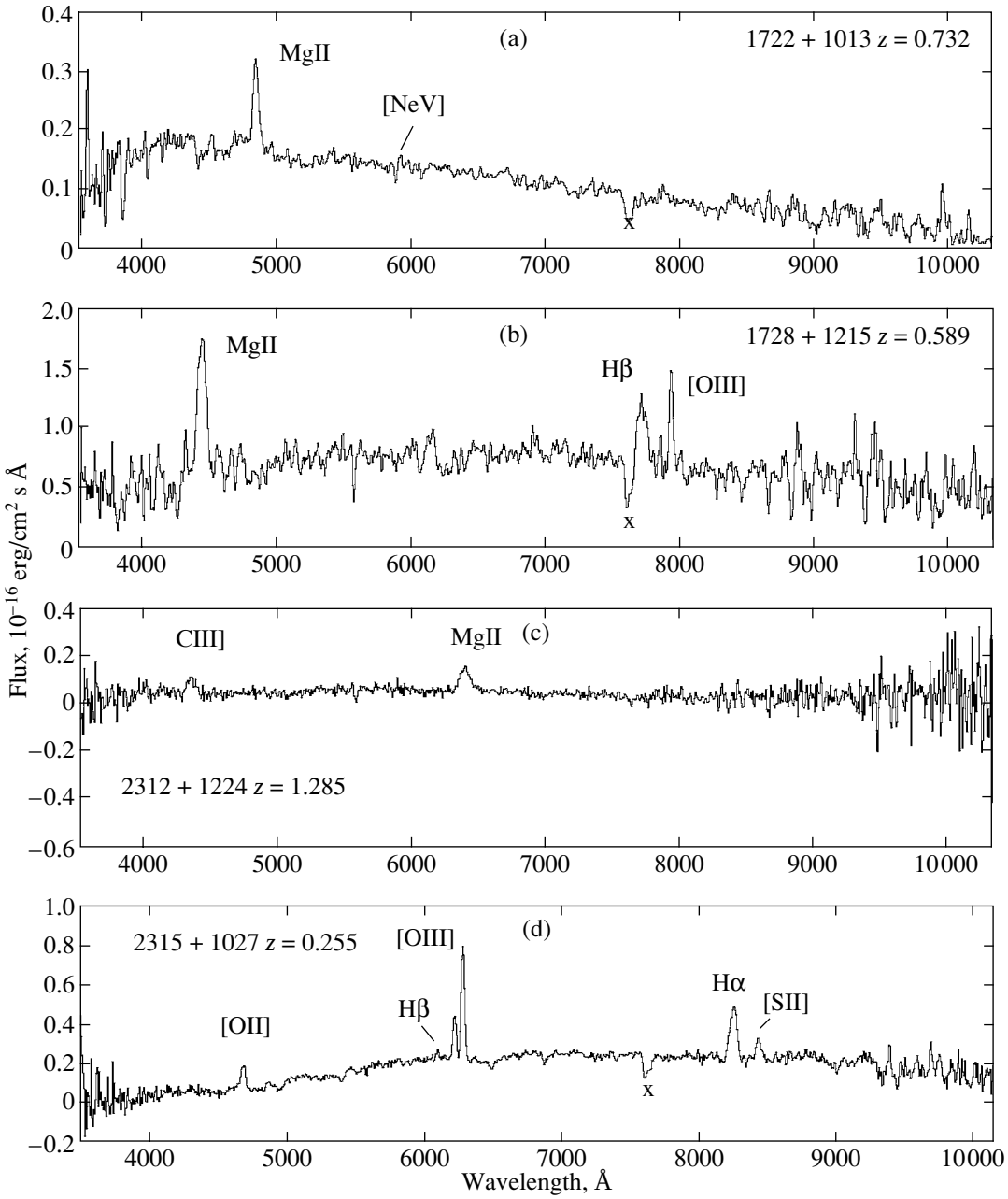

Fig. 4. Same as Fig. 1 for J1722+1013, J1728+1215, J2312+1224, and J2315+1027.

asterisks were observed in absorption, and the remaining lines in emission.

Table 3 contains the radio flux densities of the sources averaged over the observations, and presents the name of the object, the flux densities at 0.97, 2.3, 3.9, 7.7, 11.1, and 21.7 GHz in mJy and their rms errors, and the dates to which the flux densities correspond.

Observational data for variable sources are presented for multiple epochs.

Below, we discuss the optical spectrum and object classification of each object, together with the parameters of the radio spectrum.

When a non-power-law spectrum was observed, we attempted to separate it into an extended component with a power-law spectrum, $S = S_o\nu^\alpha$, and a compact component whose spectrum could be represented by a logarithmic parabola, $\log S = S_o + B\log\nu + C\log^2\nu$. The method used to separate the two components in the spectra is described in detail in [2]. This procedure also took into account the 365 MHz (Texas Survey) and 1400 MHz (NVSS) flux densities.

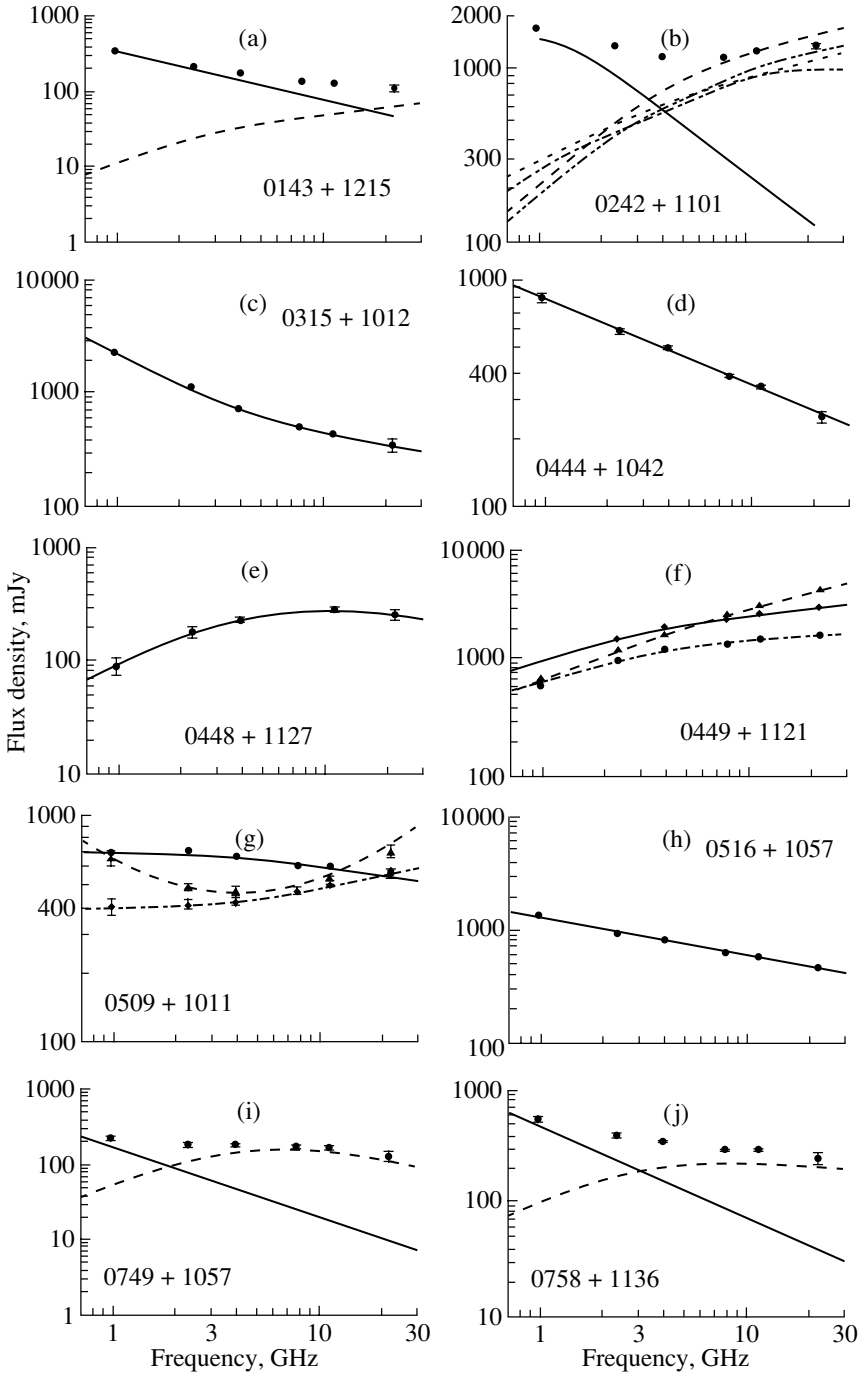

Fig. 5. Radio spectra of J0143+1215, J0242+1101, J0315+1012, J0444+1042, J0448+1127, J0449+1121, J0509+1011, J0516+1057, J0749+1057, and J0758+1136.

If the flux density of a radio source varied either from one set of observations to another or within a single set of observations, we present the parameters of the variations. For some of the sources, the relative variability amplitude is given, $V = (S_{\max} - S_{\min})/(S_{\max} + S_{\min})$. For sources with variability time scales shorter than a month, we present the modulation index m, which is defined as the ratio of the standard deviation of the variable component and the average flux density in percent.

4.1. J0143+1215

A single broad emission line is seen in the optical spectrum (Fig. 1a), interpreted as MgII 2798 Å at a redshift of $z = 1.18$. We classify this object as a

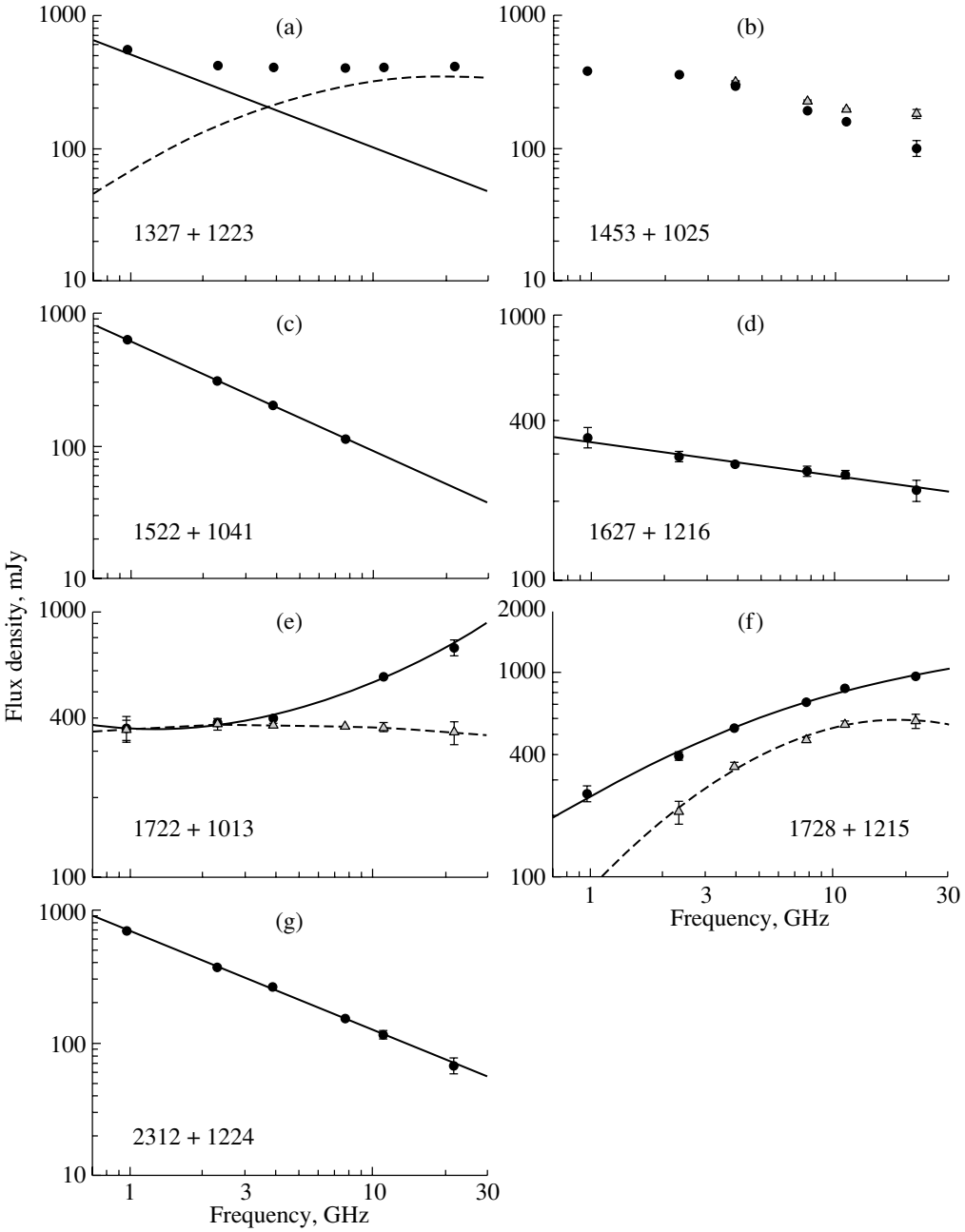

Fig. 6. Same as Fig. 5 for J1327+1223, J1453+1025, J1522+1041, J1627+1216, J1722+1013, J1728+1215, and J2312+1224.

quasar. Quasars with redshifts $z \approx 1$ usually display strong CIII] 1909 Å emission; here, however, this line is located in a noisy part of the spectrum and is not visible.

We obtained radio observations of this source in 2000, 2001, and 2002. The flux densities at all frequencies remained constant within 3σ. The spectrum falls off with frequency, flattening at high frequencies.

We were able to fit two components in the spectrum. The extended component is best fit by the power law $S = 350\,\nu^{-0.65}$ starting from 0.365 GHz. The compact component is best fit by the logarithmic parabola $\log S = 1.069 + 0.982 \log \nu - 0.322 \log^2 \nu$. The compact component is optically thick in our frequency range; the maximum flux density ($S_{\max} =$ 65 mJy) is near 35 GHz. The extended component dominates the radiation at 0.97–7.7 GHz, the flux densities of the extended and compact components are comparable at ≈13 GHz, and the radiation of the compact component begins to dominate at higher frequencies. The observed spectrum is indicated by the

Table 2. Optical data

Object	Spectral lines	Wavelength, Å	z	Spectral type	Date	Exposure time, min
J0143+1215	MgII	2798/6100	1.180	QSO	16.09.01	20
J0242+1101	Lyα	1216/4490	2.694	QSO	18.10.01	10
	CIV	1549/5720				
	CIII]	1909/7055				
J0315+1012	[OII]	3727/4550	0.222	Em. G	16.09.01	20
	Hα	6563/8020				
	[SII]	6717/8210				
J0444+1042	Lyα	1216/4140	2.403	QSO	16.09.01	16.7
	SiIV	1403/4760				
	CIV	1549/5265				
	CIII]	1909/6500				
J0448+1127	CIII]	1909/4530	1.375	QSO	15.10.01	20
	MgII	2798/6650				
J0449+1121				Lac	21.09.01	10
J0509+1011				Lac	18.10.01	10
J0516+1057	CIV	1549/4000	1.580	QSO	15.10.01	10
	HeII	1640/4215				
	CIII]	1909/4920				
J0749+1057	CaI*	4227/5130	0.214	Abs.G	15.10.01	20
	MgI*	5175/6280				
	Hα*	6563/7970				
J0758+1136	MgII	2798/4400	0.569	QSO	06.02.02	6
	Hδ	4102/6435				
	Hγ	4340/6825				
J0914+1006	[OII]	3727/4890	0.311	Em.G	06.02.02	10
	[OIII]	5007/6560				
	Hα	6563/8605				
J1327+1223	[NeIV]	2424/4725	0.950	QSO	12.05.02	10
	MgII	2798/5460				
	[NeV]	3346/6525				
	[NeV]	3426/6680				
	[OII]	3727/7270				
	[OIII]	4958/9670				
	[OIII]	5007/9760				
J1453+1025	CIV	1549/4295	1.773	QSO	08.02.02	20
	CIII]	1909/5290				
	MgII	2798/7760				

Table 2. (Contd.)

Object	Spectral lines	Wavelength, Å	z	Spectral type	Date	Exposure time, min
J1522+1041	[OII]	3727/4485	0.204	Em.G	12.05.02	10
	Hβ*	4861/5850				
	[OIII]	4958/5970				
	[OIII]	5007/6030				
	MgI*	5175/6230				
	NaI*	5893 /7095				
	Hα	6563/7903				
	[SII]	6724/8095				
J1627+1216	CIII]	1909/4228	1.216	QSO	11.05.02	10
	MgII	2798/6200				
	[NeV]	3426/7592				
	[OII]	3727/8260				
J1722+1013	MgII	2798/4845	0.732	QSO	11.05.02	10
	[NeV]	3426/5935				
J1728+1215	MgII	2798/4446	0.589	QSO	04.06.02	20
	Hβ	4861/7725				
	[OIII]	5006/7955				
J2312+1224	CIII]	1909/4360	1.285	QSO	18.10.01	10
	MgII	2798/6400				
J2315+1027	[OII]	3727/4680	0.255	Em.G	20.09.01	20
	Hβ	4861/6100				
	[OIII]	4958/6220				
	[OIII]	5007/6285				
	Hα	6563/8240				
	[SII]	6717/8430				

filled circles in Fig. 5a, with the sizes corresponding to the observational errors. The spectra of the extended and compact components are marked by the solid and dashed curves, respectively.

4.2. J0242+1101

We were able to identify three emission lines in the optical spectrum (Fig. 1b): Lyα 1216 Å, CIV 1549 Å, and CIII] 1909 Å. The redshift derived from these lines is 2.694. The object is a quasar. The Lyα line is usually stronger in radio quasars; the object may be a broad-absorption-line (BAL) quasar, with absorption in the vicinity of the nucleus partially weakening the line emission. This is also suggested by the asymmetry of the Lyα and CIV lines.

Radio observations were obtained four times in 2000–2003. All of the spectra display a minimum in the range from 3 GHz (2002) to 7.5 GHz (2000). The largest flux-density variation was detected at 21.7 GHz, from 1157 ± 15 in October 2000 to 1735 ± 20 in August 2002.

We were able to fit two components in the observed spectra. The strong extended component is best fit by the power law $S = 1930\,\nu^{-0.89}$ at 2.3–21.7 GHz; the parameters of this spectrum remained essentially constant at all observing epochs. The spectrum becomes self-absorbed at lower frequencies, with the

Table 3. Radio data

Object	Flux density with its error, mJy												Epoch
	0.97 GHz		2.3 GHz		3.9 GHz		7.7 GHz		11.1 GHz		21.7 GHz		
J0143+1215	348	10	220	06	175	03	136	04	128	02	110	10	23.07.2001
J0242+1101	1737	35	1383	17	1202	07	1082	09	1144	06	1157	15	16.10.2000
	1660	28	1340	08	1170	04	1167	06	1265	05	1378	22	23.07.2001
			1380	10	1301	04	1380	07	1507	10	1735	20	06.08.2002
			1372	40	1201	10	1106	09	1185	10	1270	50	12.09.2003
J0315+1012	2180	25	1120	20	725	08	491	09	427	14	350	45	15.11.2001
J0444+1042	820	32	596	18	500	13	377	05	340	08	250	30	15.11.2001
J0448+1127	92	15	178	15	230	11			280	11	260	20	04.11.2001
J0449+1121	430	30	1070	15	1324	19	1461	97	1654	78	1788	08	16.10.8000
	687	18	1285	10	1739	99	2671	20	3236	25	4429	34	03.07.2001
			1603	11	2035	19	2463	18	2807	72	3130	30	16.08.7001
			6871	38	1898	13	1595	13	2324	13	2782	61	12.09.2073
J0509+1011	676	18	695	16	662	08	598	05	597	01	547	15	16.10.2000
	682	11	558	10	464	04	437	05	488	01	661	21	23.02.2001
	394	52	205	20	418	14	467	17	697	08	560	35	15.11.2001
			982	26	650	05	401	08	980	08	646	08	12.09.2003
J0516+1057	1330	20	940	12	820	05	652	04	587	04	490	12	23.07.2001
			1007	30	877	07	578	06	481	12	370	35	12.09.2003
J0749+1057	219	25	180	15	182	04	169	09	165	11	126	15	04.11.2001
J0758+1136	557	30	393	20	346	05	298	07	294	07	250	20	04.11.2001
J0914+1006	420	30	260	23									02.06.2001
J1327+1223	560	30	420	15	411	09	405	10	409	08	415	20	02.06.2001
			399	45	254	15	285	10	314	14	403	40	06.09.2003
J1453+1025	383	15	359	07	293	04	194	04	160	03	116	13	23.07.2001
			353	07	321	03	230	03	198	03	184	14	06.08.2002
J1522+1041			320	14	205	10	112	06	85	17			08.06.2002
J1627+1216	348	30	294	13	275	07	259	11	252	07	220	20	15.11.2001
J1722+1013	360	30	384	12	385	07			567	07	730	48	02.06.2001
	360	25	378	18	374	07	370	06	369	12	351	34	04.11.2001
			339	30	340	06	374	06	395	07	435	32	12.09.2003
J1728+1215	257	22	394	16	537	04	716	09	849	14	960	22	16.10.2000
	250	19	403	07	524	06	613	07	737	10	793	20	23.07.2001
			316	24	429	06	517	10	578	20	571	45	08.06.2002
			210	29	350	15	470	13	565	14	584	40	12.09.2003
J2312+1224	700	25	370	15	265	11	152	05	115	07	67	09	04.11.2001

turnover frequency being near 0.7 GHz and the flux density at the turnover being $S_{\max} \approx 1600$ mJy. The extended component is plotted by the solid curve in Fig. 5b. The filled circles mark the spectrum obtained in July 2001.

In each of the four sets of observations, the spectrum of the compact component is best fit by the logarithmic parabola derived from the data averaged over the entire period of observations for this source. These spectra are plotted by the dashed and dash–dotted curves in Fig. 5b.

The spectrum of the compact component rises toward higher frequencies, with its maximum being above 40 GHz. This component is optically thick at the frequencies of our observations. The 21.7 GHz flux density reached a minimum in 2000, increased in 2001–2002, and then decreased again in 2003 to nearly its level in 2000.

These flux-density variations cannot be explained as the development of a single isolated outburst. In the standard model for the variability [13, 14], the flux density at a certain frequency should decrease only due to the transition to the optically thin part of the spectrum, which does not occur in this case. It may be that we are observing multiple outbursts whose evolution time scales are shorter than the duration of our observations. The observed evolution of the compact component is then the result of a kind of stroboscopic effect, due to our undersampling of the variations.

The flux density also varied within each set of observations. The largest variations were observed during the 97 nightly observations in 2002: the 11.1 GHz flux density increased from 1370 mJy at the beginning of this series to 1600 mJy at the end, while the 21.7 GHz flux density varied from 1400 to 1820 mJy. On June 30, 2002, the spectrum of the compact component was best fit by the parabola $\log S = 2.300 + 1.104\log\nu - 0.360\log^2\nu$, which has its maximum at $\nu_{\max} \approx 35$ GHz. Twenty days later, this spectrum was best fit by the parabola $\log S = 2.382 + 0.938\log\nu - 0.247\log^2\nu$, whose maximum is at 80 GHz. Such spectral behavior provides evidence that we are observing the evolution of two outbursts. The first was observed on June 30, 2000, while the second was observed 20 days later, at an earlier stage in its evolution. Both outbursts are well fit by logarithmic parabolas, which suggests that only one of the outbursts dominates at each these epochs. Thus, the first outburst evolved sufficiently over 20 days that its contribution to the spectrum had become negligible by the later epoch.

The object displays a high radio luminosity, close to the maximum observed for all the sources in the complete sample: $L_{\nu=11.1\ \mathrm{GHz}} = 13 \times 10^{34}$ erg/s Hz. This luminosity is calculated for a homogeneous isotropic cosmological model with zero cosmological constant, deceleration parameter $q = 0.5$, and $H = 65\ \mathrm{km\,s^{-1}\,Mpc^{-1}}$.

4.3. J0315+1012

We identified four weak emission lines with redshift $z = 0.222$ in the optical spectrum (Fig. 1c): [OII] 3727 Å, the [OIII] 4958, 5006 Å doublet, Hα 6563 Å, and [SII] 6717 Å. The object has been classified as an emission-line galaxy.

The spectrum is a power law, $S = 2055\,\nu^{-0.723}$ mJy, at 0.178–3.9 GHz. Above 3.9 GHz, the spectrum flattens due to the appearance of a compact component (Fig. 5c), however, we were not able to obtain a good two-component fit to the spectrum.

4.4. J0444+1042

Four emission lines are observed in the optical spectrum (Fig. 1d), which we identified as Lyα 1216 Å, CIV 1549 Å, and weak SiIV 1403 Å and CIII] 1909 Å at a redshift of $z = 2.403$. The object has been classified as a quasar. As for J0242+1101, the Lyα line is weaker than is typical for radio quasars, however, the line maximum may be distorted by noise.

The spectrum for November 2001 can be fit by the power law $S = 815\,\nu^{-0.372}$ mJy at 0.97–21.7 GHz (Fig. 5d). The spectrum is flat ($\alpha > -0.5$); no flux variability is observed.

4.5. J0448+1127

We identified CIII] 1909 Å and MgII 2798 Å in the optical spectrum (Fig. 1e). The full width at half maximum (FWHM) of both lines is ≈45 Å in the rest frame of the source. The redshift indicated by these lines is $z = 1.375$; the object is a quasar.

We obtained radio observations in 2001 and 2002. No flux-density variations were seen within the errors. The extended component is absent or too weak to be detected. The spectrum of the compact component averaged over the two sets of observations is best fit by the logarithmic parabola $\log S = 1.979 + 0.902\log\nu - 0.432\log^2\nu$, which has its maximum near 10 GHz and a peak flux density of 280 mJy (Fig. 5e). We were not able to measure the flux density at 7.7 GHz, because the angular distance to the adjacent strong source J0449+1121 and the distance between the feed horns of the system are very similar (the detecting equipment operates in a beam-modulation regime at this frequency). The approximate flux density at 7.7 GHz is 274 mJy.

4.6. J0449+1121

No lines are visible in the optical spectrum, and we accordingly classified this source as a BL Lac (Fig. 2a).

We obtained radio observations in 2000–2003. Figure 5f presents the spectra obtained (the spectrum for October 2000 is shown by the dash–dotted curve, for July 2001 by the dashed curve, and for July 2002 by the solid curve).

Note the strong long-term variability of the flux density (Table 3), which is accompanied by spectral variations. The spectral maximum was at 25 GHz in October 2000, but at frequencies above the observed interval at the other epochs.

The minimum flux density was observed in October 2000 at all frequencies; the maximum flux density at 7.7–21.7 GHz was observed in July 2002 and the maximum at 2.3 GHz in September 2003. The relative variability amplitudes are $V = 0.43$, 0.33, 0.29, 0.22, and 0.28 at 21.7, 11.1, 7.7, 3.9, and 2.3 GHz, respectively. These figures represent lower limits for the relative variability amplitudes, since the observations may be subject to a "stroboscopic effect" due to the presence of long gaps in the observations.

In addition to its long-term variability, the source displays strong variability on time scales shorter than a month. Analysis of the corresponding structure functions [15, 16] indicates that the characteristic time scale for variations increases with decreasing frequency.

The variability time scale is four days at 11.1 GHz, with the modulation index averaged over all epochs being $m = 3.5\%$. The characteristic time scale at 7.7 GHz is different at different epochs, and was four days ($m = 2.5\%$), five days ($m = 4.2\%$), and eight days ($m = 4.3\%$) in 2000, 2001, and 2002, respectively. The characteristic time scale was substantially longer at 3.9 GHz: 22 days ($m = 2.9$) in 2000, 10 days ($m = 4.8$) in 2001, and 16 days ($m = 5.0$) in 2002. Flux-density variations were detected at 2.3 GHz only in 2001, when they displayed a characteristic time scale of 14 days ($m = 5.0$); there are appreciable gaps in the measurements at each of the other epochs due to high levels of industrial and environmental noise.

We believe that this variability is due to scintillation in the interstellar medium; in this case, the frequency dependence of the characteristic time scale results from the frequency dependence for the angular size. The variations of the modulation index may be determined by variations in the degree of compactness of the source.

The influence of the adjacent source J0448+1127, which lies in one of the 7.7 GHz horns of the system, is significantly smaller, since its flux density is roughly a factor of five lower.

4.7. J0509+1011

The optical spectrum does not contain any lines, leading us to classify it as a BL Lac object (Fig. 2b).

Figure 5g presents the radio spectra obtained in October 2000 (solid curve) and November 2001 (dash–dotted curve) averaged over the total time spanned by the observations, together with the spectrum obtained at the end of a long series of observations in 2001, averaged over 10 days (dashed curve). The spectrum varied during June 5–September 10, 2001, and there is no single parabolic fit that is suitable for the entire averaged dataset.

Like J0449+1121, this source displays strong long-term variability of its flux density (Table 3). The shape of the spectrum also varies markedly. For example, in 2000, the spectrum could be fit well by a parabola with its maximum near 1 GHz, while the July 2001 spectrum has a minimum at 5 GHz, and the November 2001 spectrum a minimum below 1 GHz.

The flux-density variations are particularly large at 0.97, 2.3, and 3.9 GHz, where the relative amplitudes of the variability are $V = 0.27$ (October 2000, November 2001), 0.29 (October 2000, September 2003), and 0.22 (October 2000, November 2001). The dates in parentheses indicate the epochs of maximum and minimum flux density. Since no 0.97 GHz data are available after November 2001, the real relative variability amplitude at this frequency may be even higher.

It is likely that we are undersampling the variability, and that the real variability time scale does not exceed several months. This hypothesis is supported by the 21.7 GHz flux-density variations in 2001. The flux density was initially 512 ± 15 mJy, but had increased to 700 ± 20 mJy 98 days later.

The source also displays short-timescale variability. The structure functions derived from the 2000 and 2001 observations yield a characteristic time scale of three to four days. In 2000, the modulation index was $m = 4.3$, 7.4, and 10.0%, respectively, at 7.7, 3.9, and 2.3 GHz; no variability was detected at 7.7 GHz in 2001, while the modulation index was 4.5% at both 3.9 and 2.3 GHz.

4.8. J0516+1057

We were able to identify three weak emission lines with redshift $z = 1.580$ in the optical spectrum (Fig. 2c): CIV 1549 Å, HeII 1640 Å and CIII] 1909 Å. A line badly distorted by noise is visible at 7220 Å, which, at this redshift, can be identified with MgII 2798 Å. The object is classified as a quasar.

We obtained radio observations in 2001 and 2003; no significant flux-density variations were detected. The 0.97–21.7 GHz radio spectrum is best fit with the power law $S = 1270\,\nu^{-0.322}$ mJy (Fig. 5h).

4.9. J0749+1042

We identified three absorption lines in the optical spectrum (Fig. 2d): CaI 4227 Å, MgI 5175 Å, and Hα 6563 Å. The redshift derived from these lines is $z = 0.214$. The object is an absorption galaxy.

The source was observed in the radio in June 2001 and November 2001. Its flux density did not vary during this interval.

We were able to fit an extended component with a power-law spectrum starting from 0.365 GHz in the combined spectrum (Fig. 5i, filled circles): $S = 167\,\nu^{-0.92}$ mJy (solid curve). The spectrum of the compact component is best fit by the parabola $\log S = 1.761 + 0.940\log\nu - 0.532\log^2\nu$, which has its maximum flux density (150 mJy) at 7.6 GHz (dashed curve). The extended component contributes 75% of the total flux density at 0.97 GHz.

4.10. J0758+1136

Two objects are blended in the optical spectrum. After separating their spectra, one appears to be a star. Figure 2e presents the other spectrum, in which we have identified strong MgII 2798 Å, Hδ 4102 Å, and Hγ 4340 Å at a redshift of $z = 0.569$. The oxygen absorption line at ≈7650 Å is probably partially canceled out by an emission line, which may be Hβ 4861 Å, given the redshift of the object. The MgII line FWHM is ≈40 Å in the rest frame of the source. We classified this object as a quasar.

The source was observed in the radio in September 2000, June 2001, and November 2001. During this interval, the flux density remained constant within the errors. The radio spectrum falls off with frequency, flattening toward high frequencies (Fig. 5j). The spectrum (filled circles) can be divided into a power-law extended component, $S = 440\,\nu^{-0.80}$ mJy (solid curve in Fig. 5j), and a compact component, $\log S = 2.019 + 0.646\log\nu - 0.312\log^2\nu$, which has its maximum flux density (225 mJy) at 10 GHz (dashed curve).

4.11. J0914+1006

We have identified three lines in the optical spectrum with [OII] 3727 Å, [OIII] 5007 Å, and Hα 6563 Å (Fig. 3a). The object is classified as an emission-line galaxy with a redshift of $z = 0.311$.

The source is resolved in right-ascension by the RATAN-600 beam at frequencies above 3 GHz, and flux densities were obtained only at 0.97 and 2.3 GHz (Table 3). According to our measured flux densities and published data for the flux densities at 0.365, 1.4, and 4.85 GHz, the spectrum is described by the power law $S = 420\,\nu^{-0.525}$ mJy in the interval 0.365–4.85 GHz.

4.12. J1327+1223

Seven emission lines were identified in the optical spectrum (Fig. 3b): [NeIV] 2424 Å, MgII 2798 Å, [NeV] 3346 Å and [NeV] 3426 Å, [OII] 3727 Å, weak [OIII] 4958 Å, strong [OIII] 5007 Å, and MgI 5175 Å. The object is a quasar with redshift $z = 0.950$.

We obtained radio observations in 2001 and 2003. The source displays flux-density variability and a complex spectrum. Figure 6a presents the spectrum for 2001 (filled circles). An extended component with a power-law spectrum, $S = 510\,\nu^{-0.70}$ mJy, has been fit. The extended component contributes 90% of the total flux density at 0.97 GHz. At epoch June 2, 2001, the spectrum of the compact component can be described by the parabola $\log S = 1.835 + 1.075\log\nu - 0.409\log^2\nu$, which has its maximum flux density (350 mJy) at 20 GHz (Fig. 6a, dashed curve). At epoch September 6, 2003, the spectrum of the compact component can be approximated by part of a parabola that rises toward high frequencies, with the peak being located above the studied frequency interval. It is likely that the initial phase of a new outburst was observed in 2003.

4.13. J1453+1025

Three weak lines with a redshift of $z = 1.773$ were identified in the optical spectrum (Fig. 3c): CIV 1549 Å, CIII] 1909 Å, and MgII 2798 Å. The object is classified as a quasar.

We obtained radio observations in 2001 and 2002. Figure 6b presents the radio spectra for July 2001 and August 2002. Taking into account the data at 0.365 GHz, both the spectra are consistent with a two-component model: one component had its maximum at 1 GHz and remained essentially constant over the year, while the other was variable, and can be fit with parabolas with maxima near 25 GHz in July 2001 and well above the studied interval in July 2002.

4.14. J1522+0400

Both emission and absorption lines are visible in the optical spectrum (Fig. 3d). We have identified the emission lines as [OII] 3727 Å, the [OII] 4958 Å, 5007 Å doublet, Hα 6563 Å, and [SII] 6724 Å. These lines yield a redshift of $z = 0.204$. Based on this redshift, three weak absorption lines can be identified with Hβ 4861 Å, MgI 5175 Å, and NaI 5893 Å. The object is an emission-line galaxy.

The source's radio flux density is constant. Its spectrum can be described by the power law $S = 640\,\nu^{-0.832}$ mJy at 0.365–11.1 GHz (Fig. 6c).

4.15. J1627+1216

Four emission lines were identified in the optical spectrum (Fig. 3e): CIII] 1909 Å, MgII 2798 Å, [NeV] 3426 Å, and [OII] 3727 Å lines. These lines indicate a redshift of $z = 1.216$. The object is a quasar.

We obtained radio observations on June 2001 and November 2001; the flux density remained essentially constant at all frequencies during this time. The 0.97–21.7 GHz radio spectrum can be approximated with the power law $S = 333\,\nu^{-0.125}$ mJy (Fig. 6d), but the presence of large discrepancies with the fit indicates that the spectrum is complex. We were unable to separate the spectrum into components.

4.16. J1722+1013

A strong line with a width of about 50 Å is observed in the optical spectrum (Fig. 4a), which we identified with MgII 2798 Å at a redshift of $z = 0.732$; [NeV] 3426 Å with the same redshift is also detected. A weak line is visible at 8670 Å, which corresponds to [OIII] 5007 Å at the given redshift. The object is classified as a quasar.

We obtained radio observations at three epochs in 2001 and 2003. The spectrum was flat in November 2001 (Fig. 6e, dashed curve), and increased toward high frequencies at the other epochs (Fig. 6e, June 2003; the spectrum is plotted by the solid curve). A decrease in the flux density at 21.7 GHz over five months was detected—from 730 ± 48 Jy in June 2001 to 351 ± 34 Jy in November 2001. The relative amplitude of the variability is $V = 0.35$.

4.17. J1728+1215

Three strong lines are observed in the optical spectrum (Fig. 4b), which we identified with MgII 2798 Å, Hβ 4861 Å, and the [OIII] 4958, 5007 Å doublet at a redshift of $z = 0.589$. The object is a quasar.

We obtained four sets of radio observations in 2000–2003. The structure functions indicate substantial variability of the flux density on a time scale of 12 days at 3.9, 7.7, and 11.1 GHz. Figure 6f presents the spectra for October 2000 and September 2003. In the first spectrum (solid curve), the maximum lies substantially above the studied interval ($\nu_{\max} \approx$ 110 GHz); in the second (dashed curve), the maximum is at $\nu_{\max} \approx 20$ GHz. The spectra obtained in 2001 and 2002 are between these two. It appears that we observed the development of a single outburst, with the flux-density maximum being shifted toward low frequencies with time.

4.18. J2312+1224

Two weak emission lines are observed in the optical spectrum (Fig. 4c), which we identified with CIII] 1909 Å and MgII 2798 Å at a redshift of $z = 1.285$. The object is a quasar.

The source displays a power-law spectrum, $S = 695\,\nu^{-0.745}$ mJy, and constant flux densities at 0.97–21.7 GHz (Fig. 6g). The spectrum can be described with the same power-law index in the broader interval 0.178–21.7 GHz.

4.19. J2315+1027

The strongest lines in the optical spectrum (Fig. 4d) can be identified with the [OIII] 4958, 5007 Å doublet and Hα 6563 Å. In addition, [OII] 3727 Å, [SII] 6717 Å, and weak Hβ 4861 Å are visible. The redshift derived from all these lines is $z = 0.255$. The object is classified as an emission-line galaxy.

Since the radio source is known to be double and is not resolved by the RATAN-600, we were not able to obtain its radio parameters.

5. CONCLUSION

We have classified the twelve radio sources J0143+1215 ($z = 1.18$), J0242+1101 ($z = 2.694$), J0444+1042 ($z = 2.403$), J0448+1127 ($z = 1.375$), J0516+1057 ($z = 1.580$), J0758+1136 ($z = 0.569$), J1327+1223 ($z = 0.950$), J1453+1025 ($z = 1.773$), J1627+1216 ($z = 1.216$), J1722+1013 ($z = 0.732$), J1728+1215 ($z = 0.589$), and J2312+1224 ($z = 1.285$) as quasars. Their optical spectra display the standard set of lines typical for quasars at the given redshifts: Lyα 1216 Å, CIV 1549 Å, CIII] 1909 Å, and MgII 2798 Å. Weaker lines are also visible in several of the spectra: SiIV 1403 Å, [NeV] 3346, 3426 Å, Hβ 4861 Å and the [OIII] 4958, 5007 Å doublet.

We observed power-law spectra ($S \propto \nu^{\alpha}$) in only these twelve quasars; two of them—J0444+1042 and J0516+1057—display flat spectra, with $\alpha = -0.372$ and $\alpha = -0.322$, respectively. The source J2312+1224 displays a steep spectrum with $\alpha = -0.745$. The flux densities of these quasars did not vary over the course of our observations.

The spectra of the other nine quasars cannot be approximated by power laws. Five of these objects display long-term variability of their flux density, while the flux densities of four objects remained constant during the interval spanned by our observations.

We were able to obtain two-component fits with an extended component, $\log S = S_o + \alpha \log \nu$, and a compact component, $\log S = S_o + B \log \nu +$

$C \log^2 \nu$, for the spectra of the four quasars J0143+1215, J0242+1101, J0758+1136, and J1327+1223.

No lines are visible in the spectra of J0449+1121 and J0509+1011, leading us to classify them as BL Lac objects. Both display substantial long-term variability with relative variability amplitudes $V = 0.2–0.4$. In addition, both sources display appreciable variability on shorter time scales of 3–4 days for J0509+1011 and 4–20 days for J0449+1121. In the latter source, the variability time scale depends on the frequency and observing epoch.

The four objects J0315+1012 ($z = 0.222$), J0914+1006 ($z = 0.311$), J1522+1041 ($z = 0.204$), and J2315+1027 ($z = 0.255$) are emission-line galaxies. The [OII] 3727 Å, [OIII] 4958, 5007 Å, and Hα 4861 Å lines typical of emission-line galaxies are visible in all their spectra. In J1522+1041, three absorption lines with the same redshift are also seen. The radio spectra of three of these objects are power laws; the spectrum of J0315+1012 is also a power law at 0.178–3.9 GHz, but flattens at lower frequencies, possibly reflecting the presence of weak compact components.

The source J0749+1057 was identified with an absorption-line galaxy at a redshift of $z = 0.214$. The spectrum can be separated into an extended and compact component, with the radiation of the compact component dominating at 2.3–21.7 GHz. We have identified a number of other radio sources with absorption-line galaxies earlier; for example, J1306+1113 [5] and J2330+1218 [4].

ACKNOWLEDGMENTS

This work was supported by the Federal Science and Technology Program "Astronomy," the Russian Foundation for Basic Research (project no. 02-07-90247), and the Federal Science and Technology Project "Universities of Russia" (project no. UR 02.03.029).

REFERENCES

1. P. C. Gregory, W. K. Scott, K. Douglas, and J. J. Condon, Astrophys. J., Suppl. Ser. **103**, 427 (1996).
2. A. G. Gorshkov, V. K. Konnikova, and M. G. Mingaliev, Astron. Zh. **80**, 978 (2003) [Astron. Rep. **47**, 903 (2003)].
3. M. P. Veron-Cetty and P. Veron, Astron. Astrophys. **374**, 92 (2001).
4. V. Chavushyan, R. Mujica, J. R. Valdez, *et al.*, Astron. Zh. **79**, 771 (2002) [Astron. Rep. **46**, 697 (2002)].
5. V. L. Afanas'ev, S. N. Dodonov, A. V. Moiseev, *et al.*, Pis'ma Astron. Zh. **29**, 626 (2003) [Astron. Lett. **29**, 579 (2003)].
6. http://www.sao.ru/moisav/scorpio/scorpio.html.
7. A. M. Botashev, A. G. Gorshkov, V. K. Konnikova, and M. G. Mingaliev, Astron. Zh. **76**, 723 (1999) [Astron. Rep. **43**, 631 (1999)].
8. A. G. Gorshkov and O. I. Khromov, Astrofiz. Issled., Izv. Spets. Astrofiz. Obs. **14**, 15 (1981).
9. I. W. A. Browne, Mon. Not. R. Astron. Soc. **293**, 257 (1998).
10. J. J. Condon, W. D. Cotton, E. W. Greisen, *et al.*, Astron. J. **115**, 1693 (1998).
11. J. N. Douglas, Astron. J. **111**, 1945 (1996).
12. D. Monet, A. Bird, B. Canzian, *et al.*, USNO-SA1.0 (US Naval Observatory, Washington DC, 1996).
13. A. P. Marscher and W. K. Gear, Astrophys. J. **298**, 114 (1985).
14. E. Valtaoja, H. Terasranta, S. Urpo, *et al.*, Astron. Astrophys. **254**, 71 (1992).
15. J. H. Simmonetti, J. M. Cordes, and D. S. Heeschen, Astrophys. J. **296**, 46 (1985).
16. P. A. Hughes, H. D. Aller, and V. F. Aller, Astrophys. J. **396**, 469 (1992).

Translated by K. Maslennikov

Astronomy Reports, Vol. 49, No. 5, 2005, pp. 390–404. Translated from Astronomicheskiĭ Zhurnal, Vol. 82, No. 5, 2005, pp. 437–452.

The Chemical Composition of Galactic Planetary Nebulae with Regard to Inhomogeneity in the Gas Density in Their Envelopes

V. V. Holovatyy and N. V. Havrilova

Chair of Astrophysics, Franko State University, ul. Kyryla i Mefodija 8, Lviv, 79005 Ukraine

Received December 23, 2003; in final form, December 3, 2004

Abstract—The results of a study of the chemical compositions of Galactic planetary nebulae taking into account two types of inhomogeneity in the nebular gas density in their envelopes are reported. New analytical expressions for the ionization correction factors have been derived and are used to determine the chemical compositions of the nebular gas in Galactic planetary nebulae. The abundances of He, N, O, Ne, S, and Ar have been found for 193 objects. The $Y-Z$ diagrams for various He abundances are analyzed for type II planetary nebulae separately and jointly with HII regions. The primordial helium abundance Y_p and enrichment ratio dY/dZ are determined, and the resulting values are compared with the data of other authors. Radial abundance gradients in the Galactic disk are studied using type II planetary nebulae.

1. INTRODUCTION

Planetary nebulae (PN) are convenient objects for studies of the chemical evolution of matter in the Galaxy. Owing to their relatively simple structure, their chemical compositions can be determined more accurately than those of other stellar objects. Comparisons of the metallicities of PN and of HII regions in blue compact dwarf galaxies can yield more complete information about the pre-Galactic helium abundance, rate of enrichment of matter in the Universe in heavy elements, and possible changes in this rate during the chemical evolution of galaxies. This makes accurate determinations of the chemical compositions of PN very important.

The difficulty in determining the chemical compositions of PN is that not all emission lines and not all ions are observed in the spectra of these nebulae. Usually, so-called ionization correction factors (ICFs), based on the similarities of the ionization potentials, are used when deriving the chemical compositions of PN. However, these do not include differences in the effective photoionization cross sections and excitation conditions of various ions. Obviously, a more accurate method for determining the ICFs would be to find them via calculations of a grid of photoionization models (PIMs) for the PN emission [1, 2]. Note that the accuracy with which such ICFs can be determined depends on the accuracy of the atomic data used, as well as the structure of the gas density in the PN. Images of many PN demonstrate nonuniform patterns in their gas envelopes [3]; the best known example is probably the Helix Nebula [4]. The origin of this nonuniformity is not well understood. Two types of models and theories have been devised: those in which the inhomogeneity forms before the PN itself [5], and those in which it forms later, during the evolution of the PN [6]. On rare occasions, the sizes and number of inhomogeneities in a specific PN can be determined [7, 8]. Peimbert [9] noted early on that the differences in the derived electron temperatures T_e for PN were greater than the likely errors in the calculations, implying the presence of large fluctuations in T_e, which could be due to spatial fluctuations of the gas density in the PN envelopes. When calculating PN PIMs, authors frequently assume a constant density for the nebular gas and spherical symmetry for the envelopes, or the presence of n-type macrofluctuations [8]. Rubin [10] and Kingdon and Ferland [11] introduced inhomogeneity in the form of a sinusoidal distribution for the gas density.

Some three-dimensional models for individual nebulae have recently been published [12, 13]. However, these calculations are rather cumbersome, and the homogeneous sample of objects considered is small. At the same time, such samples enable us to analyze the $Y-Z$ dependences (where Y and Z are the mass abundances of helium and of heavy elements) and to elucidate which estimate of the pre-Galactic helium abundance is more trustworthy: $Y_p = 0.234 \pm 0.002$ [14] or $Y_p = 0.244 \pm 0.002$ [15]. Data for PN samples can also be used to study elemental-abundance gradients in the Galactic disk. These gradients depend strongly on the distance scale adopted [16], leading to appreciable scatter in the gradients obtained by different authors.

1063-7729/05/4905-0390$26.00

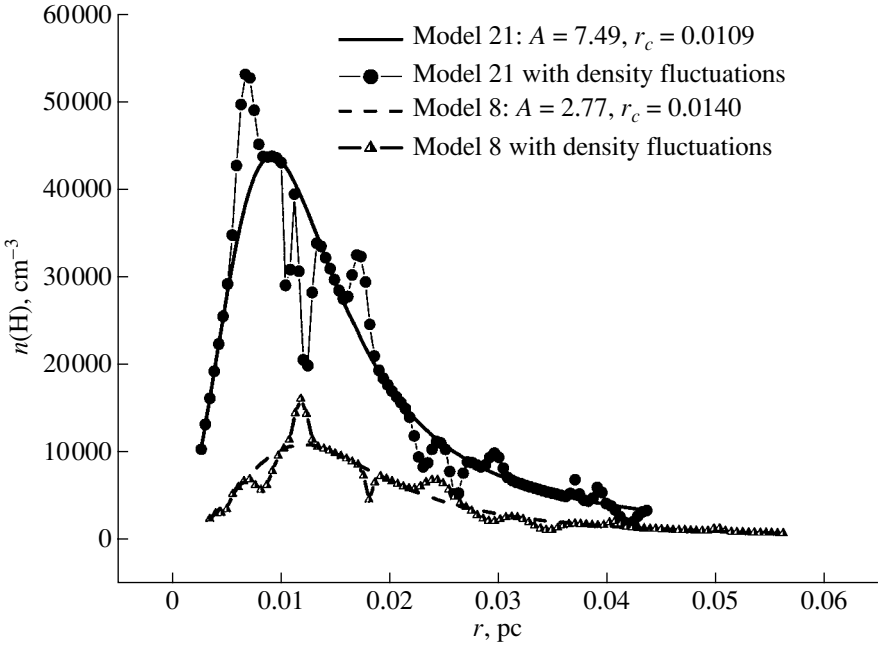

Fig. 1. Radial distribution of the gas density in the envelopes of two model planetary nebulae.

We report here new determinations of the chemical compositions of a sample of 193 galactic PN, adopting a radial distribution for the gas density that is close to the observed distribution [17]. All supplementary data are available on the ftp server of the Astronomical Observatory of the Lviv Franko State University: ftp://astro.franko.lviv.ua/PN/ChemCompPN2004.

2. PLANETARY NEBULA PIM CALCULATIONS

We used the CLOUDY94 code of Ferland [18] to calculate photoionization models for the emission of the planetary nebulae. We calculated two grids of models, each containing 270 PN PIMs. The free parameters for each grid of models were the spectral energy distribution (SED) of the PN nucleus at $\lambda \leq$ 912 Å and the filling factor and chemical composition of the nebular gas. We took the effective temperatures T_* and radii r_* of the central stars of the PN required for the models from the evolutionary tracks of Bloecker [19, 20]. The SEDs of the nuclei at $\lambda \leq$ 912 Å corresponded to the model stellar atmospheres of Clegg and Middlemass [21], which include the effect of the stellar wind [22]. All the PIMs were spherically symmetric.

To allow for various types of gas-density inhomogeneity in the PN envelopes, we used a distribution close to the observed distribution as a first approximation. The radial distribution of the gas density in the PN envelopes (type I inhomogeneity) was specified by the following empirical relationship derived from isophotal maps of actual PN [17]:

$$n(r) = \frac{x^2\left(1+3e^{-1.2x}\right)}{\left(x^2-1\right)^2+0.36r_c^{-0.43}x^2}\frac{A}{r_c^2} \quad \mathrm{cm}^{-3}, \quad (1)$$

where $x = r/r_c$ and $r_c = \langle V_{\mathrm{exp}}\rangle\, t$. Here, r is the distance from the central star to a given point in the nebula, n is the gas density at this point, $\langle V_{\mathrm{exp}}\rangle$ is the average expansion velocity of the envelope, and t is the age of the envelope. The parameter A describes the outflow of stellar material during the detachment of the nebular envelope [23]. For most PN, the values of A lie in the interval 0.8–8.0, which corresponds to mass-loss rates of $(0.5\text{–}5.6) \times 10^{-5}\ M_\odot$/year at a velocity $\langle V_{\mathrm{exp}}\rangle$ of about 15 km/s. For most of the PN studied, A is close to 1.6. The inhomogeneity of the nebular gas for the grid models was also taken into account by varying the filling factor [24], which we assigned values of 0.1, 0.5, and 1.

The next step was taking into account fluctuations of the gas density in the PN envelopes (type II inhomogeneity). We wrote code that superimposed inhomogeneities on the distribution (1) using a standard random-number generator (a modified version of the code of [25]). The input parameters were:

(1) the parameters of the PN envelope: r_c and A [see (1)], and the inner and outer radii of the envelope r_{in} and r_{out} ($r_{\mathrm{in}} = r_c/3$, $r_{\mathrm{out}} = 3 \times r_c$);

(2) the parameters of the inhomogeneities: n_{min} and n_{max} are the minimum and maximum numbers of

Table 1. Empirical relationships for the chemical composition of nebular gas; $\left(\frac{(A/H)_{calc}}{(A/H)_{mod}}\right)$ for planetary nebulae

No.	References	Relationship	$\frac{(A/H)_{calc}}{(A/H)_{mod}}$
1	1, 2	$He/H = [He^{+} + He^{++}]/H^{+}$	0.200
2	3, 4, 5, 6	$He/H = (He^{+}/H^{+})[1 - 0.25\,(O^{+}/O)]^{-1}$	0.229
3	7	$C/H = (C^{+} + C^{++} + C^{3+})/H^{+}$	0.209
4	8	$C/H = [(He^{+} + He^{++})/He^{+}]^{1/3}(C^{+} + C^{++} + C^{3+})$	0.218
5	9	$N/O = N^{+}/O^{+}$	0.339
6	4, 2	$N/H = (O/O^{+})(N^{+}/H^{+})$	0.248
7	4	$O/H = [(He^{++} + He^{+})/He^{+}][(O^{+} + O^{++})/H^{+}]$	0.748
8	10	$O/H = (O^{+} + O^{++})/H^{+}$	0.689
9	8	$O/H = [1/[1 - 0.95N^{4+}/(N^{+} + N^{++} + N^{3+} + N^{4+})]](O^{+} + O^{++} + O^{3+})/H^{+}$	0.689
10	8	$O/H = [(He^{+} + He^{++})/He^{+}]^{2/3}(O^{+} + O^{++})/H^{+}$	0.727
11	3, 5, 6	$Ne/H = (Ne^{++} + Ne^{3+})/H^{+}$	0.468
12	2	$S/H = (O/O^{+})(S^{+} + S^{++})/H^{+}$	2.47
13	11	$S/H = [S/(S^{+} + S^{++})](S^{+3}/H^{+}) = [0.013 + x(5.10 + x[-12.78 + x(14.77 - 6.11x)])]^{-1}(S^{+3}/H^{+})$, where $x = O^{+}/O$	1.55
14	10	$Ar/H = [(Ar^{++} + Ar^{3+})/H^{+}][(He^{+} + He^{++})/He^{+}]$	0.963
15	3, 5, 6	$Ar/H = (Ar^{2+} + Ar^{3+} + Ar^{4+})/H^{+}$	0.884
16	9, 2	$Ar/H = 1.87(Ar^{++}/H^{+})$	1.49

Literature to Table 1:
1. *M. Seaton*, Mon. Not. Roy. Astron. Soc. **139**, 129 (1968).
2. *P. Leisy, M. Donnefeld,* Astron. Astrophys., Suppl. Ser. **116**, 95 (1996).
3. *G. Stasińska,* Astron. Astrophys. **66**, 257 (1978).
4. *J. Lequeux et al.*, Astron. Astrophys. **90**, 155 (1979).
5. *G. Stasińska,* Astron. Astrophys. **84**, 320 (1980).
6. *G. Stasińska,* Astron. Astrophys., Suppl. Ser. **48**, 299 (1982).
7. *B. Wilkes et al.*, Mon. Not. Roy. Astron. Soc. **197**, 1 (1981).
8. *R. L. Kinsburgh, M. J. Barlow,* Mon. Not. Roy. Astron. Soc. **271**, 257 (1994).
9. *M. Peimbert et al.*, Rev. Mex. Astron. y Astrofís. **31**, 147 (1995).
10. *T. Barker,* Astrophys. J. **267**, 630 (1983).
11. *T. X. Thuan et al.*, Astrophys. J. **445**, 108 (1995).

fluctuations (5–15), d_{min} and d_{max} are the minimum and maximum sizes of the fluctuations in percent relative to the envelope radius $r = r_{out} - r_{in}$ (0.5–5%), ρ_{min} and ρ_{max} are the minimum and maximum deviations of the density of an inhomogeneity from the main distribution (1) (5–30%), and the magnitudes of the fluctuations themselves (to 20%). The parameters of the inhomogeneities were matched to the observational data.

The gas-density fluctuations had the form of a spherical belt, and were superimposed on the overall gas distribution in such a way that the total mass of the model nebula envelope was conserved. The result of the computations is a file with the radial gas-density distribution of the nebula envelope.

Figure 1 shows the radial gas-density distributions for two PIMs with different values for r_c and A (without and with gas-density fluctuations). In the computations, r_c was varied from 1.23×10^{-2} to 7.30×10^{-2} pc.

The parameters for each of 30 selected basic models for the calculations of our two PN PIM grids are available on our ftp server (Modparameters.tar.gz).

In all, we computed 540 PN PIMs. The integrated spectra of these models were taken to be those observed, and were analyzed using the well known methods of nebular gas diagnostics. This yielded

Table 2. ICFs for type I (F) and type II (FF) inhomogeneity in the gas density distribution

No.	A^{+i}/H^+	X^{+k+1}/X^{+k}	Polynomial coefficients				r	$(A/H)_{calc}/(A/H)_{mod}$
			C_0	C_1	C_2	C_3		
He/H : $1, 2(x \in [-3.012..-0.173])$								
F1	He^+	He^{2+}/He^+	−0.23870	−0.60140	−0.33475	−0.05832	0.91	1.011
F2	He^{2+}	He^{2+}/He^+	−0.23870	0.39860	−0.33475	−0.05832	0.99	1.011
O/H : $3(x \in [-0.848..1.445]); 4(x \in [-0.601..1.111]); 5(x \in [-1.538..-0.278])$								
F3	O^+	O^{2+}/O^+	−0.27601	−0.61017	−0.45654	0.04707	0.91	1.033
F4	O^{2+}	S^{2+}/S^+	−0.37506	0.76762	−0.80102		0.65	1.008
F5	O^+	Ar^{3+}/Ar^{2+}	−1.36930	−2.26755	−1.44714	−0.32455	0.84	1.041
N/H : $6(x \in [-0.842..1.445]); 7(x \in [-0.589..1.093]); 8(x \in [-2.069..0.121])$								
F6	N^+	O^{2+}/O^+	−0.27782	−0.62239	−0.34683		0.96	1.149
F7	N^+	S^{2+}/S^+	−0.16105	−0.71193	−1.04641	0.30716	0.88	1.189
F8	N^+	Ar^{3+}/Ar^{2+}	−1.30959	−2.17432	−1.43771	−0.34048	0.84	0.870
Ne/H : $9(x \in [-0.708..1.502]); 10(x \in [-2.042..0.101])$								
F9	Ne^{2+}	O^{2+}/O^+	−0.06150	−0.08428	−0.21927	0.06389	0.43	1.024
F10	Ne^{2+}	Ar^{3+}/Ar^{2+}	−0.32702	−0.51322	−0.22932	−0.00919	0.49	1.016
S/H : $11(x \in [-0.821..1.467]); 12(\in [-0.842..1.424]);$ $13(\in [-0.598..1.093]); 14(x \in [-2.077..0.121])$								
F11	S^+	O^{2+}/O^+	−0.33362	−0.62060	−0.26100	−0.07336	0.94	1.021
F12	S^{2+}	O^{2+}/O^+	−0.17925	−0.03041	−0.36595	0.03666	0.78	1.007
F13	S^+	S^{2+}/S^+	−0.20142	−0.86441	−0.72479	0.11284	0.94	1.015
F14	S^+	Ar^{3+}/Ar^{2+}	−1.37852	−2.40162	−1.76205	−0.45096	0.79	1.093
Ar/H : $15(x \in [-0.821..-1.424]); 16(x \in [-0.864..1.445]); 17, 18(x \in [-2.060..0.122])$								
F15	Ar^{2+}	O^{2+}/O^+	−0.07643	−0.22497	−0.23215	0.03283	0.76	1.017
F16	Ar^{3+}	O^{2+}/O^+	−0.98922	1.05332	−0.59124	−0.03053	0.88	1.050
F17	Ar^{2+}	Ar^{3+}/Ar^{2+}	−0.55070	−1.00470	−0.63547	−0.13461	0.78	1.015
F18	Ar^{3+}	Ar^{3+}/Ar^{2+}	−0.55070	−0.00471	−0.63547	−0.13461	0.95	1.015
He/H : $1(x \in [-3.696..0.178]); 2(x \in [-3.523..-0.050])$								
FF1	He^+	He^{2+}/He^+	−0.22559	−0.53991	−0.26862	−0.04109	0.74	1.011
FF2	He^{2+}	He^{2+}/He^+	−0.13271	0.77099	−0.04971		0.99	1.016
O/H : $3(x \in [-0.236..1.098]); 6(x \in [-2.081..-0.177]);$ $4(x \in [-0.843..1.315]); 5(x \in [-0.351..0.7263])$								
FF3	O^+	O^{2+}/O^+	−0.28347	−0.60137	−0.41236		0.89	1.033
FF4	O^{2+}	O^{2+}/O^+	−0.29168	0.46012	−0.39720	−0.07055	0.94	1.046
FF5	O^{2+}	S^{2+}/S^+	−0.38583	0.78229	−0.68946	−0.13053	0.67	1.027
FF6	O^+	Ar^{3+}/Ar^{2+}	−1.35031	−2.19380	−1.37347	−0.30467	0.84	1.051

Table 2. (Contd.)

No.	A^{+i}/H^+	X^{+k+1}/X^{+k}	Polynomial coefficients				r	$(A/H)_{calc}/(A/H)_{mod}$
			C_0	C_1	C_2	C_3		
N/H : $7(x \in [-0.794..1.414]); 8(x \in [-0.360..0.668]); 9(x \in [-2.081..-0.052])$								
FF7	N^+	O^{2+}/O^+	−0.27858	−0.62863	−0.34379		0.96	1.314
FF8	N^+	S^{2+}/S^+	−0.18648	−0.68632	−0.76086		0.87	1.326
FF9	N^+	Ar^{3+}/Ar^{2+}	−1.28947	−2.09108	−1.34620	−0.31297	0.84	1.325
Ne/H : $10(x \in [-2.0819..-0.187])$								
FF10	Ne^{2+}	Ar^{3+}/Ar^{2+}	−0.32575	−0.49150	−0.19930		0.84	1.025
S/H : $11(x \in [-0.769..1.340]); 12(x \in [-0.601..1.340]);$ $13(\in [-0.351..1.098]); 14(x \in [-2.050..-0.021]); 15(x \in [-1.155..-0.082])$								
FF11	S^+	O^{2+}/O^+	−0.32238	−0.65139	−0.32790		0.93	1.031
FF12	S^{2+}	O^{2+}/O^+	−0.18345	−0.03747	−0.31307	−0.00846	0.76	1.014
FF13	S^+	S^{2+}/S^+	−0.19761	−0.85607	−0.76149	0.12733	0.95	1.012
FF14	S^+	Ar^{3+}/Ar^{2+}	−1.36016	−2.31242	−1.65119	−0.41463	0.79	1.095
FF15	S^{2+}	Ar^{3+}/Ar^{2+}	−0.58767	−1.06149	−0.83329	−0.19345	0.79	1.003
Ar/H : $16(x \in [-0.794..1.196]); 18(x \in [-2.081..0.062]);$ $17(x \in [-0.754..0.621]); 19(x \in [-2.092..-0.167])$								
FF16	Ar^{2+}	O^{2+}/O^+	−0.08066	−0.22004	−0.20368		0.74	1.020
FF17	Ar^{3+}	O^{2+}/O^+	−0.98865	1.05557	−0.57037	−0.06337	0.88	1.049
FF18	Ar^{2+}	Ar^{3+}/Ar^{2+}	−0.55086	−1.00056	−0.62990	−0.13395	0.78	1.012
FF19	Ar^{3+}	Ar^{3+}/Ar^{2+}	−0.55086	−5.68722	−0.62990	−0.13395	0.96	1.018

values for T_e, n_e, and the relative ion abundances $(A^{+i}/H^+)_{diagn}$. The observed emission-line spectra of actual PN are analyzed precisely in this manner. We used the DIAGN software [26] with the same atomic data used in the CLOUDY94 software to find $(A^{+i}/H^+)_{diagn}$. For most ions, the values of $(A^{+i}/H^+)_{diagn}$ differ from the $(A^{+i}/H^+)_{mod}$ values computed in the PIMs [27]. We expect that the values of $(A^{+i}/H^+)_{diagn}$ are more accurate, since they are derived from observations in just this way.

The resulting values of T_e, n_e, and A^{+i}/H^+ for all the models (for type I and type II inhomogeneity) are available on our ftp server (PNGrid.tar.gz, PNGridfluct.tar.gz). More detailed calculations are also given in our paper [27].

3. TESTING THE EMPIRICAL RELATIONSHIPS FOR THE ICFs

We selected 67 empirical relationships used to determine the chemical compositions of PN from the literature. These are located on our ftp server (PN_ICF.ps).

It is of interest to use the available ICFs to try to reproduce the chemical compositions $(A/H)_{mod}$ adopted in the PIMs. We used the integrated PIM spectra computed as described above for this purpose. The test procedure was the following. We first determined the relative ion abundances $(A^{+i}/H^+)_{diagn}$ based on diagnostics of these spectra, which we further used to determine computed values of $(A/H)_{calc}$ from each of the relationships. We then compared the corresponding values of $(A/H)_{mod}$ and $(A/H)_{calc}$. Obviously, the closer the ratio $(A/H)_{calc}/(A/H)_{mod}$ is to unity, the more accurate the expression for the ICFs.

The results for 35 empirical relationships that could be tested in this way are located on our ftp server (PNICFtest.ps).

Table 1 lists 16 of the 67 empirical relationships we collected from the literature, together with the test results for each of these relationships. The values

of $(A/H)_{calc}/(A/H)_{mod}$ were obtained by averaging the results of the computed PN PIMs. We can see from the testing results that only some of the relationships display deviations of the above ratio from unity $\leq 30\%$ (i.e., $(A/H)_{calc}/(A/H)_{mod}$ lies within the interval 0.7–1.3). This indicates the need for new ICFs for use in the determination of the chemical abundances in PN.

4. NEW ICFs AND OUR DETERMINATION OF THE CHEMICAL COMPOSITIONS OF GALACTIC PN

We considered relationships linking the ion abundances A^{+i}/H^+ and the total abundance A/H as follows [27]:

$$\log[(A^{+i}/H^+)/(A/H)] = f(x), \qquad (2)$$
$$x = \log(X^{+k+1}/X^{+k}).$$

These relationships were approximated by a polynomial function:

$$f(x) = \sum_{n=0}^{3} C_n * x^n, \qquad (3)$$

where C_n are the polynomial coefficients.

We found new ICFs for the two types of inhomogeneity. We used 18 new expressions for type I inhomogeneity (F1–F18, Table 2), and 19 new expressions for type II inhomogeneity (FF1–FF19, Table 2). The columns of Table 2 present (1) a number identifying the ICF relationship, (2) the abundance of the ith ionization stage A^{+i}/H^+ of element A, (3) the ion abundances for elements in adjacent ionization stages X^{+k+1}/X^{+k}, (4)–(7) the polynomial coefficients C_0, C_1, C_2, and C_3, (8) the correlation coefficient r for each relationship, and (9) the results of our testing of the relationships, $(A/H)_{calc}/(A/H)_{mod}$.

Analysis of the formulas for the helium abundance indicated that they are not entirely exact. Figure 2 shows $(He/H)_{calc}/(He/H)_{mod}$ as a function of $(He^+/H^+)_{mod}$, obtained from the calculated PN PIM grid [27] for the F1 ICF (Table 1). The results of previous calculations demonstrate that the values of He^+/H^+ for most Galactic PN lie in the interval 0.081–0.125 [28]. We observe a wide scatter in $(A/H)_{calc}/(A/H)_{mod}$ precisely in this range of He^+/H^+ values. Therefore, we adopted ICF(He) = 1 when determining the helium abundance; i.e., $He/H = He^+/H^+ + He^{++}/H^+$.

In total, we derived the chemical compositions of 193 Galactic PN. A bibliography of the observational data used is located on our ftp server (PNList.txt).

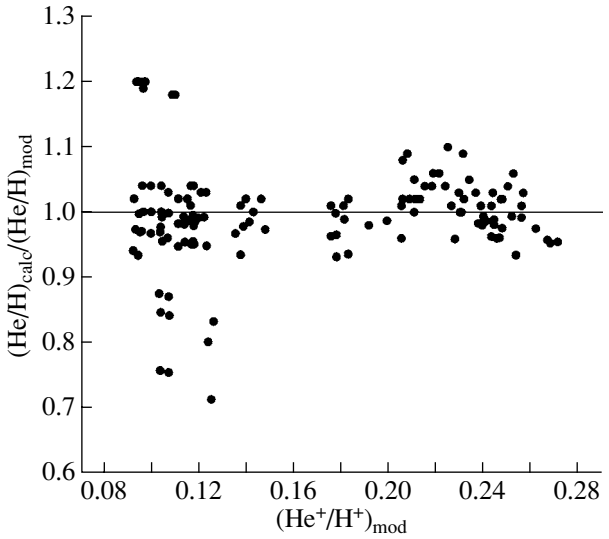

Fig. 2. $(He/H)_{calc}/(He/H)_{mod}$ as a function of $(He^+/H^+)_{mod}$, obtained from the calculations of the PIM grid for the F1 ICFs (Table 1).

We used the new formulas for the recombination coefficients of Benjamin *et al.* [29] to find the helium abundances, which take into account the radiative transfer in the HeI lines and collisional excitation of H and He atoms. We derived the electron densities $n_e(He^+)$ and electron temperatures T_e, optical depths $\tau_{HeI3889}$, relative helium-ion abundances y^+_{aver}, $y^{++}_{4686} \equiv He^{++}/H^+$, and total helium abundances He/H (ICF(He) = 1) for 81 PN in our sample using the χ^2-minimization method of [30] and data for four helium lines ($\lambda\lambda 4471, 5876, 6678, 7065$). If all four of these HeI lines were not present, we used either three lines ($\lambda\lambda 4471, 5876, 6678$) or two lines ($\lambda\lambda\, 4471, 5876$). The calculation results are stored on our ftp server (HeResults.tar.gz).

Table 3 lists the total helium abundances for the 81 type II PN (disk component) for all three sets of HeI lines. The asterisks mark PN that have the HeII $\lambda 4686$ line in their spectra. Column 4 of Table 3 contains the helium abundances averaged using the standard method, $\langle He/H \rangle$. As is noted in [30], taking into account the radiative transfer in the HeI lines considerably improves the accuracy of the helium-ion abundances and, therefore, the accuracy of the total helium abundances in these objects.

The chemical compositions for the Galactic PN in our sample derived using the new ICFs (Table 2) are located on our ftp server (AllPNcomposition.txt). Table 4 presents the chemical compositions for 75 type II Galactic PN, for both type I and type II inhomogeneity (A/H(I), A/H(II)). The mean errors in O/H(I), O/H(II), N/H(I), N/H(II), Ne/H(I), Ne/H(II), S/H(I), S/H(II), Ar/H(I), and A/H(II) are

Table 3. Helium abundances in type II Galactic PN based on two HeI lines ($\lambda\lambda$4471, 5976), three HeI lines ($\lambda\lambda$4471, 5976, 6678), and four HeI lines ($\lambda\lambda$4471, 5976, 6678, 7065). Asterisks (*) denote PN without the HeII λ4686 line

PN	He/H (two HeI lines)	He/H (three HeI lines)	He/H (four HeI lines)	⟨He/H⟩
Cn 2-1	0.0918 ± 0.0010	0.0940 ± 0.0008		0.0929 ± 0.0010
Hb 4	0.1050 ± 0.0018	0.1120 ± 0.0027		0.1085 ± 0.0032
He 2-108*	0.0977 ± 0.0008			0.0977 ± 0.0007
He 2-131*	$0.0355 \pm 5.4e\text{-}05$			0.0355 ± 0.0000
He 2-141	0.1250 ± 0.0078			0.1250 ± 0.0078
Hu 2-1	0.0768 ± 0.0004	0.0826 ± 0.0005		0.0797 ± 0.0006
IC 1297	0.1110 ± 0.0057	0.1110 ± 0.0049	0.1070 ± 0.0032	0.1096 ± 0.0081
IC 1747	0.1050 ± 0.0041	0.1070 ± 0.0034		0.1060 ± 0.0053
IC 2149*	0.0876 ± 0.0018	0.0903 ± 0.0016		0.0889 ± 0.0024
IC 2165	0.1060 ± 0.0037	0.1040 ± 0.0037	0.1040 ± 0.0038	0.1046 ± 0.0064
IC 2448	0.1130 ± 0.0068	0.0963 ± 0.0034		0.1046 ± 0.0076
IC 351	0.0842 ± 0.0038			0.0842 ± 0.0038
IC 3568	0.0862 ± 0.0040			0.0862 ± 0.0040
IC 418*	0.0701 ± 0.0007	0.0693 ± 0.0006		0.0697 ± 0.0007
IC 4191	0.1030 ± 0.0025	0.0984 ± 0.0013		0.1007 ± 0.0028
IC 4406	0.1080 ± 0.0034	0.1150 ± 0.0030	0.0743 ± 0.0012	0.0991 ± 0.0046
IC 4593*	0.0841 ± 0.0007	0.0880 ± 0.0007	$0.0781 \pm 2.7 \times 10^{-9}$	0.0834 ± 0.0010
IC 4634*	0.0798 ± 0.0023	0.0792 ± 0.0019		0.0795 ± 0.0029
IC 4776*	0.0770 ± 0.0024	0.0755 ± 0.0014		0.0762 ± 0.0027
IC 4846	0.0816 ± 0.0005	0.0849 ± 0.0013		0.0832 ± 0.0013
IC 4997	0.0862 ± 0.0014			0.0862 ± 0.0014
IC 5117	0.0828 ± 0.0009			0.0828 ± 0.0009
IC 5217	0.0878 ± 0.0026	0.0918 ± 0.0021		0.0898 ± 0.0026
J 320	0.0849 ± 0.0020	0.0926 ± 0.0042		0.0887 ± 0.0046
J 900	0.0876 ± 0.0038	0.0890 ± 0.0039	0.0886 ± 0.0039	0.0884 ± 0.0066
K 1-7	0.1070 ± 0.0020			0.1070 ± 0.0020
M 1-1	0.1000 ± 0.0094			0.1000 ± 0.0094
M 1-20*	0.0953 ± 0.0030	0.0988 ± 0.0046		0.0970 ± 0.0054
M 1-26*	0.0412 ± 0.0002	0.0485 ± 0.0005		0.0448 ± 0.0005
M 1-72*	0.0714 ± 0.0009			0.0714 ± 0.0008
M 2-23*	0.0826 ± 0.0052	0.0844 ± 0.0021		0.0835 ± 0.0056
M 3-1	0.0858 ± 0.0006			0.0858 ± 0.0006
M 4-18*	0.0417 ± 0.0002			0.0417 ± 0.0001
NGC 1535	0.0929 ± 0.0055	0.0830 ± 0.0019	0.0809 ± 0.0015	0.0856 ± 0.0060
NGC 2022	0.1050 ± 0.0100			0.1050 ± 0.0100
NGC 2371	0.1140 ± 0.0081	0.1080 ± 0.0077		0.1110 ± 0.0111
NGC 2392	0.0870 ± 0.0054	0.0912 ± 0.0040	0.0852 ± 0.0036	0.0878 ± 0.0076
NGC 2438	0.1090 ± 0.0052			0.1090 ± 0.0052
NGC 2452	0.1140 ± 0.0060	0.1060 ± 0.0056		0.1100 ± 0.0082
NGC 2867	0.1020 ± 0.0049	0.1040 ± 0.0041	0.1020 ± 0.0026	0.1026 ± 0.0068

Table 3. (Contd.)

PN	He/H (two HeI lines)	He/H (three HeI lines)	He/H (four HeI lines)	⟨He/H⟩
NGC 3242	0.0859 ± 0.0047	0.0849 ± 0.0038	0.0793 ± 0.0021	0.0833 ± 0.0063
NGC 3587	0.0779 ± 0.0020			0.0779 ± 0.0020
NGC 3918	0.0958 ± 0.0039	0.0948 ± 0.0039		0.0953 ± 0.0055
NGC 40*	0.0441 ± 0.0006	0.0444 ± 0.0006	$0.0231 \pm 4.5 \times 10^{-10}$	0.0372 ± 0.0008
NGC 5315	0.1030 ± 0.0005	0.1020 ± 0.0004		0.1025 ± 0.0006
NGC 5882*	0.1060 ± 0.0014	0.1060 ± 0.0011		0.1060 ± 0.0017
NGC 6153	0.1100 ± 0.0013	0.1060 ± 0.0012		0.1080 ± 0.0017
NGC 6309	0.1080 ± 0.0060	0.1100 ± 0.0057	0.1030 ± 0.0052	0.1070 ± 0.0097
NGC 6326	0.1130 ± 0.0061	0.1040 ± 0.0050	0.1000 ± 0.0049	0.1056 ± 0.0092
NGC 6369	0.0968 ± 0.0046	0.0749 ± 0.0008		0.0858 ± 0.0046
NGC 6439	0.1130 ± 0.0021	0.1120 ± 0.0021		0.1125 ± 0.0029
NGC 6445	0.0909 ± 0.0049	0.0973 ± 0.0049	0.0859 ± 0.0049	0.0913 ± 0.0084
NGC 650	0.1070 ± 0.0031	0.1060 ± 0.0030	0.1040 ± 0.0028	0.1056 ± 0.0051
NGC 6543*	0.1090 ± 0.0016	0.1110 ± 0.0015		0.1100 ± 0.0021
NGC 6563	0.1180 ± 0.0047	0.1090 ± 0.0017		0.1135 ± 0.0049
NGC 6565	0.0983 ± 0.0029	0.0970 ± 0.0025	0.0752 ± 0.0017	0.0901 ± 0.0041
NGC 6567	0.0916 ± 0.0009	0.1040 ± 0.0062		0.0978 ± 0.0062
NGC 6572*	0.0901 ± 0.0011	0.0943 ± 0.0009		0.0922 ± 0.0014
NGC 6578	0.0995 ± 0.0005	0.0976 ± 0.0004		0.0985 ± 0.0006
NGC 6629*	0.0926 ± 0.0019	0.0859 ± 0.0005		0.0892 ± 0.0019
NGC 6720	0.1080 ± 0.0037	0.1130 ± 0.0035	0.0993 ± 0.0026	0.1067 ± 0.0057
NGC 6741	0.0933 ± 0.0039	0.0967 ± 0.0038	0.0895 ± 0.0036	0.0931 ± 0.0065
NGC 6751*	0.1030 ± 0.0016	0.0968 ± 0.0006	$0.0908 \pm 1.3 \times 10^{-9}$	0.0968 ± 0.0017
NGC 6804	0.0963 ± 0.0076	0.0971 ± 0.0076		0.0967 ± 0.0107
NGC 6807	0.0910 ± 0.0015			0.0910 ± 0.0015
NGC 6818	0.0980 ± 0.0065	0.0999 ± 0.0065		0.0989 ± 0.0091
NGC 6826*	0.0917 ± 0.0020	0.0942 ± 0.0017		0.0929 ± 0.0026
NGC 6833	0.0734 ± 0.0023	0.0969 ± 0.0056		0.0851 ± 0.0060
NGC 6853	0.1090 ± 0.0037	0.1110 ± 0.0038		0.1100 ± 0.0053
NGC 6881	0.0972 ± 0.0038	0.0981 ± 0.0037		0.0976 ± 0.0053
NGC 6884	0.1100 ± 0.0024	0.1080 ± 0.0023		0.1090 ± 0.0033
NGC 6886	0.0942 ± 0.0040	0.0913 ± 0.0039		0.0927 ± 0.0055
NGC 6891*	0.0921 ± 0.0022	0.0817 ± 0.0007		0.0869 ± 0.0023
NGC 6894	0.0910 ± 0.0015	0.0927 ± 0.0021		0.0918 ± 0.0025
NGC 7009	0.1120 ± 0.0036	0.1080 ± 0.0018		0.1100 ± 0.0040
NGC 7026	0.1150 ± 0.0020	0.0993 ± 0.0011		0.1071 ± 0.0022
NGC 7027	0.0965 ± 0.0046	0.1050 ± 0.0046		0.1007 ± 0.0065
NGC 7139	0.1060 ± 0.0021			0.1060 ± 0.0021
NGC 7662	0.0849 ± 0.0050	0.0871 ± 0.0045		0.0860 ± 0.0067
PB 4	0.0940 ± 0.0100			0.0940 ± 0.0100
Tc 1*	0.0662 ± 0.00051	0.0667 ± 0.0004		0.0664 ± 0.0006

Table 4. Chemical compositions of type II Galactic PN for the two types of inhomogeneity: $\frac{A}{H}(I)$ and $\frac{A}{H}(II)$

PN	$\frac{O}{H}(I)$	$\frac{O}{H}(II)$	$\frac{N}{H}(I)$	$\frac{N}{H}(II)$	$\frac{Ne}{H}(I)$	$\frac{Ne}{H}(II)$	$\frac{S}{H}(I)$	$\frac{S}{H}(II)$	$\frac{Ar}{H}(I)$	$\frac{Ar}{H}(II)$
A2	5.32×10^{-4}	5.44×10^{-4}	1.04×10^{-4}	1.05×10^{-4}	1.56×10^{-4}		1.13×10^{-5}	1.16×10^{-5}		
A4	5.31×10^{-4}	5.45×10^{-4}	2.28×10^{-4}	2.30×10^{-4}	8.87×10^{-5}		9.20×10^{-6}	9.38×10^{-6}		
BD+30	1.87×10^{-6}	1.88×10^{-6}	8.88×10^{-5}	9.08×10^{-5}			4.52×10^{-6}	4.48×10^{-6}		
Cn2-1	6.10×10^{-4}	7.72×10^{-4}	9.47×10^{-5}	9.68×10^{-5}	1.17×10^{-4}		8.37×10^{-6}	8.02×10^{-6}	2.02×10^{-6}	1.71×10^{-6}
Hb4	5.36×10^{-4}	5.48×10^{-4}	2.54×10^{-4}	2.39×10^{-4}	1.14×10^{-4}		1.29×10^{-5}	1.42×10^{-5}	3.32×10^{-6}	3.29×10^{-6}
He2-108	9.88×10^{-5}	1.01×10^{-4}	1.99×10^{-5}	1.99×10^{-5}	3.97×10^{-6}		2.52×10^{-7}	2.45×10^{-7}		
He2-141	2.68×10^{-4}	3.43×10^{-4}	9.51×10^{-5}	1.27×10^{-4}	5.05×10^{-5}		3.75×10^{-6}	3.79×10^{-6}	1.89×10^{-6}	
Hu2-1	2.28×10^{-4}	1.87×10^{-4}	3.44×10^{-4}	2.13×10^{-5}	1.68×10^{-5}		1.53×10^{-6}	1.57×10^{-6}	4.26×10^{-7}	4.31×10^{-7}
IC1297	5.92×10^{-4}	7.63×10^{-4}	1.54×10^{-4}	1.46×10^{-4}	1.21×10^{-4}		9.60×10^{-6}	9.10×10^{-6}	1.87×10^{-6}	1.49×10^{-6}
IC1747	6.69×10^{-4}	7.66×10^{-4}	1.08×10^{-4}	1.29×10^{-4}	1.15×10^{-4}		7.29×10^{-6}	7.10×10^{-6}	1.81×10^{-6}	1.52×10^{-6}
IC2149	3.49×10^{-4}	2.59×10^{-4}	1.22×10^{-4}	2.29×10^{-5}	3.17×10^{-5}		2.36×10^{-6}	2.40×10^{-6}	7.12×10^{-7}	7.11×10^{-7}
IC2165	6.67×10^{-4}	7.30×10^{-4}	8.18×10^{-5}	1.30×10^{-4}	1.02×10^{-4}		5.95×10^{-6}	5.94×10^{-6}	3.35×10^{-6}	
IC418	1.80×10^{-4}	2.67×10^{-4}	2.03×10^{-4}	2.90×10^{-5}	3.74×10^{-6}		4.13×10^{-6}	4.06×10^{-6}	3.86×10^{-7}	3.79×10^{-7}
IC4191	3.61×10^{-4}	3.57×10^{-4}	1.03×10^{-4}	9.99×10^{-5}	1.14×10^{-4}		7.79×10^{-6}	7.98×10^{-6}	1.88×10^{-6}	1.82×10^{-6}
IC4406	4.70×10^{-4}	3.67×10^{-4}	5.24×10^{-4}	2.24×10^{-4}	1.07×10^{-4}		8.92×10^{-6}	9.76×10^{-6}	2.03×10^{-6}	2.01×10^{-6}
IC4593	2.34×10^{-4}	2.27×10^{-4}	1.32×10^{-5}	1.33×10^{-5}	3.79×10^{-5}		2.32×10^{-6}	2.32×10^{-6}	6.67×10^{-7}	6.64×10^{-7}
IC4634	3.26×10^{-4}	2.61×10^{-4}	1.60×10^{-5}	1.61×10^{-5}	6.72×10^{-5}	5.99×10^{-5}	2.17×10^{-6}	2.30×10^{-6}	8.37×10^{-7}	8.76×10^{-7}
IC4776	8.42×10^{-5}	6.65×10^{-5}	2.58×10^{-5}	7.85×10^{-6}	1.91×10^{-5}	1.57×10^{-5}	1.98×10^{-6}	1.90×10^{-6}	4.10×10^{-7}	4.96×10^{-7}
IC4846	3.86×10^{-4}	3.10×10^{-4}	3.80×10^{-5}	3.05×10^{-5}	7.05×10^{-5}	6.37×10^{-5}	4.22×10^{-6}	4.16×10^{-6}	7.95×10^{-7}	8.26×10^{-7}
IC4997	3.68×10^{-4}	1.54×10^{-4}	1.70×10^{-5}	2.07×10^{-5}	2.05×10^{-5}	1.99×10^{-5}	4.25×10^{-6}	4.01×10^{-6}	8.62×10^{-7}	8.62×10^{-7}
IC5117	3.76×10^{-4}	3.59×10^{-4}	1.07×10^{-4}	5.78×10^{-5}	9.64×10^{-5}		6.26×10^{-6}	4.42×10^{-6}	1.76×10^{-6}	1.13×10^{-6}
IC5217	3.53×10^{-4}	4.18×10^{-4}	7.75×10^{-5}	7.77×10^{-5}	8.50×10^{-5}		7.22×10^{-6}	7.32×10^{-6}	2.09×10^{-6}	
J900	2.67×10^{-4}	2.72×10^{-4}	3.54×10^{-5}	3.48×10^{-5}	6.05×10^{-5}		2.36×10^{-6}	2.40×10^{-6}	8.14×10^{-7}	5.24×10^{-7}
K1-7	3.77×10^{-4}	3.65×10^{-4}	1.57×10^{-4}	1.58×10^{-4}	6.22×10^{-5}		6.78×10^{-6}	7.04×10^{-6}		
M1-1	9.00×10^{-5}		3.96×10^{-5}		1.04×10^{-5}		2.37×10^{-6}		2.33×10^{-6}	

Table 4. (Contd.)

PN	$\frac{O}{H}$(I)	$\frac{O}{H}$(II)	$\frac{N}{H}$(I)	$\frac{N}{H}$(II)	$\frac{Ne}{H}$(I)	$\frac{Ne}{H}$(II)	$\frac{S}{H}$(I)	$\frac{S}{H}$(II)	$\frac{Ar}{H}$(I)	$\frac{Ar}{H}$(II)
M1-20	1.58×10^{-4}	1.60×10^{-4}	2.59×10^{-5}	1.96×10^{-5}	3.47×10^{-5}	3.27×10^{-5}	1.28×10^{-6}	1.29×10^{-6}	4.64×10^{-7}	4.96×10^{-7}
M1-26	1.65×10^{-5}		3.76×10^{-4}				9.59×10^{-6}	9.71×10^{-6}		
M1-27			3.89×10^{-4}	3.80×10^{-4}			1.78×10^{-5}	1.77×10^{-5}		
M1-72	6.96×10^{-5}	7.15×10^{-5}	1.47×10^{-5}	1.45×10^{-5}			1.93×10^{-6}	1.81×10^{-6}	2.74×10^{-7}	2.68×10^{-7}
M2-23	3.03×10^{-4}	1.90×10^{-4}	4.53×10^{-5}	2.95×10^{-5}	5.41×10^{-5}		4.27×10^{-6}	4.15×10^{-6}	7.47×10^{-7}	7.75×10^{-7}
M2-51	3.11×10^{-4}	3.10×10^{-4}	2.01×10^{-4}	2.02×10^{-4}	4.82×10^{-5}					
M3-1	1.91×10^{-4}	1.63×10^{-4}	6.55×10^{-5}	4.68×10^{-5}	3.57×10^{-5}		5.88×10^{-6}	6.40×10^{-6}	1.08×10^{-6}	9.96×10^{-7}
NGC 2371	4.47×10^{-4}	4.29×10^{-4}	2.12×10^{-4}	1.64×10^{-4}	7.97×10^{-5}		1.46×10^{-5}	1.48×10^{-5}	3.98×10^{-6}	2.41×10^{-6}
NGC 2392	3.16×10^{-4}	3.40×10^{-4}	9.44×10^{-5}	1.08×10^{-4}	5.94×10^{-5}		6.16×10^{-6}	6.21×10^{-6}	1.01×10^{-6}	1.02×10^{-6}
NGC 2438	6.49×10^{-4}	5.77×10^{-4}	2.27×10^{-4}	1.21×10^{-4}	8.86×10^{-5}		1.04×10^{-5}	1.05×10^{-5}	2.95×10^{-6}	2.94×10^{-6}
NGC 2452	6.72×10^{-4}	7.35×10^{-4}	3.49×10^{-4}	3.35×10^{-4}	1.29×10^{-4}		2.11×10^{-5}	1.96×10^{-5}	3.96×10^{-6}	3.39×10^{-6}
NGC 2867	3.25×10^{-4}	2.89×10^{-4}	6.01×10^{-5}	5.21×10^{-5}	6.42×10^{-5}	6.29×10^{-5}	3.90×10^{-6}	3.98×10^{-6}	9.88×10^{-7}	1.02×10^{-6}
NGC 3587	2.47×10^{-4}	2.42×10^{-4}	7.80×10^{-5}	7.86×10^{-5}	4.65×10^{-5}		3.09×10^{-6}	3.17×10^{-6}	1.48×10^{-6}	1.48×10^{-6}
NGC 3918	9.52×10^{-4}	7.81×10^{-4}	2.60×10^{-4}	1.34×10^{-4}	1.26×10^{-4}		1.13×10^{-5}	1.15×10^{-5}	3.52×10^{-6}	2.21×10^{-6}
NGC 40	9.81×10^{-6}	9.84×10^{-6}	1.06×10^{-4}	1.07×10^{-4}			2.60×10^{-6}	2.58×10^{-6}		
NGC 5315	2.30×10^{-4}	2.01×10^{-4}	2.66×10^{-4}	8.79×10^{-5}	5.21×10^{-5}	4.49×10^{-5}	8.97×10^{-6}	9.06×10^{-6}	1.52×10^{-6}	1.52×10^{-6}
NGC 5882	1.15E-3	1.24E-3	1.19×10^{-4}	1.32×10^{-4}	2.17×10^{-4}		1.43×10^{-5}	1.58×10^{-5}	4.55×10^{-6}	
NGC 6153	7.20×10^{-4}	7.15×10^{-4}	1.46×10^{-4}	1.45×10^{-4}	2.44×10^{-4}		7.56×10^{-6}	8.79×10^{-6}	3.59×10^{-6}	3.68×10^{-6}
NGC 6309	4.88×10^{-4}		1.12×10^{-4}				9.62×10^{-6}	9.85×10^{-6}		
NGC 6326	6.91×10^{-4}		1.80×10^{-4}	1.84×10^{-4}			1.08×10^{-5}	1.06×10^{-5}	2.72×10^{-6}	
NGC 6369	2.42×10^{-4}	2.82×10^{-4}	8.82×10^{-5}	1.03×10^{-4}	4.64×10^{-5}		3.95×10^{-6}	4.00×10^{-6}	1.40×10^{-6}	1.43×10^{-6}
NGC 6439	3.38×10^{-4}	3.46×10^{-4}	1.48×10^{-4}	1.79×10^{-4}	1.11×10^{-4}		8.27×10^{-6}	8.41×10^{-6}	1.84×10^{-6}	6.24×10^{-7}
NGC 6445	5.23×10^{-4}	5.11×10^{-4}	2.87×10^{-4}	2.79×10^{-4}	1.11×10^{-4}		1.02×10^{-5}	1.05×10^{-5}	2.52×10^{-6}	2.34×10^{-6}
NGC 650	2.81×10^{-4}	2.90×10^{-4}	1.43×10^{-4}	1.43×10^{-4}	8.61×10^{-5}	8.13×10^{-5}	5.34×10^{-6}	5.37×10^{-6}	1.16×10^{-6}	1.16×10^{-6}
NGC 6543	2.91×10^{-4}	3.67×10^{-4}	3.16×10^{-5}	3.18×10^{-5}	1.08×10^{-4}	8.67×10^{-5}	4.47×10^{-6}	4.56×10^{-6}	1.66×10^{-6}	1.87×10^{-6}

Table 4. (Contd.)

PN	$\frac{O}{H}$(I)	$\frac{O}{H}$(II)	$\frac{N}{H}$(I)	$\frac{N}{H}$(II)	$\frac{Ne}{H}$(I)	$\frac{Ne}{H}$(II)	$\frac{S}{H}$(I)	$\frac{S}{H}$(II)	$\frac{Ar}{H}$(I)	$\frac{Ar}{H}$(II)
NGC 6563	4.01×10^{-4}	4.15×10^{-4}	2.09×10^{-4}	2.10×10^{-5}			3.61×10^{-6}	3.69×10^{-6}	1.51×10^{-6}	1.50×10^{-6}
NGC 6565	4.11×10^{-4}	4.90×10^{-4}	1.95×10^{-5}	1.92×10^{-5}	1.05×10^{-4}	1.15×10^{-4}	8.69×10^{-6}	8.94×10^{-6}	1.93×10^{-6}	1.92×10^{-6}
NGC 6567	2.73×10^{-4}	3.03×10^{-4}	2.17×10^{-5}	2.17×10^{-5}	4.32×10^{-5}		1.99×10^{-6}	2.04×10^{-6}	5.39×10^{-7}	6.01×10^{-7}
NGC 6572	3.62×10^{-4}	3.31×10^{-4}	7.06×10^{-5}	4.26×10^{-5}	8.17×10^{-5}	7.38×10^{-5}	3.50×10^{-6}	3.47×10^{-6}	1.78×10^{-6}	1.93×10^{-6}
NGC 6578	3.68×10^{-4}	3.93×10^{-4}	5.03×10^{-5}	5.07×10^{-5}	1.73×10^{-4}	1.40×10^{-4}	1.18×10^{-6}	1.18×10^{-6}	1.79×10^{-6}	1.96×10^{-6}
NGC 6629	4.54×10^{-4}	4.55×10^{-4}	3.61×10^{-5}	3.64×10^{-5}	6.80×10^{-5}		7.51×10^{-7}	7.75×10^{-7}	1.94×10^{-6}	1.96×10^{-6}
NGC 6720	4.86×10^{-4}	4.57×10^{-4}	1.81×10^{-4}	1.78×10^{-4}	1.13×10^{-4}	1.23×10^{-4}	4.54×10^{-6}	4.76×10^{-6}	1.82×10^{-6}	1.82×10^{-6}
NGC 6741	5.57×10^{-4}	5.46×10^{-4}	1.94×10^{-4}	1.90×10^{-4}	1.30×10^{-4}		7.93×10^{-6}	8.04×10^{-6}	3.22×10^{-6}	2.03×10^{-6}
NGC 6751	6.22×10^{-4}	6.15×10^{-4}	1.70×10^{-4}	1.64×10^{-4}	1.02×10^{-4}		6.66×10^{-6}	6.68×10^{-6}	1.69×10^{-6}	1.69×10^{-6}
NGC 6807	1.75×10^{-4}	1.54×10^{-4}	2.13×10^{-5}	2.11×10^{-5}	4.68×10^{-5}	4.31×10^{-5}	2.43×10^{-6}	2.40×10^{-6}	6.27×10^{-7}	6.58×10^{-7}
NGC 6818					1.19×10^{-4}					
NGC 6826	2.55×10^{-4}	2.84×10^{-4}	2.77×10^{-5}	2.80×10^{-5}	6.53×10^{-5}	4.44×10^{-5}	2.69×10^{-6}	2.60×10^{-6}	9.24×10^{-7}	6.27×10^{-7}
NGC 6833	9.60×10^{-4}	9.00×10^{-5}	3.58×10^{-5}	2.26×10^{-5}	2.81×10^{-5}	2.38×10^{-5}	1.11×10^{-6}	1.07×10^{-6}	3.76×10^{-7}	4.18×10^{-7}
NGC 6853	4.98×10^{-4}	5.05×10^{-4}	5.34×10^{-4}	1.70×10^{-4}	1.36×10^{-4}		1.36×10^{-5}	1.31×10^{-5}	3.37×10^{-6}	3.49×10^{-6}
NGC 6881	3.18×10^{-4}	3.19×10^{-4}	1.32×10^{-4}	1.29×10^{-4}	6.98×10^{-5}		5.19×10^{-6}	5.28×10^{-6}	2.20×10^{-6}	1.63×10^{-6}
NGC 6884	9.87×10^{-4}	1.25E-3	1.39×10^{-4}	1.62×10^{-4}	1.77×10^{-4}		1.03×10^{-5}	1.05×10^{-5}	5.02×10^{-6}	
NGC 6886	8.76×10^{-4}	7.97×10^{-4}	3.12×10^{-4}	2.02×10^{-4}	1.72×10^{-4}		9.80×10^{-6}	9.92×10^{-6}	4.02×10^{-6}	1.69×10^{-6}
NGC 6891	2.73×10^{-4}	2.76×10^{-5}	2.94×10^{-5}	2.97×10^{-5}	6.59×10^{-5}	4.47×10^{-5}	7.90×10^{-7}	2.74×10^{-7}	8.84×10^{-7}	5.41×10^{-7}
NGC 6894	2.43×10^{-4}	2.42×10^{-4}	2.14×10^{-4}	2.06×10^{-4}	5.62×10^{-5}		1.05×10^{-5}	1.06×10^{-5}	1.27×10^{-6}	1.28×10^{-6}
NGC 7009	7.44×10^{-4}		1.34×10^{-4}		1.70×10^{-4}		1.40×10^{-5}		2.98×10^{-6}	
NGC 7026	4.06×10^{-4}	3.81×10^{-4}	1.84×10^{-4}	1.65×10^{-4}	1.48×10^{-5}	1.48×10^{-4}	1.14×10^{-5}	1.17×10^{-5}	2.56×10^{-6}	2.62×10^{-6}
NGC 7027	2.09×10^{-4}	2.04×10^{-4}	1.12×10^{-4}	7.39×10^{-5}	4.68×10^{-5}		6.24×10^{-6}	5.67×10^{-6}	1.97×10^{-6}	1.79×10^{-6}
NGC 7139	2.71×10^{-4}	2.69×10^{-4}	1.40×10^{-4}	1.40×10^{-4}	5.32×10^{-5}		8.10×10^{-6}	8.14×10^{-6}		
PB4	4.54×10^{-4}		7.13×10^{-5}		8.71×10^{-5}		8.14×10^{-6}		2.38×10^{-6}	
Tc1	1.03×10^{-4}	1.55×10^{-4}	1.00×10^{-4}	1.50×10^{-5}	3.30×10^{-6}		1.55×10^{-6}	1.52×10^{-6}	3.27×10^{-7}	3.20×10^{-7}

Table 5. Y_p and dY/dZ for type II PN for the two types of inhomogeneity (I and II) and three sets of HeI lines

No.	Y_p	ΔY_p	dY/dZ	$\Delta(dY/dZ)$	Number	Notes
1	0.240	1.32×10^{-3}	3.78	0.188	51	PN, I (*)
2	0.243	9.73×10^{-4}	3.42	0.147	70	PN, I (*, together with HII regions)
3	0.239	9.04×10^{-4}	5.41	0.165	47	PN, II (*)
4	0.241	7.70×10^{-4}	5.10	0.147	69	PN, II (*, together with HII regions)
5	0.264	1.74×10^{-3}	1.82	0.225	35	PN, I (**)
6	0.253	1.08×10^{-3}	3.20	0.151	57	PN, I (**, together with HII regions)
7	0.264	1.04×10^{-3}	2.32	0.167	33	PN, II (**)
8	0.258	8.40×10^{-4}	3.28	0.143	55	PN, II (**, together with HII regions)
9	0.245	3.11×10^{-3}	3.77	0.630	34	PN, I (***, together with HII regions)
10	0.244	3.15×10^{-3}	4.58	0.792	33	PN, II (***, together with HII regions)
11	0.248	3.63×10^{-3}	3.32	0.508	82	PN, I ($\langle$ He/ H$\rangle$, together with HII regions)
12	0.248	3.62×10^{-3}	4.28	0.617	85	PN, II ($\langle$He/H$\rangle$, together with HII regions)
13	0.251	1.49×10^{-3}	2.88	0.229	49	PN, I ($\langle$He/H$\rangle$, Z(I)(O/H))
14	0.249	1.03×10^{-3}	3.18	0.174	71	PN, I ($\langle$He/H$\rangle$, Z(I)(O/H), together with HII regions)
15	0.257	1.08×10^{-3}	2.66	0.206	45	PN, II ($\langle$He/H$\rangle$, Z(II)(O/H))
16	0.253	8.72×10^{-4}	3.26	0.181	66	PN, II ($\langle$He/H$\rangle$, Z(II)(O/H), together with HII regions)

* Two HeI lines (λ4471, λ5876)
** Three HeI lines (λ4471, λ5876, λ6678)
*** Four HeI lines (λ4471, λ5876, λ6678, λ7065)

1.59×10^{-5}, 7.22×10^{-6}, 9.12×10^{-6}, 4.15×10^{-6}, 7.96×10^{-7}, 1.62×10^{-6}, 3.00×10^{-7}, 1.96×10^{-7}, 2.65×10^{-8}, and 2.67×10^{-8}, respectively.

5. DETERMINATION OF Y_p AND dY/dZ

We analyzed the Y–Z dependence in order to determine the pre-Galactic helium abundance Y_p and its enrichment dY/dZ, where Y and Z are the mass abundances of helium and of heavy elements:

$$Y = \frac{4\mathrm{He/H}(1-Z)}{1+4\mathrm{He/H}}, \quad Z = \frac{Za}{1+4\mathrm{He/H}+Za}, \tag{4}$$

$$Za = 14\mathrm{N/H} + 16\mathrm{O/H} + 20\mathrm{Ne/H} + 32\mathrm{S/H} + 40\mathrm{Ar/H}. \tag{5}$$

The extrapolation of this dependence to $Z = 0$ yields Y_p, and its slope corresponds to dY/dZ.

Note that we plotted the Y–Z relationship using only type II PN. We estimated the masses of the ionized gas in the PN for all the nebulae of our sample, with the nucleus mass taken into account:

$$M_i = M_* + M_{\mathrm{neb}}. \tag{6}$$

The masses of the PN nuclei M_* were taken from [35], and we took into consideration only the ionized part of the gas (H and He) when calculating the masses of the PN envelopes M_{neb}. The scatter of masses M_i for the disk component of the PN is small (0.7–$1.5 M_\odot$), testifying that our PN sample is homogeneous. The results of the calculations for all the PN are available on our ftp server (PNmasses.txt).

When finding Y_p, we eliminated objects without the HeII λ4686 line in their spectra, since we derived the relative helium-ion abundances $\mathrm{He^{++}/H^+}$ using only this line, and the uncertainty in its observed intensity introduces an uncertainty in the total helium content $\mathrm{He/H} = \mathrm{He^+/H^+} + \mathrm{He^{++}/H^+}$. In order to determine Y_p more accurately, we expanded the sample by including HII regions in blue compact dwarf galaxies [31]. Note that determining Z requires the abundances of all the heavy elements listed above [see formulas (4), (5)], which limits the number of objects suitable for the analysis. To take this into account, we plotted dependences of the form Z–O/H for the two sets of Z values (the two types of inhomogeneity). It is obvious that these relations are linear, and that they can be represented by the following approximating

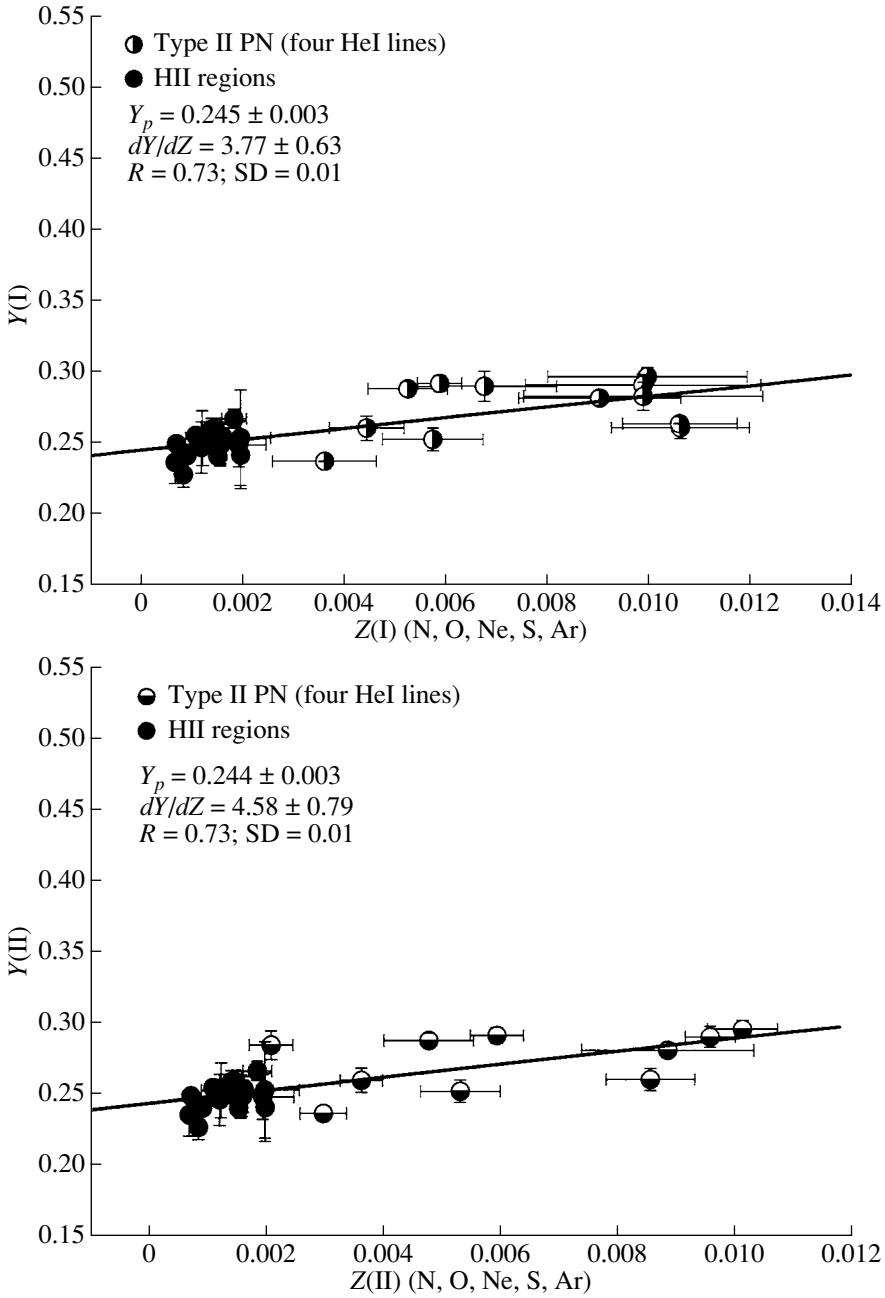

Fig. 3. The $Y(\mathrm{I})-Z(\mathrm{I})$ and $Y(\mathrm{II})-Z(\mathrm{II})$ relationships for type II PN (four HeI lines) together with HII regions for the two types of inhomogeneity in the gas-density distribution in their envelopes.

formulas when determining Z for Galactic PN ($Z(\mathrm{I})$ corresponds to type I and $Z(\mathrm{II})$ to type II inhomogeneity; r is the correlation coefficient):

$$Z(\mathrm{I}) = 17.28 \times \mathrm{O/H} + 3.29 \times 10^{-4}, \quad r = 0.95, \tag{7}$$

$$Z(\mathrm{II}) = 15.61 \times \mathrm{O/H} + 1.02 \times 10^{-3}, \quad r = 0.95. \tag{8}$$

Table 5 lists the values of Y_p and dY/dZ for the different versions of the $Y-Z$ dependences. The average values $\langle \mathrm{He/H} \rangle$ correspond to the data from Table 3, and the values of $Z(\mathrm{I})(\mathrm{O/H})$ and $Z(\mathrm{II})(\mathrm{O/H})$ to equations (7) and (8). The version based on all four HeI lines ($\lambda\lambda 4471, 5876, 6678, 7065$) is the most accurate, and the data are plotted for type II PN together with HII regions in blue compact dwarf galaxies. The resulting values $Y_p(\mathrm{I}) = 0.245 \pm 0.003$ and $Y_p(\mathrm{II}) = 0.247 \pm 0.004$ coincide with our previous calculations [28], and also agree well with the recent data of [32–34] ($Y_p = 0.2452 \pm 0.0015$ [32], $Y_p =$

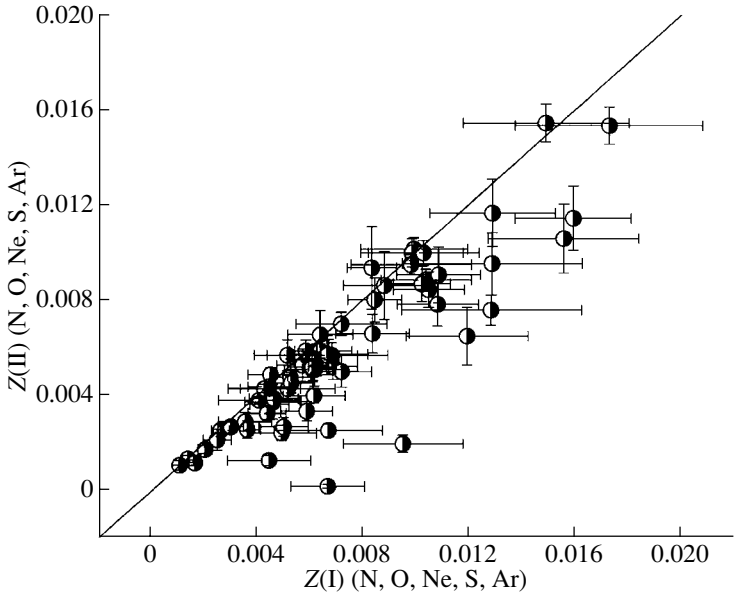

Fig. 4. Comparison of the heavy-element abundances for type II PN for the two types of inhomogeneity in the gas-density distribution in their envelopes, Z(I) and Z(II). The straight line corresponds to identical values for these quantities.

0.248 ± 0.003 [33], $Y_p = 0.245 \pm 0.004$ [34]). Figure 3 shows the $Y-Z$ dependences for type II PN (four HeI lines) for the two types of inhomogeneity in the distribution of the gas density in their envelopes (Y(I) − Z(I) corresponds to type I and Y(II) − Z(II) to type II inhomogeneity).

Figure 4 presents the heavy-element contents Z(I) and Z(II) for the type II PN for the two types of inhomogeneity. The straight line corresponds to identical values for these two quantities. We can see that the presence of fluctuations (type II inhomogeneity) lowers the value of Z for most of the PN. It is obvious that the origin of this behavior is an underabundance of ions within the fluctuations themselves, which is reflected in the total abundance of a particular element. We also compared these same values of Z(I) and Z(II) with the results for Z (C, N, O, Ne, S, Ar) from our previous work [28]. The previous values of Z are somewhat higher, presumably due to the fact that we have taken into account the presence of gas-density fluctuations in the present paper and the C/H content in the previous work.

We also analyzed gradients of the elemental abundances with distance from the Galactic center for type II PN. We adopted the PN distances R from [35], and the elemental abundances from Tables 3 and 4. The abundance gradients for each element studied, $d[\log(\mathrm{A/H})]/dR$, in kpc^{-1} are

$(\mathrm{He/H})^{*} = -0.0124 \pm 8.97 \times 10^{-6}$ ($n = 16$);

$(\mathrm{He/H})^{**} = -0.0082 \pm 2.86 \times 10^{-6}$ ($n = 60$);

O/H(I) $= -0.0252 \pm 0.0118$ ($n = 65$); O/H(II) $= -0.0180 \pm 0.0183$ ($n = 61$);

N/H(I) $= -0.0287 \pm 0.0179$ ($n = 66$); N/H(II) $= -0.0215 \pm 0.0201$ ($n = 61$);

Ne/H(I) $= -0.0330 \pm 0.0131$ ($n = 59$); Ne/H(II) $= -0.0322 \pm 0.0312$ ($n = 16$);

S/H(I) $= -0.0255 \pm 0.0139$ ($n = 62$); S/H(II) $= -0.0234 \pm 0.0150$ ($n = 59$);

Ar/H(I) $= -0.0247 \pm 0.0156$ ($n = 55$); Ar/H(II) $= -0.0280 \pm 0.0169$ ($n = 48$).

When deriving the helium-abundance gradients, we used the data for PN with four HeI lines ($(\mathrm{He/H})^{*}$) and the average values $\langle \mathrm{He/H} \rangle$ ($(\mathrm{He/H})^{**}$), taking into account the corresponding errors. For the abundance gradients of the remaining elements, data for the two types of inhomogeneity are given (A/H(I) and A/H(II)); these coincide with our previous calculations [28] within the errors. Our calculations cover Galactocentric distances $R = 2-15$ kpc. The number of objects (n) used to find each gradient is given in parentheses.

Although the distance scale adopted strongly affects the values of the gradients, our helium-abundance gradients coincide with the data of [36], and the gradients of other elements coincide with the data of [37] within the errors.

6. CONCLUSIONS

We have determined the abundances of He, N, O, Ne, S, and Ar in 193 Galactic planetary nebulae allowing for two types of inhomogeneity of the nebular gas density. We have derived the chemical compositions of the nebular gas using new approximating

formulas for the ionization correction factors based on a calculated grid of photoionization models for the planetary nebulae. When deriving the expressions for the ICFs, we used for the first time the relative ion abundances $(A^{+i}/H^+)_{diagn}$ obtained from diagnostics of the integrated PIM spectra. The derived expressions were tested to determine if they could reproduce the chemical compositions $(A/H)_{mod}$ specified in the PIMs. In most cases, the ICFs are able to reproduce the chemical compositions of the nebular gas in the PN to within $\leq 10\%$. We also tested a set of empirical relationships for the ICFs that have been used in various other studies to determine the chemical compositions of the gas in nebular objects. We determined the He abundance using the new recombination coefficients of Benjamin *et al.* [29], which take into account the radiative transfer in HeI lines and the collisional excitation of H and He atoms. We have analyzed the $Y-Z$ dependences for various versions of the helium abundance for both PN alone and for PN together with HII regions in blue compact dwarf galaxies. We also determined the primordial helium abundance Y_p and the enrichment of this value dY/dZ. We consider the values $Y_p(\mathrm{I}) = 0.245 \pm 0.003$ and $dY/dZ(\mathrm{I}) = 3.77 \pm 0.63$ and $Y_p(\mathrm{II}) = 0.247 \pm 0.004$ and $dY/dZ(\mathrm{II}) = 4.09 \pm 0.93$ to be the most accurate estimates for the two types of inhomogeneity considered. Our estimates of Y_p and dY/dZ are consistent with those of the previous studies [32–34].

REFERENCES

1. R. L. Kingsburgh and M. J. Barlow, Mon. Not. R. Astron. Soc. **271**, 257 (1994).
2. G. Stasinska, M. G. Richer, and M. L. Mc Call, Astron. Astrophys. **336**, 667 (1998).
3. C. R. O'Dell, B. Balick, A. R. Hajian, *et al.*, Astron. J. **123**, 3329 (2002).
4. J. Meaburn, C. A. Clayton, M. Bryce, *et al.*, Mon. Not. R. Astron. Soc. **294**, 201 (1998).
5. P. J. Huggins and N. Mauron, Astron. Astrophys. **393**, 273 (2002).
6. R. J. R. Williams, Mon. Not. R. Astron. Soc. **310**, 789 (1999).
7. K. J. Borkowski, J. P. Harrington, Z. Tsvetanov, and R. E. S. Clegg, Astrophys. J. Lett. **415**, L47 (1993).
8. S. M. Viegas and R. E. S. Clegg, Mon. Not. R. Astron. Soc. **271**, 993 (1994).
9. M. Peimbert, Bol. Obs. Tonantzintla Tacubaya **6**, 29 (1971).
10. R. H. Rubin, Astrophys. J., Suppl. Ser. **69**, 897 (1989).
11. J. Kingdon and G. J. Ferland, Astrophys. J. **450**, 691 (1995).
12. S. R. Och, L. B. Lucy, and M. R. Rosa, Astron. Astrophys. **336**, 301 (1998).
13. B. Ercolano, C. Morisset, M. J. Barlow, *et al.*, astro-ph/0209417.
14. K. A. Olive, G. Steigman, and E. D. Skillman, Astrophys. J. **483**, 788 (1997).
15. Yu. I. Izotov and T. X. Thuan, Astrophys. J. **497**, 227 (1998).
16. P. R. Amnuel, Mon. Not. R. Astron. Soc. **261**, 263 (1993).
17. V. V. Golovatyi, V. I. Dmitrenko, Yu. F. Mal'kov, and O. V. Rokach, Astron. Zh. **70** (4), 691 (1993) [Astron. Rep. **37** (4), 346 (1993)].
18. G. J. Ferland, CLOUDY94 Code. http://www.nublado.org.
19. T. Blocker, Astron. Astrophys. **297**, 727 (1995).
20. T. Blocker, Astron. Astrophys. **299**, 755 (1995).
21. R. E. S. Clegg and D. Middlemass, Mon. Not. R. Astron. Soc. **229**, 759 (1987).
22. N. V. Havrilova and O. V. Rokach, Visn. Astron. Shkol. Molod. Vchenikh **2** (1), 82 (2001).
23. V. V. Golovatyi and Yu. F. Mal'kov, Astron. Zh. **69** (6), 1166 (1992) [Sov. Astron. **36** (6), 599 (1992)].
24. D. E. Osterbrock and E. Flather, Astrophys. J. **129**, 26 (1959).
25. N. V. Havrilova and N. L. Tishko, Visn. Astron. Shkol. Molod. Vchenikh **1** (2), 115 (2000).
26. V. V. Holovatyy, R. E. Gershberg, Yu. F. Mal'kov, *et al.*, Izv. Krymsk. Astrofiz. Obs. **96**, 1 (1999).
27. N. V. Havrilova, V. V. Holovatyy, and B. Ya. Melekh, J. Phys. Studies **6** (4), 451 (2002).
28. V. V. Holovatyy and N. V. Havrylova, J. Phys. Studies **7** (4), 1 (2003).
29. R. A. Benjamin, E. D. Skillman, and D. P. Smits, astro-ph/0202227.
30. N. V. Havrylova, Astron. Astrophys. Trans. **22** (6), 833 (2003).
31. B. Ya. Melekh, Visn. Astron. Shkol. Molod. Vchenikh **1** (2), 111 (2000).
32. Yu. I. Izotov and T. X. Thuan, Astrophys. J. **511**, 639 (1999).
33. D. R. Ballantyne, G. J. Ferland, and P. G. Martin, Astrophys. J. **536**, 773 (2000).
34. B. Ya. Melekh, Visn. Astron. Shkol. Molod. Vchenikh **2** (2), 96 (2001).
35. Yu. F. Mal'kov, Astron. Zh. **74** (6), 853 (1997) [Astron. Rep. **41** (6), 760 (1997)].
36. J. Koppen, A. Acker, and B. Stenholm, Astron. Astrophys. **248**, 197 (1991).
37. A. Alibes, J. Labay, and R. Canal, astro-ph/0107016.

Translated by G. Rudnitskiĭ

Astronomy Reports, Vol. 49, No. 5, 2005, pp. 405–416. Translated from Astronomicheskiĭ Zhurnal, Vol. 82, No. 5, 2005, pp. 453–465.

A Compiled Catalog of Spectroscopically Determined Elemental Abundances for Stars with Accurate Parallaxes; Magnesium

T. V. Borkova and V. A. Marsakov

Rostov State University, Rostov-on-Don, 344104 Russia

Received July 5, 2004; in final form, December 3, 2004

Abstract—We present a compiled catalog of effective temperatures, surface gravities, iron and magnesium abundances, distances, velocity components, and orbital elements for stars in the solar neighborhood. The atmospheric parameters and iron abundances are averages of published values derived from model synthetic spectra for a total of about 2000 values in 80 publications. Our relative magnesium abundances were found from 1412 values in 31 publications for 876 dwarfs and subgiants using a three-step iterative averaging procedure, with weights assigned to each source of data as well as to each individual determination, and taking into account systematic deviations of each scale relative to the reduced mean scale. The estimated completeness for data sources containing more than five stars up to late December 2003 exceeds 90%. For the vast majority of stars in the catalog, the spatial-velocity components were derived from modern high-precision astrometric observations and their Galactic orbital elements were computed using a three-component model of the Galaxy, consisting of a disk, a bulge, and a massive extended halo.

1. INTRODUCTION

Detailed studies of the abundances of several elements in stars of various ages can be used to trace the Galaxy's chemical evolution and identify the sources in which various elements are synthesized, enabling progress in our understanding of the history of star formation and the origin of our Galaxy's multi-component structure. According to current ideas, at least four subsystems can be identified in the Galaxy: the thin disk, thick disk, proto-disk halo, and accreted halo. It is believed that the first three subsystems formed from the same collapsing proto-galactic cloud, whereas the last subsystem was formed of isolated proto-galactic fragments and the debris of dwarf satellite galaxies that were disrupted and captured by the Galaxy at various stages of its evolution. (For more detail on the presence of accreted-halo stars in the solar vicinity, see [1] and references therein.) Since the vast majority of stars in the solar neighborhood are members of the thin-disk and thick-disk subsystems, the chemical compositions of these subsystems are best known. One striking result is that the thin-disk stars clearly exhibit a decrease in their relative abundances of α-process elements, [α/Fe], with increasing metallicity, [Fe/H]. This means that the rate of iron enrichment of the interstellar medium during the thin-disk formation stage was greater than the rate of enrichment in α-process elements. In addition, there is a strong difference between the thick-disk and thin-disk subsystems in their relative abundances of α-process elements, testifying that the transition between the two disks was discrete (see, for instance, [2–5]). Another interesting result is the absence of appreciable differences in the [α/Fe] ratios for proto-disk halo and thick-disk stars. This can be interpreted as evidence that these two systems were formed during a time so short that close binaries with component masses of $4–8\,M_\odot$ did not have time to evolve, explode as type Ia supernovae, and enrich the interstellar medium with iron-peak elements. The large scatter in the relative abundances of α-process elements in the halo is interpreted as evidence that mixing in the interstellar medium was weak during the formation of the halo subsystem (see, for instance, [5]). The closeness of the ages of the stars in these two subsystems has even led some authors to doubt the existence of two separate subsystems, and to suggest that the thick disk and proto-disk halo should be combined into a single subsystem [6, 7]. Note, however, that these conclusions are based on very limited samples, with possible selection effects due to the extreme kinematic criteria used to isolate stars belonging to each of the subsystems. In fact, a more careful study of the relative abundances of α-process elements for thick-disk stars revealed a slight decrease of [α/Fe] with increasing metallicity, considered to be evidence for the onset of enrichment of the interstellar medium with iron by type Ia supernovae [8]. This means that the formation of the thick disk began more than ≈1 billion years after the first burst of star formation in the collapsing proto-

1063-7729/05/4905-0405$26.00

Galactic cloud. It was also found that a large number of stars with ratios $[\alpha/\mathrm{Fe}] \leq 0.25$ dex are observed in the range $[\mathrm{Fe/H}] \approx -1.0 \ldots -1.5$ dex, which is more characteristic of thin-disk stars (see, for example, [9]). In addition, most stars with unusually low abundances of α-process elements have retrograde orbits and so were probably captured from dwarf satellite galaxies. This hypothesis is supported by the results of Shetrone *et al.* [10] and Tolstou *et al.* [11], who showed that stars with low $[\alpha/\mathrm{Fe}]$ values are actually observed in dwarf spheroidal galaxies.

As we noted, the results cited above were obtained from fairly limited samples, which were often influenced by significant kinematic selection effects, and so require additional verification. The abundances of a number of elements have been published for numerous stars in the solar neighborhood. These were derived by different groups and have different accuracies. The best-studied α-process element is magnesium: unevolved F–G stars possess optical lines of this element with various intensities produced by atoms in various excited states. Accordingly, the aim of our study is to compile a uniform master catalog of relative magnesium abundances for solar-vicinity stars reduced to a unified scale using essentially all published data, along with computed spatial-velocity components and Galactic orbital elements based on accurate trigonometric parallaxes, proper motions, and radial velocities. This catalog will make it possible to extract samples in order to study various subsystems, not only with considerably larger volumes, but also largely free of artificial selection effects. Later, we will use these data together with theoretical evolutionary tracks to determine the ages of stars that have begun to leave the main sequence, taking into account the abundances of their α-process elements. The high-accuracy kinematic data of our compiled catalog will make it possible to reliably assign stars to particular subsystems of the Galaxy, and enable comprehensive statistical analyses of the stellar populations' chemical, physical, spatial, and kinematic properties. At the same time, homogeneous data on the relative magnesium abundances of stars currently in the solar vicinity but born at various distances from the Galactic center can be used to reconstruct the star-formation history and the evolution of the interstellar medium's chemical composition during the early stages of the formation of our Galaxy.

2. PREPARATION OF THE COMPILED CATALOG

The various published abundances of an element for a given star often differ quite appreciably, even when the spectra reduced by different authors are of similarly high quality. Extraction of the needed information from the spectra is based solely on current ideas concerning the structure of stellar atmospheres, and these ideas develop via the usual iterative process. It is therefore not surprising that different authors have preferred to use somewhat different theoretical model stellar atmospheres and develop different techniques for reducing and theoretically analyzing spectra. In several leading groups, analyses of spectral-line formation have been carried out without assuming local thermodynamic equilibrium. In fact, it is always necessary to analyze non-LTE effects for any abundance determinations. However, the assumption of LTE is justified for the atmospheres of dwarfs due to their high densities of particles, whose collisions bring the atomic-level populations into equilibrium. In particular, detailed computations have demonstrated that non-LTE corrections for magnesium in F–G dwarfs and subgiants are small, within 0.1 dex, and thus are smaller than the internal uncertainties in the Mg abundances [12]. To avoid uncertainties due to non-LTE effects for lines of iron, we always use abundances derived solely from FeII lines. (Note that, in his determinations of relative stellar magnesium abundances assuming LTE, Fuhrmann [4, 5] used lines of neutral elements for which the non-LTE effects are approximately the same, and his resulting [MgI/FeI] ratios are nearly unbiased.)

These factors explain the reasons for the deviations among the data obtained and analyzed by different authors. We also cannot rule out the possibility of systematic differences between the magnesium abundances presented in different papers. If several abundance values are available for the same star, they can simply be averaged. However, when an abundance is presented in only one paper, the possibility of systematic differences must be considered. We collected all available lists (with $\geq$5 stars) of relative magnesium abundance estimates, [Mg/Fe], for field stars from high-resolution spectra with high signal-to-noise ratios published after 1989. We estimate the completeness of the abundances published for solar-vicinity stars up through December 2003 to be better than 90%. The largest of the source catalogs contain only about 200 stars (Table 1). Note that our aim is not to analyze the origin of discrepancies among the data, but to compile a list of published spectroscopic relative magnesium abundances for field stars that is as complete as possible, and is reduced to a uniform scale. The raw material for this study were 36 publications containing 1809 magnesium-abundance determinations for 1027 stars. Of these stars, we retained only 876 dwarf and subdwarf stars that lie below the solid line in the Hertzsprung–Russell diagram in Fig. 1a. This line was plotted "by eye," parallel to the zero-age main sequence, to exclude stars in more

Table 1. Weights, p_j, and systematic deviations, $\Delta[\mathrm{Mg/Fe}]_j$, derived for each of the lists in two metallicity ranges

Source	Total number of stars	[Fe/H] ≤ –1.0			[Fe/H] > –1.0		
		$\Delta[\mathrm{Mg/Fe}]_j$	p_j	Number of stars	$\Delta[\mathrm{Mg/Fe}]_j$	p_j	Number of stars
[13]	178	–	–	–	−0.045	1.00	167
[9]	30	+0.001	1.00	7	+0.046	0.60	22
[14]	61	−0.056	0.64	27	−0.026	0.63	32
[15]	15	+0.034	1.00	13	−0.069	0.63	2
[4, 5]	111	−0.040	0.52	6	+0.006	0.81	76
[16]	52	+0.053	0.60	20	+0.053	0.63	22
[17, 18]	93	–	–	–	−0.011	0.64	59
[19, 20]	209	+0.070	0.67	21	+0.004	0.69	77
[21]	16	−0.0035	0.61	7	+0.041	0.49	7
[22]	9	–	–	–	+0.008	0.70	5
[23]	8	−0.030	0.96	7	–	–	–
[24–26]	51	−0.019	0.57	16	+0.011	0.46	21
[27]	20	−0.111	0.43	20	–	–	–
[28]	20	–	–	–	+0.017	1.00	20
[29, 30]	55	−0.082	0.28	8	–	–	–
[31]	7	−0.050	0.63	7	–	–	–
[32]	217	+0.129	0.40	40	+0.052	0.80	176
[8]	10	–	–	–	+0.040	1.00	8
[33]	65	–	–	–	−0.002	0.66	27
[34]	20	+0.098	0.33	11	−0.080	0.76	4
[35, 36]	27	−0.030	0.33	9	–	–	–
[37]	142	−0.077	0.67	41	−0.076	0.77	53
[38]	176	–	–	–	+0.046	0.90	30

Note: The "Number of stars" columns give the number of a list's stars that are also present in other sources.

advanced evolutionary stages. This automatically rejected five publications in which only giants had been studied.

Atmospheric Parameters and Iron Abundances

We simply averaged the stellar effective temperatures and surface gravities from the cited papers, in which these parameters were determined using various methods. For both parameters, we estimated the uncertainties of the averages based on the scatter of the individual values about the average for each star; i.e., from the agreement of the values obtained by the various authors. For this purpose, we calculated the deviations $dX_i = \langle X \rangle - X_i$ for stars for which these parameters were determined in several studies, where the index i refers to the individual measurements for a given star. Note that our uncertainty estimates are based on as many as 80 publications, since we also used studies devoted to spectroscopic abundance determinations for other elements (see the numbers of stars in the histograms, Fig. 2). We then plotted the corresponding distributions and calculated the dispersions of Gaussian curves describing them, which were equal to $\epsilon(T_{\mathrm{eff}}) = \pm 56$ K and ± 82 K and $\epsilon(\log g) = \pm 0.12$ and ± 0.24 for stars with [Fe/H] values above and below -1.0, respectively. The good agreement of the observed distributions with the Gaussian curves shows that the deviations are random, so that their dispersions should reflect the

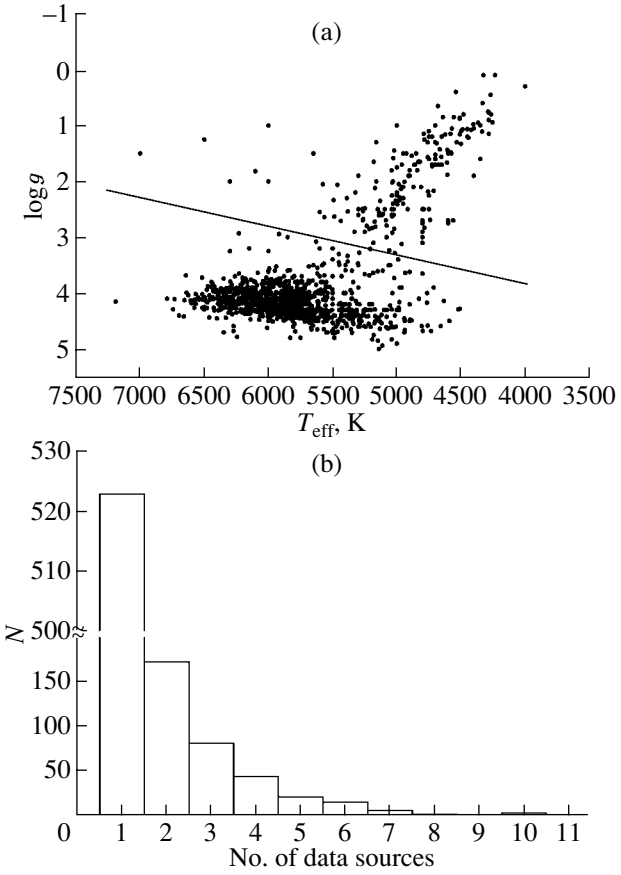

Fig. 1. (a) $T_{\rm eff} - \log g$ diagram for stars with magnesium abundances found in the literature and (b) the distribution of the number of magnesium-abundance determinations available for the stars. Only stars lying below the sloping line in diagram (a) enter our catalog.

actual uncertainties in the parameters. Our [Fe/H] values for each star are also averages of metallicities from the same papers, with uncertainties estimated as $\epsilon([{\rm Fe/H}]) = \pm 0.07$ dex and ± 0.13 dex, respectively, for metal-rich and metal-poor stars. All these estimates are close to the lower limits of the uncertainties for these parameters claimed by the authors. These distributions and the approximating normal curves are displayed in Fig. 2. We found it necessary to differentiate between the two metallicity groups because the uncertainties in all the parameters are considerably larger for the metal-poor stars.

Iterative Procedure Used to Calculate the Relative Magnesium Abundances

To get an idea of the number of magnesium-abundance determinations for the individual stars, see the histogram in Fig. 1b, which presents the distribution of the number of sources for the stars. This histogram shows that the number of stars decreases exponentially with increasing number of magnesium-abundance determinations, so that only single determinations are available for more than half the stars in the sample. To derive reliable abundances, we applied a somewhat modified version of the three-step iterative technique for compiling data presented by Castro *et al.* [39].

Figure 3 presents several diagrams that compare the [Mg/Fe] ratios for the lists having the largest numbers of stars in common. We can see that the values of all the authors are fairly well correlated, with all the correlation coefficients being $r \geq 0.8$. However, small (within the uncertainties) systematic deviations are present in the data. Not only are the results of the LTE and non-LTE approximations different, but there exist discrepancies within each of these approximations. In particular, the two diagrams in the upper panel of Fig. 3 demonstrate the scatter of the estimates obtained using a single approximation. The two diagrams in the middle panel, which compare the abundances derived using different approximations, show only scatter without a considerable systematic offset. On the other hand, appreciable systematic differences can appear not only between the values obtained using different approximations, but also between the values obtained by different authors using the same approach (Figs. 3e and 3f). If there are no regular systematic differences related to a particular approach, we can simply average all these data for each star.

After averaging (calculating the individual preliminary mean values, $\langle[{\rm Mg/Fe}]_i\rangle$), we can check whether the systematic differences and scatter of the $[{\rm Mg/Fe}]_i$ values for different authors depend on metallicity. Figure 4 shows the relations between the deviations $\delta[{\rm Mg/Fe}]_i = \langle[{\rm Mg/Fe}]_i\rangle - [{\rm Mg/Fe}]_i$ and $[{\rm Fe/H}]_i$ for some of our lists. The subscript i here refers to an individual abundance determination for a star. The diagrams demonstrate that the scatter of the deviations and the systematic offset of $\delta[{\rm Mg/Fe}]_i$ relative to the mean (zero) vary from list to list and also depend on metallicity. Sometimes the scatter and systematic offset remain practically the same over the whole metallicity range (Figs. 4a and 4b). Weak trends with various signs are common. The $\delta[{\rm Mg/Fe}]_i$ deviations sometimes move upwards (Figs. 4c and 4d) and sometimes downwards (Figs. 4e and 4f) with increasing metallicity in the diagram. To take these small but systematic trends into account, we divided each list into two metallicity ranges at $[{\rm Fe/H}] = -1.0$ dex and calculated the mean deviations for these ranges; i.e., the systematic deviations $\Delta[{\rm Mg/Fe}]_j = \langle\delta[{\rm Mg/Fe}]\rangle_j$ (see the dotted lines in the diagrams). We then corrected all the individual $[{\rm Mg/Fe}]_i$ values for these biases. As noted above, these corrections leave the magnesium abundances

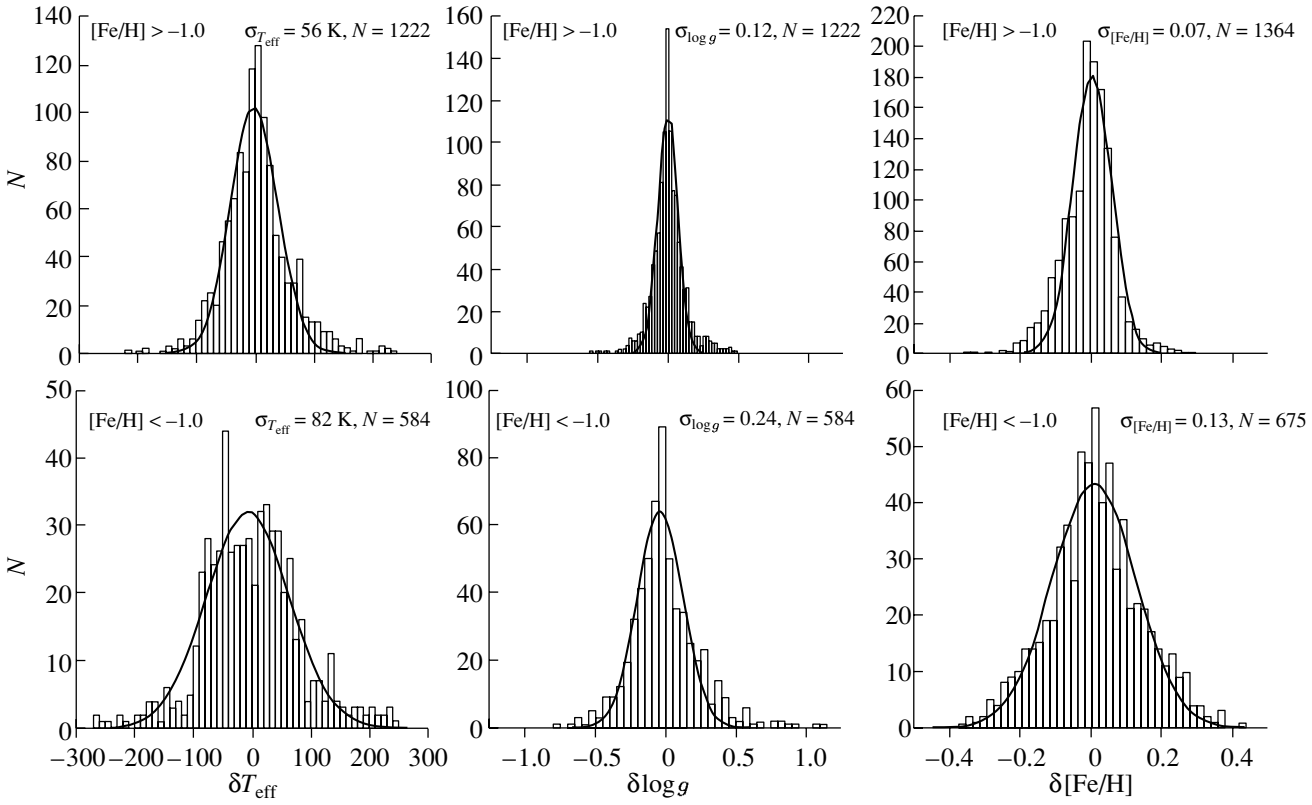

Fig. 2. Distribution of the deviations of individual determinations of $T_{\rm eff}$, $\log g$, and [Fe/H] from the computed mean values. The upper row of the graphs is for stars with [Fe/H] > -0.1, and the lower row, for those with [Fe/H] < -1.0. The curves represent normal approximations to the distributions. The dispersions and numbers of stars are indicated for the histograms.

for stars present in several lists virtually unchanged. However, if a star's magnesium abundance was determined in a single study only, the correction will strongly affect the final magnesium abundance. Indirect confirmation that it is appropriate to correct for these systematic differences is provided by the fact that the scatter of the data points in the final [Fe/H]–[Mg/Fe] diagram plotted for the sample stars became considerably smaller after applying the corrections, and characteristic features observed in the data for individual sources became more prominent (compare Fig. 10 below and Fig. 6 in [15]).

The next step after correcting for systematic biases was to determine weights for the data sources in the lists and calculate new weighted means. Figures 3 and 4 show that the scatters in the diagrams—i.e., the [Mg/Fe] uncertainties in the lists—are not all the same. Accordingly, each list was assigned a weight that was inversely proportional to the corresponding dispersion for the deviations in each of the metallicity ranges. The lowest scatter for the higher metallicities was found for the lists of [8, 13, 28], and they were assigned unit weights. At lower metallicities, the lowest scatter was shown by the lists of [9, 15]. The lowest weights assigned to some of the lists were ≈ 0.3. The weights and biases for each list in each of the two metallicity ranges are collected in Table 1. We then calculated a new weighted mean magnesium abundance for each star, taking into account the biases and weights assigned to the lists.

Let us briefly discuss one important aspect of compiling the data. In practice, small catalogs can have few stars in common even with the largest original catalogs. Thus, to analyze the agreement between their values and the values of other authors and assign them correct weights, we combined the small catalogs into larger lists, each containing a series of studies by the same group in which the same techniques were used to derive the abundances. For lists containing several values for the same star, we chose the more recent values. As a result, we obtained 24 lists including 31 primary data sources (Table 2[1]). Further, all the lists were used to calculate preliminary mean magnesium abundances for each star in the sample. (The only exception was [40]: none of its nine stars were found in any other source, and

[1] Table 2 of this paper is presented only electronically and can be found at http://cdsweb.u-strasbg.fr/cats/J.AZh.htx. A description of this table is given in the Appendix.

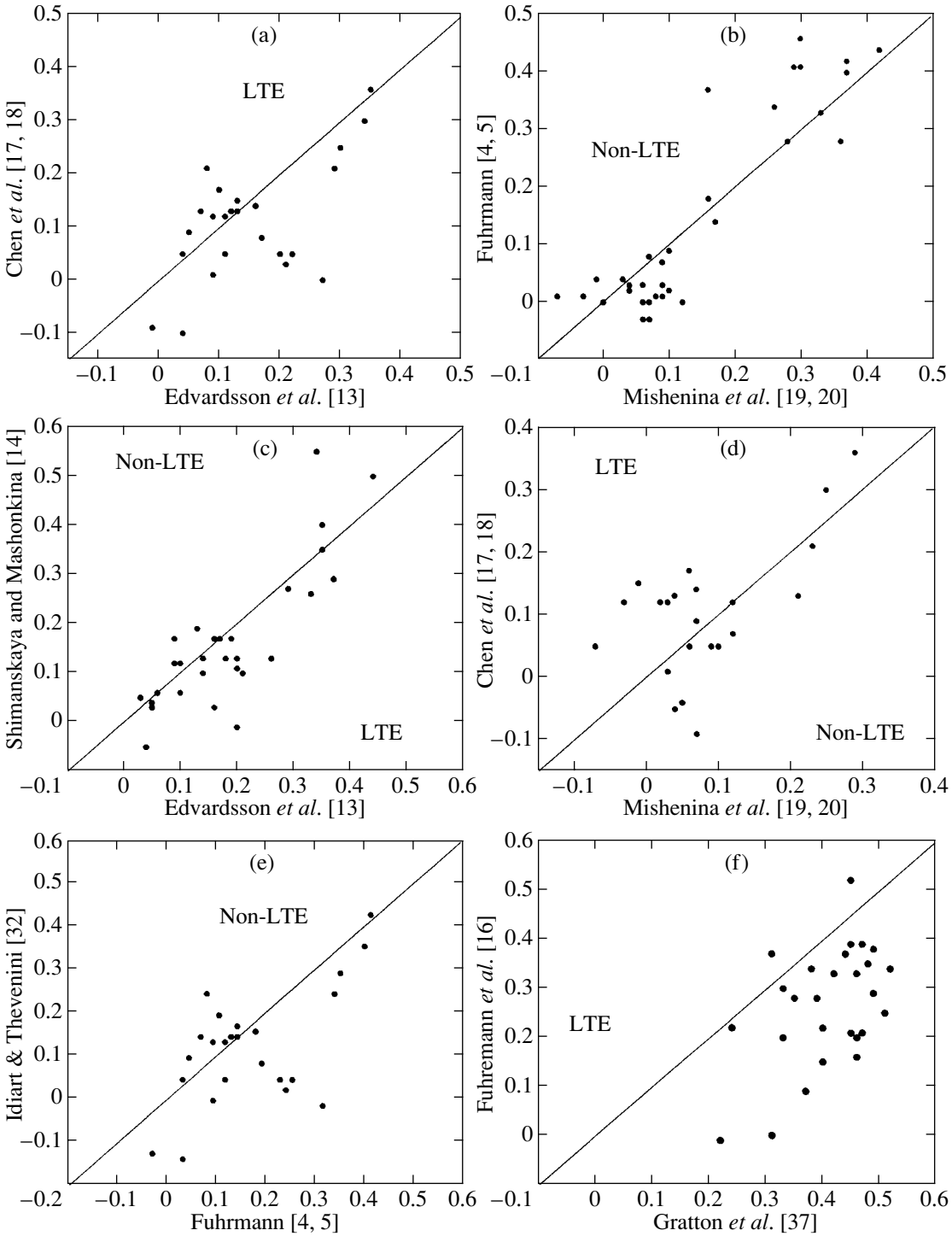

Fig. 3. Comparison of [Mg/Fe] values from several authors. The approximations used by the authors when deriving the magnesium-abundance determinations are indicated.

all the data for these stars were entered into the final catalog without any changes.)

The next step was also a weight-assigning procedure, this time for individual values, $[\mathrm{Mg/Fe}]_{ij}$, where the first subscript refers to the value and the second to the list. This procedure was intended to assign lower weights to initial values showing larger deviations. Clearly, such a procedure can work only if there are three or more values for the same star. This step makes use of the deviations from the calculated weighted means, δ_{ij}, for individual values (with their biases taken into account). When assigning the

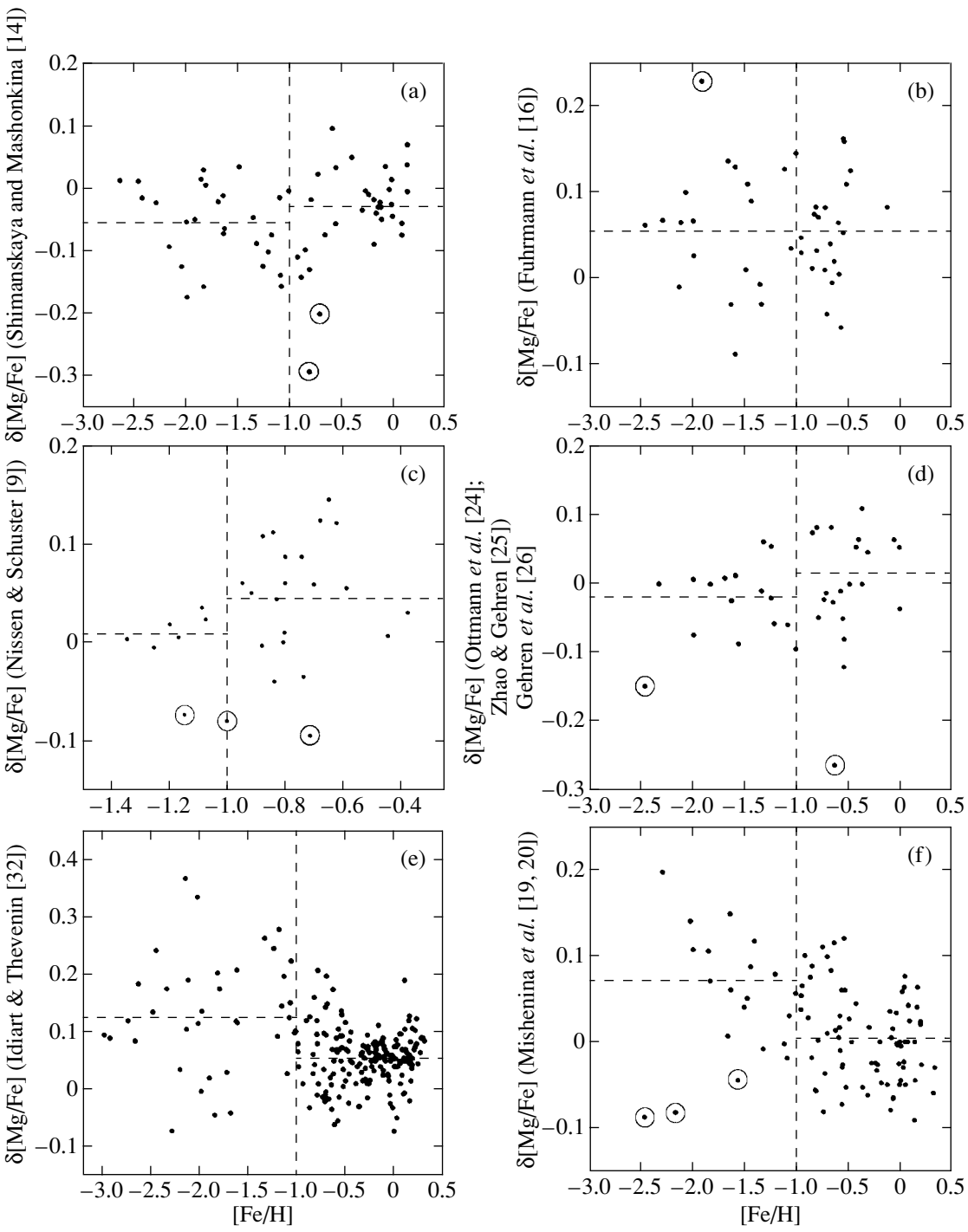

Fig. 4. Relation between the metallicities and the deviations of individual magnesium-abundance determinations (from several sources) from the averages calculated using the data of all authors, (δ[Mg/Fe]). The values rejected by applying a 3σ criterion to the scatter ($\sigma_{\delta[\mathrm{Mg/Fe}]}$) or by the calculated deviations ($\Delta[\mathrm{Mg/Fe}]_j$) are circled. The horizontal lines are mean deviations for each of the ranges.

weights p_{ij}, we considered the mean absolute value, ε_j, of the deviations for all stars in the list containing the given value. The weights were calculated using the formula $p_{ij} = \sqrt{2\varepsilon_j^2/(\delta_{ij}^2 + \varepsilon_j^2)}$. We can see that an individual weight of unity was assigned to values whose deviations were equal to the mean deviation. Most stars in the list were given weights slightly greater than unity, $(p_{ij})_{\max} = \sqrt{2}$. However, the weights begin to decrease appreciably for $\delta_{ij} > \varepsilon_j$.

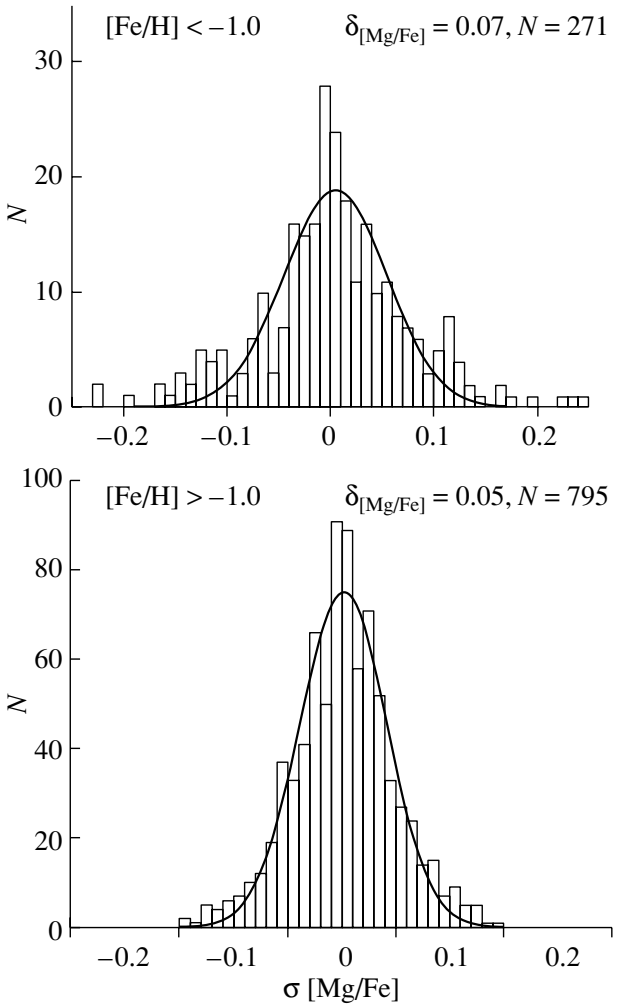

Fig. 5. Distributions of the δ[Mg/Fe] deviations for the two metallicity ranges. The notation is as in Fig. 2.

As a result, this procedure assigns the lowest weights to the least-reliable determinations and enables us to obtain final values that are close to those given for most of the sources, with no single measurement rejected. Some idea of the internal accuracy of our final [Mg/Fe] values can be obtained from the dispersion of the distribution of all the deviations δ_{ij}, equal to $\epsilon_{[\mathrm{Mg/Fe}]} = \pm 0.05$ dex and ± 0.07 dex for metal-rich and metal-poor stars, respectively (Fig. 5). The final weighted mean [Mg/Fe] values calculated for our sample of dwarfs and subgiants in the solar neighborhood are presented in Table 2 (see the Appendix).

Distances, Proper Motions, and Radial Velocities

We determined the distances to the stars using trigonometric parallaxes with uncertainties below 25% from the catalogs [41–43] or, in their absence, we adopted the photometric distances from the catalogs [44, 45], derived using *uvby* β photometric data. The uncertainty in photometric distances is usually claimed to be $\pm 13\%$ [45]. Figure 6 shows the distribution of the distances of the sample stars from the Sun. The distribution's ascending branch lasts only to 25 pc, after which a steep decline begins, testifying that most of the sample stars are close to the Sun. The photometric distances were used only for the most distant stars.

We took the proper motions from the catalogs [41–44, 46, 47] (our order of preference of the catalogs, which corresponds to the accuracy of their proper motions, was 41–42–43–46–44–47). For most stars in our sample, the typical uncertainties in their proper motions are ≈ 1.8 milliarcseconds/year, corresponding to a mean uncertainty in the tangential velocity of $\approx \pm 0.8$ km/s.

We took the radial velocities from the catalogs [45, 48–50] (in the order of preference 48–49–50–45). If the required data were not present in any of these catalogs, we took them from other publications (see references to Table 2 in the Appendix). The characteristic uncertainties in the radial-velocity measurements for the sample stars are $\approx \pm 0.6$ km/s [43].

Spatial Velocities and Galactic Orbital Elements

We computed the U, V, and W components of the total spatial velocity relative to the Sun for 850 stars with distances, proper motions, and radial velocities (U is directed toward the Galactic anticenter, V in the direction of the Galactic rotation, and W toward the North Galactic pole). The main contribution to the uncertainties in the spatial velocities comes from the uncertainties in the distances, rather than the uncertainties in the tangential and radial velocities. For mean distance uncertainties of 15% and the mean distance from the Sun of the sample stars, ≈ 60 pc, the mean uncertainty in the spatial-velocity components is $\approx \pm 2$ km/s.

We adopted a Galactocentric distance for the Sun of 8.5 kpc, a rotational velocity for the Galaxy at the solar Galactocentric distance of 220 km/s, and a velocity for the Sun relative to the local centroid of $(U_\odot, V_\odot, W_\odot) = (-11, 14, 7.5)$ km/s [51]. We used these values to calculate the components of the spatial velocities in cylindrical coordinates, (Θ, Π, W), and the total residual velocities of the stars relative to the local solar centroid, V_{res}.

We calculated the Galactic orbital elements by modeling 30 orbits of each star around the Galactic center using the multicomponent model for the Galaxy of [52], which consists of a disk, bulge, and extended massive halo.

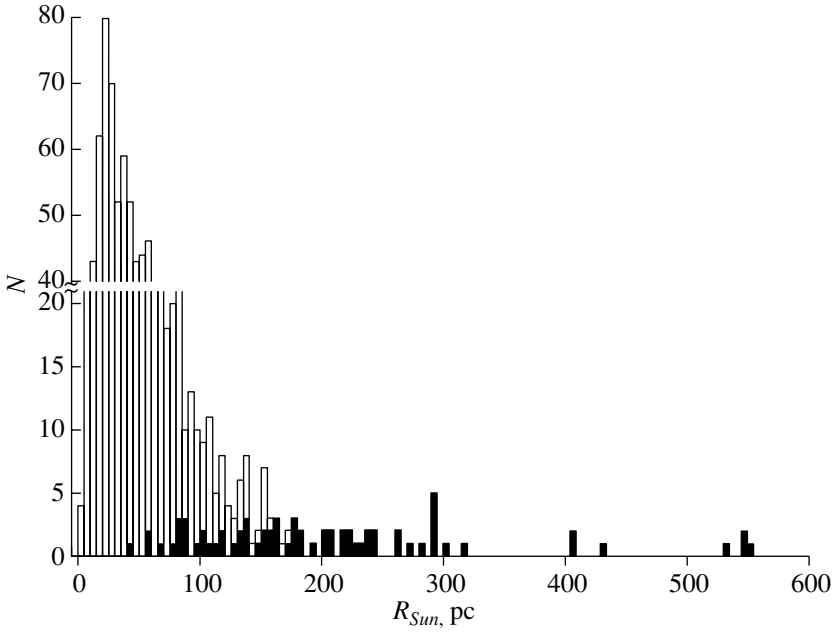

Fig. 6. Distribution of the distances of the catalog stars from the Sun derived from trigonometric parallaxes (open bars) and photometric measurements (filled bars).

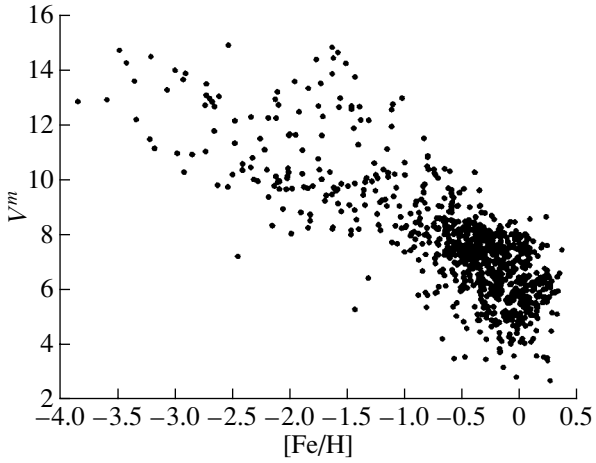

Fig. 7. Metallicity versus apparent magnitude.

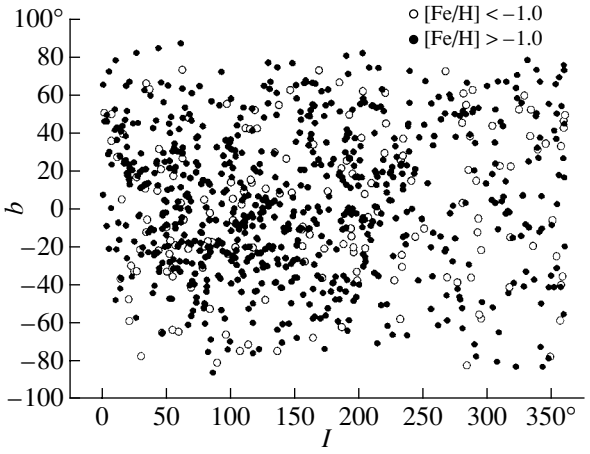

Fig. 8. Positions of metal-rich (filled circles) and metal-poor (open circles) stars on the sky.

A list of the stars with all the parameters described in this paper is presented in Table 2 (see its description in the Appendix). The catalog itself is published only electronically, at the address http://cdsweb.u-strasbg.fr/cats/J.AZh.htx.

3. ANALYSIS OF THE SAMPLE

All the published catalogs can be tentatively subdivided into two groups based on the principle applied to select stars for spectroscopic determinations of the abundances of various elements. The first group consists of various samples whose stars were selected based on a limiting apparent magnitude. Since the Sun is situated near the Galactic plane, such samples contain almost exclusively stars of the disk subsystems, with very few halo (i.e., low-metallicity) stars. Thus, a preliminary selection of low-metallicity stars using photometric data is needed for spectroscopic observations of objects in the halo subsystems. The apparent magnitudes of the stars selected in this way are much fainter. This is clearly illustrated in the [Fe/H]–V_m diagram for our sample stars (Fig. 7).

Nearly all the stars with [Fe/H] ≥ -1.0 are brighter than $V \approx 9^m$, whereas most of the more

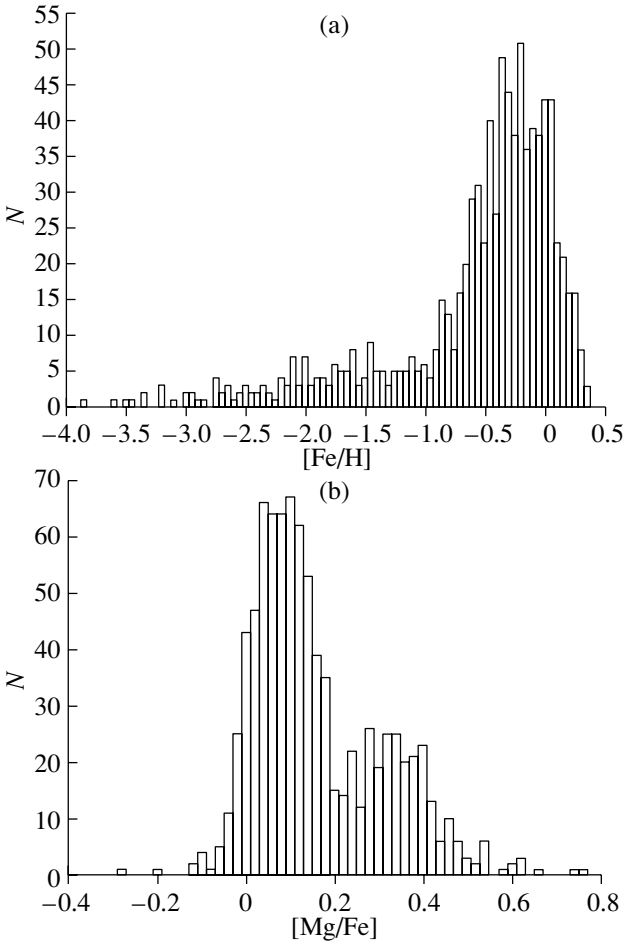

Fig. 9. Distributions of the (a) iron abundances and (b) relative magnesium abundances of the catalog stars.

metal-poor stars are fainter. The stars of both groups cover the sky rather uniformly, with an understandable concentration of metal-richer stars toward the Galactic plane (Fig. 8). This observational selection effect should be borne in mind when estimating the relative numbers of stars of various metallicities in the solar neighborhood. Figure 9 displays the [Fe/H] and [Mg/Fe] distributions for the resulting sample, while Fig. 10 shows the corresponding [Fe/H]–[Mg/Fe] diagram.

We are preparing a cycle of papers in which we identify stars belonging to the thin-disk and thick-disk subsystems, as well as to the proto-disk and "accreted" halo subsystems, based on the elements of the Galactic orbits from the catalog. In these forthcoming papers, we will estimate the star-formation rates and efficiencies of mixing of the interstellar medium during the early stages of the Galaxy's evolution based on an analysis of the scatter of the relative magnesium abundances for low-metallicity stars of the old Galactic subsystems.

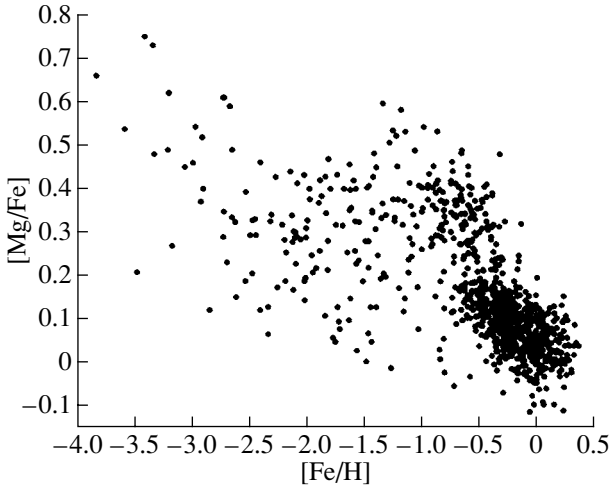

Fig. 10. Metallicity versus magnesium abundance for the catalog stars.

We are also planning to present similarly unified abundance determinations for other α-process elements in a future version of our catalog.

ACKNOWLEDGMENTS

The authors are grateful to L.I. Mashonkina for fruitful discussions of the results.

APPENDIX

Description of Table 2 (this table is published only electronically, at the address http://cdsweb.u-strasbg.fr/cats/J.AZh.htx):

(1) HD: No. in the HD catalog ⟨ III/135 ⟩
(2) DM: DM number ⟨I/119⟩, ⟨I/122⟩
(3) HIP: No. in the Hipparcos catalog (⟨I/239⟩)
(4) SAO: No. in the SAO catalog ⟨I/131⟩
(5) OtherName: Other name
(6) Vmag: Apparent V magnitude in the Johnson system
(6) Radeg: α in degrees (ICRS, epoch J1991.25)
(7) Dedeg: δ in degrees (ICRS, epoch J1991.25)
(8) Plx: Trigonometric or photometric parallax

Remark on column 8:

Errors are given for trigonometric parallaxes only.

(9) pmRA: Proper motion, $\mu_\alpha \cos\delta$
(10) pmDE: Proper motion, μ_δ
(11) e_Plx: Standard error of the trigonometric parallax
(12) e_pmRA: Standard error of $\mu_\alpha \cos\delta$
(13) e_pmDE: Standard error of μ_δ
(14) f(pi): Data source for the star's parallax and proper motion

Remark on column 14:

The following notation is used for the references:

[HIP]: The Hipparcos and Tycho Catalogues, ESO, 1997

[KHR]: Kharchenko N.V., 2001, All-sky Compiled Catalogue of 2.5 million stars, KFNT, 17, 409

[SKY]: Myers J.R., Sande C.B., Miller A.C., *et al.,* 2002, Sky2000. Catalog, version 4

[BCY]: Beer T.C., Chiba M., Yoshi Y., *et al.,* 2000, Astron J., 119, 2866

[CLL]: Carney B.W., Latham D.W., Laird J.B., Aguilar L.A., 1994, Astron. J., 107, 2240

[BSN]: Bakos G.A., Sahu K.C., Nemeth P., 2002, Astrophys. J., Suppl. Ser. JS, 141, 187.

(15) RV: Radial velocity

(16) f(vr): Data source for the radial velocity (3)

Remark on column 16:

The following notation is used for the references:

[BBF]: Barbier-Brossat M. and Figon P., Astron. Astrophys. 142, 217, 2000

[BG]: Barberi M. and Gratton R.G., Astron. Astrophys., 384, 879, 2002

[MLG]: Malaroda S., Levato H., Galliani S., Stellar Radial Velocities 1991–1998

[NMB]: Nidever D.L., Marcy G.W., Butler R.P., *et al.,* Astron. J., Suppl. Ser., 141, 503 (2002)

[NMA]: Nordstrom B., Mayor M., Andersen J., *et al.,* Astron. Astrophys., 418, 989 (2004)

[MON]: Montes D., Lopez-Santiago J., Galvez M.C., *et al.,* Mon. Not. R. Astron. Soc., 328, 45 (2001)

[FUL]: Fulbright J.P., Astron. J., 123, 404 (2002)

[WBS]: Wilhelm R., Beers T.C., Sommer-Larsen J., *et al.,* Astron. J., 117, 1229 (1999)

[SWG]: Strassmeier K.G., Washuettl A., Granzer T., *et al.,* Astron. Astrophys., Suppl. Ser., 142, 275 (2000)

[LST]: Latham D.W., Stefanik R.P., Torres G., *et al.,* Astron. J., 124, 1144 (2002)

[NS]: Nissen P.E., Schuster W.J. Astron. Astrophys., 326, 751 (1997)

[GBR]: Grenier S., Baylac M.O., Rolland L., *et al.,* Astron. Astrophys., Suppl. Ser., 137, 451 (1999)

[AFG]: Axer M., Fuhrmann K., Gehren T., Astron. and Astrophys., 300, 751 (1995).

(17) Teff: Effective temperature

(18) log g: The star's surface gravity

(19) [Fe/H]: The star's iron abundance (4)

(20) [Mg/Fe]: The star's magnesium-to-iron abundance

Remark on columns 19, 20:

Elemental abundances are given on a logarithmic scale in solar units.

(21) f(mg): Number of data sources for [Mg/Fe]

(22) f(sum): The data sources' combined weight

Remark for column 22:

The combined weight includes the weights of the data source (Table 1) and of the individual value (see the text).

(23) l: Galactic longitude

(24) b: Galactic latitude

(25) Mv: Absolute magnitude

(26) rsun: Distance from the Sun

(27–29) Xg, Yg, Zg: Coordinates in the Galactic coordinate system

(30) R: Distance to the star from the Galactic center

(31–33) U, V, W: The star's spatial-velocity components (see the text)

(34, 35) Vpi, Vtet: Components of the spatial velocity in the cylindrical coordinate system

(36) Vtot: The star's total residual velocity relative to the local solar centroid

(37–39) Rpe, Rap, e: The star's perigalactic and apogalactic distances and the eccentricity of its Galactic orbit

(40) i: Inclination of the star's Galactic orbit

(41) Zmax: Maximum distance of the star's orbit from the Galactic plane.

REFERENCES

1. T. V. Borkova and V. A. Marsakov, Pis'ma Astron. Zh. **30**, 173 (2004) [Astron. Lett. **30**, 148 (2004)].
2. R. G. Gratton, E. Carretta, F. Matteuchi, and C. Sneden, in *Formation of the Galactic Halo Inside and Out*, Ed. by H. Morrison and A. Sarajedini (Astron. Soc. Pacif., San Francisco, 1996), ASP Conf. Ser., Vol. 92, p. 307.
3. R. G. Gratton, E. Carretta, F. Matteucci, and C. Sneden, Astron. Astrophys. **358**, 671 (2000).
4. K. Fuhrmann, Astron. Astrophys. **338**, 161 (1998).
5. K. Fuhrmann, Preprint (Munich, 2000).
6. K. Fuhrmann, New Astron. **7**, 161 (2002).
7. R. G. Gratton, E. Carretta, S. Desidera, *et al.*, Astron. Astrophys. **406**, 131 (2003).
8. J. Prochaska, S. O. Naumov, B. W. Carney, *et al.*, Astron. J. **120**, 2513 (2000).
9. P. E. Nissen and W. J. Schuster, Astron. Astrophys. **326**, 751 (1997).
10. M. Shetrone, K. A. Venn, E. Tolstou, *et al.*, Astron. J. **125**, 684 (2003).
11. E. Tolstou, K. A. Venn, M. Shetrone, *et al.*, Astron. J. **125**, 707 (2003).
12. N. N. Shimanskaya, L. I. Mashonkina, and N. A. Sakhibullin, Astron. Zh. **77**, 599 (2000) [Astron. Rep. **44**, 530 (2000)].

13. B. Edvardsson, J. Andersen, B. Gustafsson, *et al.*, Astron. Astrophys. **275**, 101 (1993).
14. N. N. Shimanskaya and L. I. Mashonkina, Astron. Zh. **78**, 122 (2001) [Astron. Rep. **45**, 100 (2001)].
15. L. Mashonkina, T. Gehren, C. Travaglio, and T. Borkova, Astron. Astrophys. **397**, 275 (2003).
16. K. Fuhrmann, M. Axer, and T. Gehren, Astron. Astrophys. **301**, 492 (1995).
17. Y. Q. Chen, P. E. Nissen, G. Zhao, *et al.*, Astron. Astrophys., Suppl. Ser. **141**, 491 (2000).
18. Y. Q. Chen, G. Zhao, P. E. Nissen, *et al.*, Astrophys. J. **591**, 925 (2003).
19. T. V. Mishenina and V. V. Kovtyukh, Astron. Astrophys. **370**, 951 (2001).
20. T. V. Mishenina, C. Soubiran, V. V. Kovtyukh, and S. A. Korotin, Astron. Astrophys. **418**, 551 (2004).
21. G. Clementini, R. Gratton, E. Carretta, and C. Sneden, Mon. Not. R. Astron. Soc. **302**, 22 (1999).
22. E. Carretta, R. Gratton, and C. Sneden, Astron. Astrophys. **356**, 238 (2000).
23. P. E. Nissen, B. Gustafsson, B. Edvardsson, and G. Gilmore, Astron. Astrophys. **285**, 440 (1994).
24. R. Ottmann, M. J. Pfeiffer, and T. Gehren, Astron. Astrophys. **338**, 661 (1998).
25. G. Zhao and T. Gehren, Astron. Astrophys. **362**, 1077 (2000).
26. T. Gehren, Y. C. Liang, J. R. Shi, *et al.*, Astron. Astrophys. **413**, 1045 (2004).
27. P. Magain, Astron. Astrophys. **209**, 211 (1989).
28. E. Jehin, P. Magain, C. Neuforge, *et al.*, Astron. Astrophys. **341**, 241 (1999).
29. A. Stephens, Astron. J. **117**, 1771 (1999).
30. A. Stephens and A. M. Boesgaard, Astron. J. **123**, 1647 (2002).
31. B. W. Carney, J. S. Wright, C. Sneden, *et al.*, Astron. J. **114**, 363 (1997).
32. T. Idiart and F. Thevenin, Astrophys. J. **541**, 207 (2000).
33. T. Bensby, S. Filtzing, and I. Lundstrom, Astron. Astrophys. **410**, 527 (2003).
34. S. V. Ermakov, Doctoral Dissertation in Mathematical Physics (SAO, 2002).
35. S. G. Ryan, J. E. Norris, and M. S. Bessell, Astron. J. **102**, 303 (1991).
36. S. G. Ryan, J. E. Norris, and T. C. Beers, Astrophys. J. **471**, 254 (1996).
37. R. Gratton, E. Carretta, R. Claudi, *et al.*, Astron. Astrophys. **404**, 187 (2003).
38. B. E. Reddy, J. Tomkin, L. Lambert, *et al.*, Mon. Not. R. Astron. Soc. **340**, 304 (2003).
39. B. Hauck and M. Mermilliod, Astron. Astrophys., Suppl. Ser. **129**, 431 (1998).
40. S. Castro, R. M. Rich, M. Grenon, *et al.*, Astron. J. **114**, 376 (1997).
41. The Hipparcos and Tycho Catalogues, ESO, 1997.
42. N. V. Kharchenko, All-sky Compiled Catalogue of 2.5 Million Stars, KFNT **17**, 409 (2001).
43. J. R. Myers, C. B. Sande, A. C. Miller, Jr., W. H. Warren, and D. A. Tracewell, Sky2000 Catalog, Version 4 (2002).
44. B. W. Carney, D. W. Latham, J. B. Laird, and L. A. Aguilar, Astron. J. **107**, 2240 (1994).
45. B. Nordstrom, M. Mayor, J. Andersen, *et al.*, Astron. Astrophys. **418**, 989 (2004).
46. T. C. Beers, M. Chiba, Y. Yoshi, *et al.*, Astron. J. **119**, 2866 (2000).
47. G. A. Bakos, K. C. Sahu, and P. Nemeth, Astrophys. J., Suppl. Ser. **141**, 187 (2002).
48. D. L. Nidever, G. W. Marcy, R. P. Butler, *et al.*, Astrophys. J., Suppl. Ser. **141**, 503 (2002).
49. M. Barbier-Brossat and P. Figon, Astron. Astrophys. **142**, 217 (2000).
50. M. Barberi and R. G. Gratton, Astron. Astrophys. **384**, 879 (2002).
51. K. U. Ratnatunga, J. N. Bahcall, and S. Casrtano, Astrophys. J. **291**, 260 (1985).
52. C. Allen and A. Santillan, Rev. Mex. Astron. Astrofis. **22**, 255 (1991).

Translated by N. Samus'

Astronomy Reports, Vol. 49, No. 5, 2005, pp. 417–424. Translated from Astronomicheskiĭ Zhurnal, Vol. 82, No. 5, 2005, pp. 466–473.

Composite Dust Grains: Modeling of Infrared Absorption Bands

T. V. Zinov'eva

Sobolev Astronomical Institute,
St. Petersburg State University, St. Petersburg, Russia

Received February 27, 2004; in final form, December 3, 2004

Abstract—We investigate the influence of small-scale asphericity of the surfaces of dust grains on the characteristics of the two deepest absorption bands observed in the spectra of protostellar objects and stars (the 3.1 μm water-ice and 9.7 μm silicate bands). The model used has composite particles in the form of radially inhomogeneous spheres with intermediate layers in which the index of refraction changes. The observed band widths and the ratios of the optical depths at the band centers can be explained if the grains are composed of small particles consisting of silicate cores with thin ice mantles and rough surfaces. The grain surface roughness considerably broadens the profile of the silicate band.

1. INTRODUCTION

The chemical composition, shape, size, and structure of interstellar dust grains can be estimated by comparing the infrared (IR) absorption bands observed in the spectra of stars and protostellar objects with those predicted by model computations. The profiles, central optical depths, and polarizations of these bands can be studied in this way.

The strongest absorption bands in the near-IR are an ice band at approximately $\lambda_0 = 3.1$ μm (λ_0 is the wavelength at the band center) and a wide silicate band at approximately $\lambda_0 = 9.7$ μm [1]. The $\lambda_0 = 3.1$ band is produced by H_2O-ice, while the $\lambda_0 = 9.7$ band is produced by certain silicates: pyroxenes ($Mg_yFe_{1-y}SiO_3$, where $0 \leq y \leq 1$) or olivines ($Mg_{2y}Fe_{2-2y}SiO_4$). The profiles of the absorption bands vary strongly from object to object. Observations of absorption bands are usually interpreted using models for the absorption of light by dust grains consisting of a refractory core and a volatile envelope. The most common composition adopted for the nucleus is "astronomical silicate" (astrosil)—a hypothetical substance whose inferred optical constants are based on the observed strength and shape of the silicate bands near 9.7 and 18 μm [2].

Lee and Draine [3] used a model (in the Rayleigh approximation) with coated spherical grains with mean radii of 0.1–0.3 μm to interpret the absorption bands of the Becklin–Neugebauer (BN) protostellar object in Orion. They considered a mixture of ice-coated grains with astrosil and graphite cores, and concluded that the ratio of the mantle and core volumes V_{mantle}/V_{core} ranges from 0.5 to 5. The higher value is determined by cosmic elemental abundances, while the lower value is derived from the ratio of the observed polarizations in the 3 μm and 10 μm bands. Henning and Stognienko [4] modeled the observed polarization in the direction of the BN object and GL 2591 using aspherical, porous grains containing silicate, carbon, and vacuum and applying the discrete dipole approximation. Their computations showed that the bands produced by such grains are too wide, and have central absorptions that are stronger than is observed. O'Donnell [5] interpreted observations of the silicate bands in the same objects in terms of scattering by core–mantle spherical grains (in the Rayleigh approximation) with a large aspect ratio ($a/b = 5.0$, where a and b are the semimajor and semiminor axes of the grains). Studies of the influence of grain asphericity on the properties of the 3.1 μm and 9.7 μm bands in many objects have shown that the grains must be significantly aspherical and must have thin mantles [6]. Along with the Rayleigh approximation, exact solutions for scattering by cofocal core–mantle spherical grains obtained via a separation of variables were applied to calculate the optical properties of the grains [7].

All previous studies have considered grains with smooth surfaces. However, the surfaces of interstellar dust grains may have small inhomogeneities (pits or bumps) that result from the evolution of the grains in interstellar clouds or from collisions between grains. It was proposed to take into account the surface roughness for homogeneous spherical particles with nonsmooth surfaces by averaging the deviations from a smooth boundary [8]. This problem has not yet been solved for coated grains. We approach this problem here by applying a model with radially inhomogeneous spheres with intermediate layers. In this model, a grain contains concentric spherical layers

1063-7729/05/4905-0417$26.00

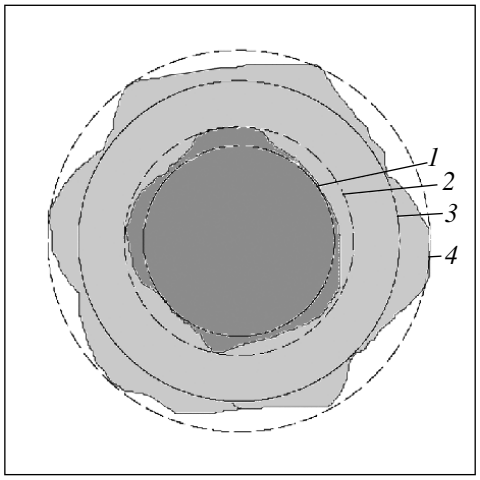

Fig. 1. The structure of an inhomogeneous particle with a mantle. The layers (from center to surface) are (*1*) the homogeneous silicate core, (*1–2*) intermediate layers [transition from silicate to ice], (*2–3*) homogeneous ice mantle, (*3–4*) intermediate layers [transition from ice to outer medium (vacuum)].

with nonvariable optical constants and intermediate layers with variable indices of refraction. It is assumed that the transition between layers is not discontinuous, and occurs along a hyperbolic path.

In the next section, we discuss the model for a radially inhomogeneous grain with intermediate layers. Such a particle scatters light like a layered dust grain with rough and patchy areas on the surface layers modeled in the discrete dipole approximation [9]. We use this model here to interpret infrared absorption bands in the spectra of protostellar sources and stars.

Section 3 considers the influence of the model parameters on the profiles of two absorption bands—the 3.1 μm band of water ice and the 9.7 μm silicate band. In the case of the silicate band, we take into account the possible influence of the nearby 12 μm water-ice absorption band.

Section 4 compares the observed dependences for the absorption bands with the results of the model computations and examines the influence on the details of the band profile of small deviations of the grain-surface shape from sphericity. The last section summarizes our conclusions about the influence of the grain roughness on the profiles of the observed bands.

2. MODEL FOR A RADIALLY INHOMOGENEOUS DUST GRAIN WITH INTERMEDIATE LAYERS

Model grains with smooth surfaces (for both the inner and outer layers) are usually used in studies of cosmic dust, but real grains may have inhomogeneities both on their surfaces and in their interiors. The surface of a dust grain may deviate locally from a strictly spherical shape, i.e., it may display small-scale inhomogeneities. The most common method for calculating the optical constants of particles with inhomogeneities and inclusions is the discrete dipole approximation. This can be applied to grains of arbitrary shape, but it has a serious drawback: the computational time becomes excessively large even for grains that have sizes comparable to the wavelength of the incident radiation.

A solution for scattering on spherical grains with nonsmooth surfaces was obtained by Perelman [10]. Perelman suggested to apply the so-called "generalized Mie theory," based on the diffraction of a plane wave on a sphere with a radially variable continuous index of refraction. This method is based on using a piecewise-hyperbolic approximation for an arbitrary continuous index of refraction. Calculations for a grain model in which the index of refraction decreases along a hyperbola in a narrow layer close to the surface were carried out by Perelman and Zinov'eva [11]. The index of refraction was represented by a continuous function of a size parameter inside an intermediate layer.

In [9], the solution for the scattering of light by a sphere obtained using the piecewise-hyperbolic approximation was generalized to the case of multilayered particles, allowing for the possibility of aspherical layer surfaces (e.g., there are ripples at the surfaces of the core and mantles). Here, we consider spheres with multiple intermediate layers and a single mantle. This model has five parameters: the index of refraction of the core m_{core}, index of refraction of the mantle m_{mantle}, radius of the particle R, fractional volume of the mantle V_{mantle}/V_{total}, and fractional volume of the matter in the intermediate layers $V_{i.l.}/V_{total}$.

The profile of the index of refraction for a radially inhomogeneous, spherically symmetric layered particle has the form

$$m(\rho) = \begin{cases} m_{core}, & 0 \le \rho < r_{core}; \\ \mathcal{M}(\rho), & r_{core} < \rho \le r; \\ m_{mantle}, & r \le \rho < r_{mantle}; \\ \mathcal{M}(\rho), & r_{mantle} < \rho \le R; \\ M, & \rho > R, \end{cases} \qquad (1)$$

where m_{core}, m_{mantle}, and M are the index of refraction of the core, mantle, and medium surrounding the particle, respectively, r_{core} is the radius of the core, r_{mantle} is the radius of the mantle, ρ is the diffraction parameter, r is the distance from the grain center to the mantle, R is the radius of the grain, and $\mathcal{M}(\rho)$ is an arbitrary function describing the index of refraction in the intermediate layers.

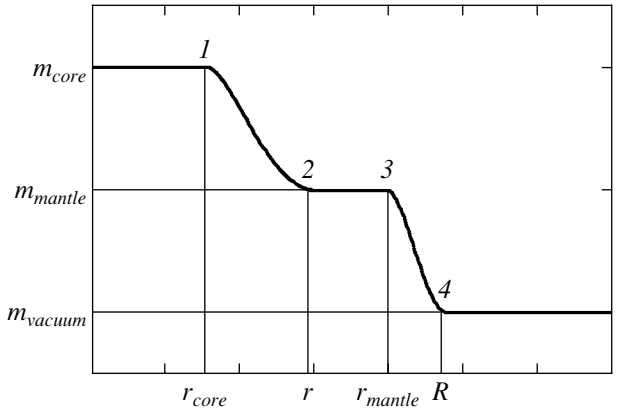

Fig. 2. Radial variations of the index of refraction in an inhomogeneous, layered sphere: the uniform core extends to boundary *1*, intervals *1–2* and *3–4* are transition layers with mixed material (intermediate layers), interval *2–3* is the uniform mantle, and the external medium (vacuum) starts beyond border *4*.

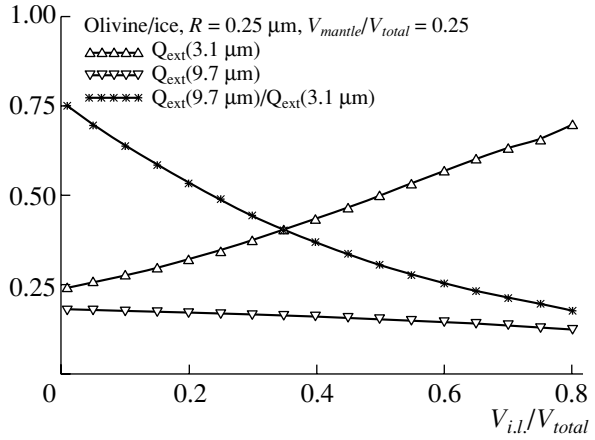

Fig. 3. Dependence of the characteristics of the calculated absorption bands on the width of the intermediate layers. The horizontal axis plots the fractional volume of the intermediate layers, and the vertical axis the values of $Q_{ext}(3.1\ \mu\text{m})$, $Q_{ext}(9.7\ \mu\text{m})$, and $Q_{ext}(9.7\ \mu\text{m})/Q_{ext}(3.1\ \mu\text{m})$.

It was shown in [12] that the extinction and backscattering efficiencies depend only weakly on the profile of the index of refraction in the intermediate layer and on the smoothness of this profile. We present the results of calculations obtained using for the profile of the index of refraction in the intermediate layers

$$\mathcal{M}(\rho) = \sum_{i=0}^{3} \frac{\alpha_i}{\rho^i}, \qquad (2)$$

where the coefficients α_i are defined based on the condition that the index of refraction be continuous at the edges of the mantles:

$$\mathcal{M}(r_{core}) = m_{core}, \quad \mathcal{M}(r) = m_{mantle}, \qquad (3)$$
$$\mathcal{M}(r_{mantle}) = m_{mantle}, \quad \mathcal{M}(R) = M.$$

A schematic of the layered-sphere model is shown in Fig. 1. The homogeneous and inhomogeneous layers are separated by concentric spheres. The two homogeneous layers are formed by a uniform, spherical core that we have taken to consist of a silicate (olivine $Mg_{0.8}Fe_{1.2}SiO_4$) and by a uniform mantle of dirty H_2O ice with admixtures. The optical constants of the silicate and ice were taken from the JPDOC database of optical constants [13]. Between the homogeneous core and mantle is a layer that is spherically inhomogeneous and asymmetric with respect to the center of the grain. This inhomogeneity arises because the surface of a real particle has pits and bumps. The inhomogeneous layer between the core and mantle contains both silicate and ice. The inhomogeneous layer at the boundary with the external medium contains ice and vacuum. The inhomogeneous layers are approximated by intermediate layers in which the index of refraction $m(\rho) = \mathcal{M}(\rho)$ varies in accordance with the formulas given above. Thus, the spatial inhomogeneity of a real grain is represented by the radial inhomogeneity of the model. Figure 2 shows the radial variations of the index of refraction for the case of nonabsorbing grains and an index of refraction for the core that is higher than that for the mantle ($m_{core} > m_{mantle}$).

The optical properties of the *layered spheres* (consisting of either a single or several species of matter) are in good agreement with results of calculations made in the discrete dipole approximation for particles with rough surfaces [9]. The intermediate layers grow as the roughness increases, which, accordingly, increases the volume of matter in them. The degree of grain roughness in the layered-grain model is determined by the parameter $V_{i.l.}/V_{total}$. For smooth particles, $V_{i.l.}/V_{total} = 0$, dust grains with slightly rough surfaces are described by models with $V_{i.l.}/V_{total} < 0.5$.

3. RESULTS AND DISCUSSION

We have considered models for grains with radii ranging from $R = 0.01\ \mu$m to $R = 0.75\ \mu$m, fractional volumes of the mantle from $V_{mantle} = 0.01V_{total}$ to $V_{mantle} = 0.75V_{total}$, and intermediate layers having volumes $V_{i.l.} = (0–0.8)V_{total}$.

When the dust-grain radius is increased, the central wavelengths for both the ice and silicate bands move toward longer wavelengths. For both bands, if R is small ($R \lesssim 0.35\ \mu$m), the full width at half maximum (FWHM) depends only weakly on the size of the grain. When $R \gtrsim 0.5\ \mu$m, FWHM (3.1 μm) for the ice band grows strongly with R. At the same

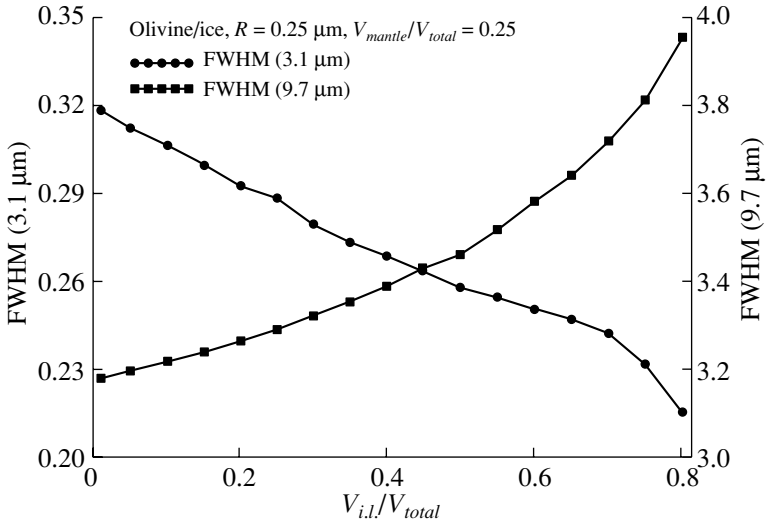

Fig. 4. Dependence of the full width at half maximum of the ice and silicate bands on the fractional volume of the intermediate layers $V_{i.l.}/V_{total}$. The vertical-axis labels on the left and right indicate FWHM (3.1 μm) and FWHM (9.7 μm).

time, the silicate band is broadened only slightly if the total radius of the grains is less than 1 μm. If both of the ratios V_{mantle}/V_{total} (the thickness of the ice mantle) and $V_{i.l.}/V_{total}$ (the small-scale inhomogeneity of the particle surface) increase, λ_0 increases; its lowest value ($\lambda_0 = 2.85$ μm) is obtained for a very thin, almost smooth envelope ($V_{mantle}/V_{total} \approx 0.01$ and $V_{i.l.}/V_{total} \approx 0.01$). The optical depth

$$\tau(\lambda) = N_d \pi R^2 Q_{ext}(\lambda), \qquad (4)$$

in the ice band grows and in the silicate band decreases with increase in either V_{mantle}/V_{total} or $V_{i.l.}/V_{total}$ (Fig. 3). In (4), N_d is the column number density of particles along the line of sight and $Q_{ext}(\lambda)$ is the extinction efficiency. The ratio of the optical depths at the band centers $\tau(9.7\ \mu\text{m})/\tau(3.1\ \mu\text{m})$ decreases in both cases, while the FWHM of the 3.1 μm band decreases and the FWHM of the 9.7 μm band increases (Fig. 4).

When analyzing the 9.7 μm silicate band, we took into account distortion and broadening due to the ice absorption band centered at approximately $\lambda_0 = 12$ μm. Figure 5 shows the wavelength dependence of the extinction efficiency in the silicate band for smooth grains with a mantle and intermediate layers (dashed curves) and without layers (solid curves). We can see that, for the same $Q_{ext}(\lambda_0)$, the layered grains produce bands that are broadened near their centers and shifted toward longer wavelengths; in the absence of intermediate layers, an additional "hump" close to 12 μm appears as the ice mantle grows.

4. COMPARISON WITH OBSERVATIONS

We studied the effect of small-scale asphericity of the dust grains on the properties of these two absorption bands in the spectra of stars and protostellar objects. The observational data were taken from [14–27], and are presented in Fig. 6, which shows the dependence of the observed and model FWHMs of the ice band on the ratio of optical depths at the band centers, $\tau(9.7\ \mu\text{m})/\tau(3.1\ \mu\text{m})$. Figure 6 shows that a 3.1 μm band resembling the observations can be obtained using dust grains with radii $R \lesssim 0.35$ μm and with thin ice mantles ($V_{mantle}/V_{total} \lesssim 0.25$) and narrow intermediate layers ($V_{i.l.}/V_{total} \lesssim 0.25$). In this case, the volume of the intermediate layers must be higher for particles of larger size. For $R \approx 0.01$–0.05 μm and $V_{mantle}/V_{total} \approx 0.01$–$0.05$, the intermediate (inhomogeneous) layers of the dust grains must contain no more than 10% of the total volume in the case of interstellar sources and ~20% in the case of stars observed through molecular clouds. When $R \approx 0.35$ μm, the intermediate layers contain about 25% of the matter in the case of protostars and (25–40)% of the matter in the case of stars.

The observational data show that, for most protostellar objects, $\tau(9.7\ \mu\text{m})/\tau(3.1\ \mu\text{m}) > 1$ (Fig. 6). Such optical-depth ratios can be obtained in the case of thin mantles (narrow intermediate layers, $V_{mantle}/V_{total} \lesssim 0.45$) on spherical grains [6]: $V_{mantle}/V_{total} \lesssim 0.3$ for smooth spheres (this paper) and $V_{i.l.}/V_{total} \lesssim 0.3$ for layered grains (Fig. 5). For stars in molecular clouds, $\tau(9.7\ \mu\text{m})/\tau(3.1\ \mu\text{m}) > 0.3$; such values are obtained for $V_{mantle}/V_{total} \lesssim 0.55$ (spheres), $V_{mantle}/V_{total} \lesssim 0.45$ (smooth spheres), and $V_{i.l.}/V_{total} \lesssim 0.5$ (layered spheres). The values of $Q_{ext}(9.7\ \mu\text{m})/Q_{ext}(3.1\ \mu\text{m}) = \tau(9.7\ \mu\text{m})/\tau(3.1\ \mu\text{m})$ for the case of a grain with a mantle but without intermediate layers (smooth

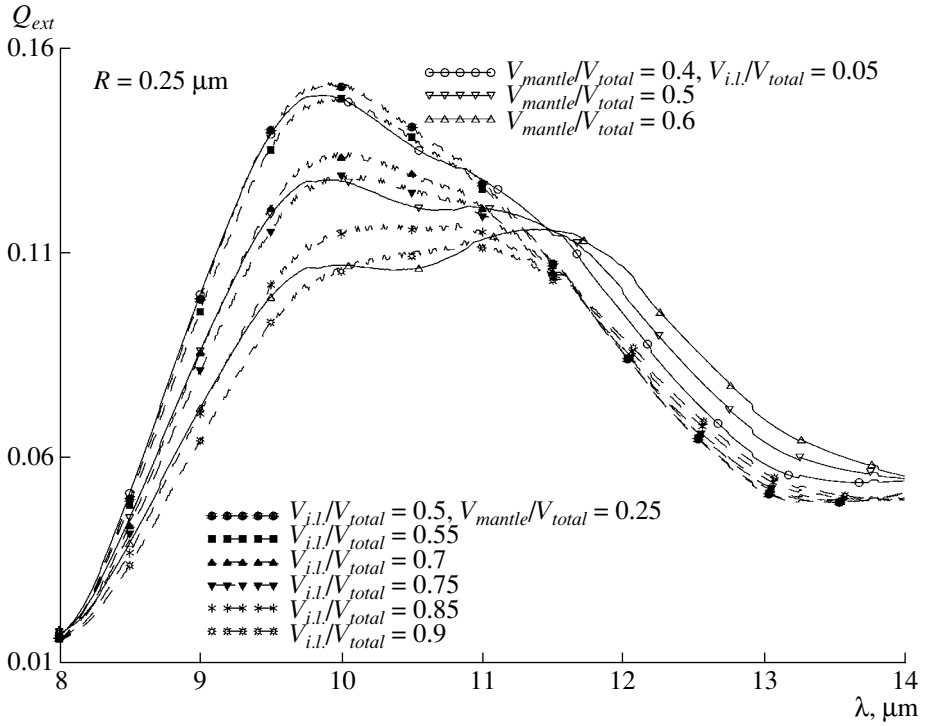

Fig. 5. Wavelength dependence of the extinction efficiency in the silicate band for grains with a mantle but without intermediate layers (solid curves) and for layered grains (dashed curves).

spheres, $V_{i.l.}/V_{total} = 0$) were computed using code for multilayered particles written by N.V. Voshchinnikov. The extinction efficiencies for narrow intermediate layers ($V_{i.l.}/V_{total} \lesssim 0.01$) do not differ much from those for coated grains without intermediate layers, and grains with narrow intermediate layers approach coated grains in a continuous fashion as the thickness of the intermediate layers approaches zero [9].

The profiles of the silicate bands in the spectra of protostellar sources also provide evidence for the presence of thin ice mantles (Fig. 7). We considered observational data provided by Dr. K. Smith in electronic form. The 12 μm ice band is usually weak in protostellar objects, so that it only slightly distorts the 9.7 μm band. For Fig. 7, we selected the five profiles that were most distorted by the 12 μm band; the influence of this band is negligible in the spectra of other protostellar sources (see., e.g., [23]). Figure 5 shows that the shapes of the most distorted profiles can be reproduced only in the presence of a thin ice mantle ($V_{mantle}/V_{total} \lesssim 0.5$). This again confirms that the ice mantles must be thin. This is relevant both for the results of our studies of the 3.1 μm band (see above) and the results of [6], since both ice absorption bands are produced by the same grains. The shapes of the bands in OMC1 IR2, RCW 57, and AFGL 4176 can be explained only by grains with intermediate layers with a fairly large fractional volume ($V_{i.l.}/V_{total} \approx 0.7-0.75$, compare Figs. 5 and 7); this provides evidence for appreciable roughness on the grain surfaces. The silicate absorption band in AFGL 2591 is produced by grains with slightly rough surfaces and fairly thin ice mantles. The absorption band in the spectrum of the protostellar object SVS 13 is produced by dust grains with relatively thick ice mantles ($0.5 \lesssim V_{mantle}/V_{total} \lesssim 0.6$). At the same time, the profile shape shows that the surfaces of the grains may be only slightly rough.

The 12 μm absorption band usually distorts the silicate absorption-band profiles of stars more than those of protostars, suggesting that the grains associated with stars have thicker ice mantles. However, the absorption at the centers of the 12 μm bands never exceed the absorption at the centers of the nearby 9.7 μm band, suggesting that $V_{mantle}/V_{total} \lesssim 0.5$.

5. CONCLUSIONS

Our main results can be summarized as follows.

(1) We have modeled composite dust grains as radially inhomogeneous spheres with intermediate layers in which the index of refraction varies. We considered coated particles with a silicate core and dirty water-ice mantle. It was assumed that the surfaces of the core and the mantle are rough spheres, and that

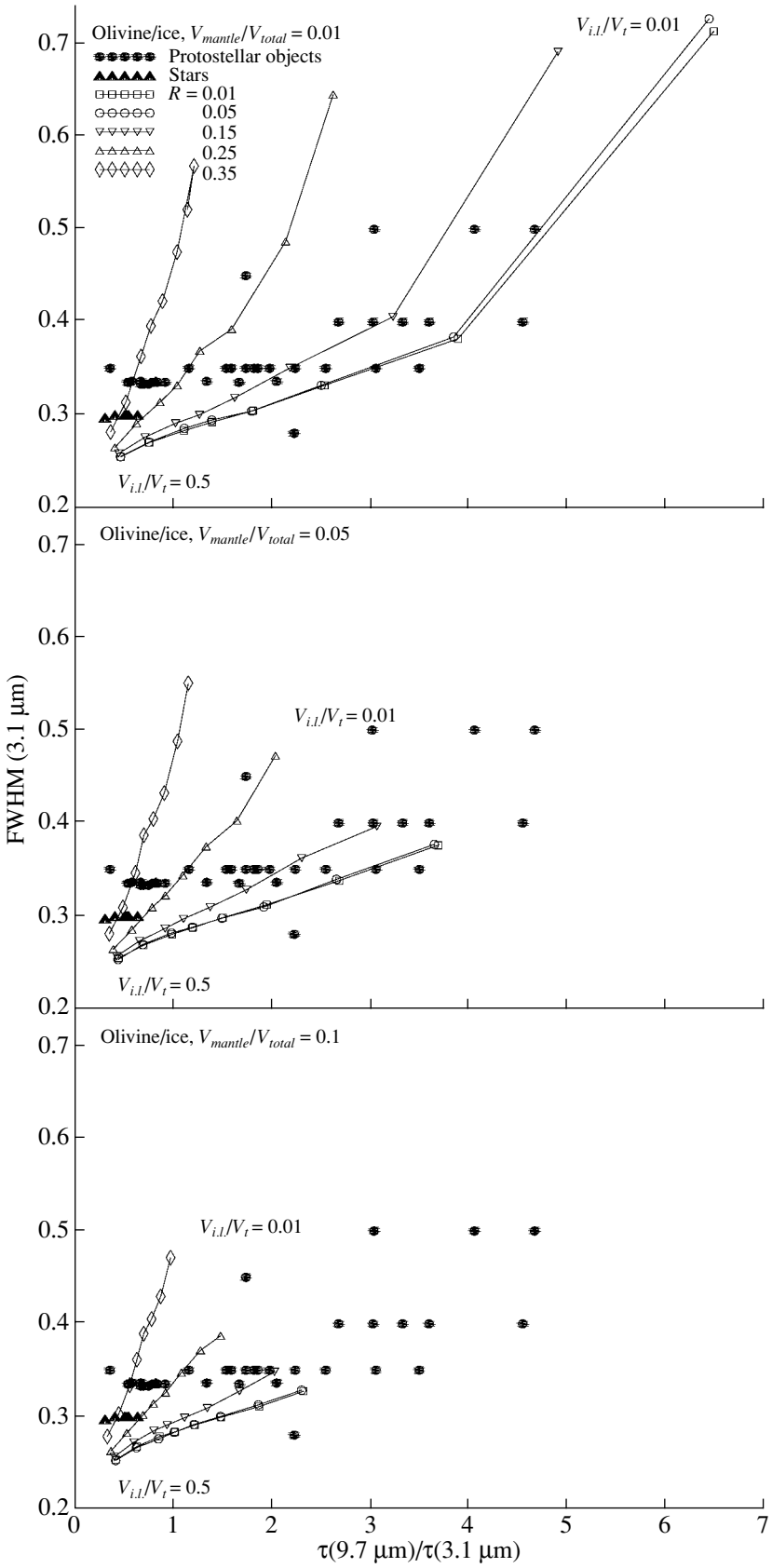

Fig. 6. Dependence of the FWHM of the ice band on the ratio of optical depths at the centers of the silicate and ice bands. We show the effects of variation of the grain size, mantle thickness, and intermediate-layer width.

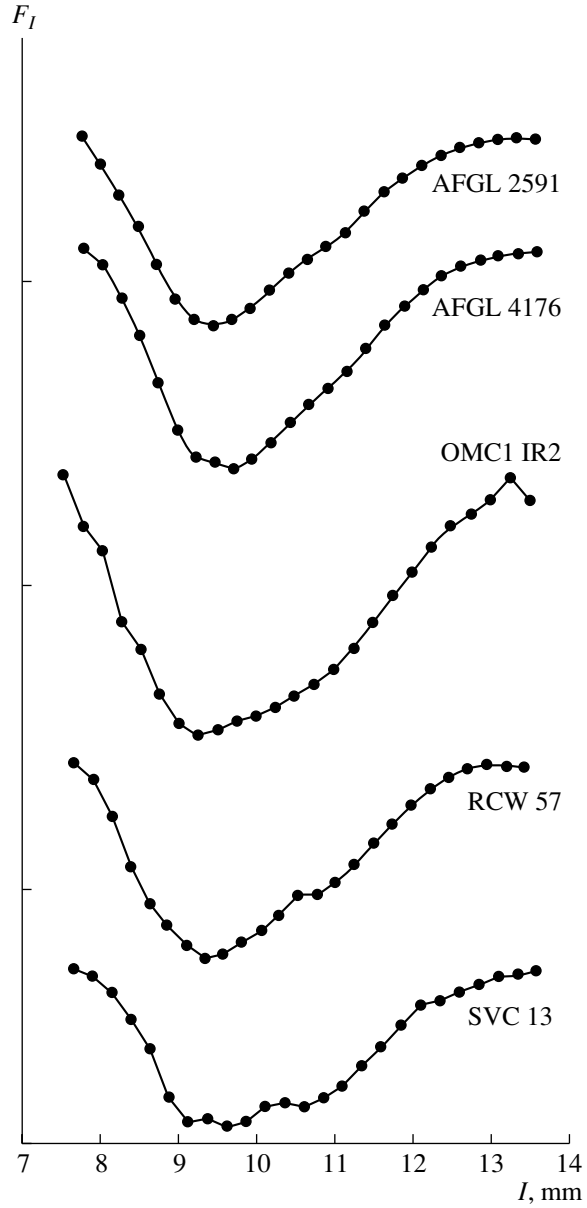

Fig. 7. Profiles of the silicate absorption band in the spectra of protostars.

the matter in intermediate layers close to boundaries is mixed.

(2) We have shown that, when the fractional volume of the intermediate layers is increased, the central wavelength of the ice band λ_0 shifts toward longer wavelengths, while the FWHM of the band decreases. The central wavelength of the silicate band remains virtually unchanged, while the band FWHM increases.

(3) Bands resembling the observed bands can be obtained if the radius of the grains $R \lesssim 0.35$ μm, the fractional volume of the mantle $V_{mantle}/V_{total} \lesssim 0.25$, and (in most cases) the particles have narrow intermediate layers ($V_{i.l.}/V_{total} \lesssim 0.25$). The thickness of the ice mantle and width of the intermediate layers are uncorrelated: a particle may have a thin mantle and narrow intermediate layers (it is almost smooth) or a thin mantle and wide intermediate layers (a refractory silicate core with an abundantly pitted surface and very aspherical shape); in some cases, the grains have a thick ice mantle and narrow intermediate layers (an almost smooth core).

(4) The roughness of the particle surface plays a significant role, broadening the profile near the center, as is observed in the spectra of some sources. The degree of roughness varies significantly from object to object. In some cases, the profile of the 9.7 μm silicate band can be reproduced only by smooth particles or by particles with narrow intermediate layers. In other cases, such as the silicate band in the spectrum of the protostellar source OMC1 IR2, it is necessary to take into account the roughness of the surface and the presence of pitting, which strongly broadens the band near its center.

ACKNOWLEDGMENTS

The author thanks Dr. K. Smith for providing observational data and T.E. Derviz and N.V. Voshchinnikov for valuable advice and remarks during the course of this study. This study was partially supported by the Program "Leading Scientific Schools of Russia" (NSh-1088.2003.2).

REFERENCES

1. D. Whittet, *Dust in the Galactic Environment* (Inst. of Phys., Bristol, 2003).
2. B. Drain and H. Lee, Astrophys. J. **285**, 89 (1984).
3. H. Lee and B. Drain, Astrophys. J. **290**, 211 (1985).
4. Th. Henning and R. Stognienko, Astron. Astrophys. **280**, 609 (1993).
5. J. O'Donnell, Astrophys. J. **437**, 262 (1994).
6. T. Zinov'eva, Astron. Astrophys. Trans. **22**, 51 (2003).
7. V. Farafonov, N. Voshchinnikov, and V. Somsikov, Appl. Opt. **35**, 5412 (1996).
8. J. Greenberg, Plenum Press, 7 (1980).
9. T. V. Zinov'eva, Opt. Spektrosk. **97**, 462 (2004) [Opt. Spectrosc. **97** (3), 433 (2004)].
10. A. Perelman, Appl. Opt. **35**, 5452 (1996).
11. A. Ya. Perel'man and T. V. Zinov'eva, Opt. Spektrosk. **92**, 468 (2002) [Opt. Spectrosc. **92**, 425 (2002)].
12. A. Ya. Perel'man and T. V. Zinov'eva, Opt. Atmos. Okeana **14**, 669 (2001).
13. T. Henning, V. B. Il'in, N. A. Krivova, *et al.*, Astron. Astrophys., Suppl. Ser. **136**, 405 (1999).
14. A. Boogert, A. Tielens, C. Ceccarelli, *et al.*, Astron. Astrophys. **360**, 683 (2000).
15. J. Bowey, A. Adamson, and D. Whittet, Mon. Not. R. Astron. Soc. **298**, 131 (1998).

16. T. Brooke, K. Sellgren, and T. Geballe, Astrophys. J. **517**, 883 (1999).
17. E. Dartois and L. d'Hendecourt, Astron. Astrophys. **365**, 144 (2001).
18. E. Gibb, D. Whittet, W. Schutte, *et al.*, Astrophys. J. **536**, 347 (2000).
19. E. Gibb, D. Whittet, and J. Chiar, Astrophys. J. **558**, 702 (2001).
20. J. H. Hough, D. C. B. Whittet, S. Sato, *et al.*, Mon. Not. R. Astron. Soc. **241**, 71 (1989).
21. M. E. Palumbo, T. R. Geballe, and A. G. Tielens, Astrophys. J. **479**, 839 (1997).
22. Y. Pendleton, A. Tielens, A. Tokunaga, and M. Bernstein, Astrophys. J. **513**, 294 (1999).
23. C. Smith, C. Wright, D. Aitken, *et al.*, Mon. Not. R. Astron. Soc. **312**, 327 (2000).
24. T. Teixeira and J. Emerson, Astron. Astrophys. **351**, 292 (1999); **351**, 303 (1999).
25. A. Tielens, D. Wooden, L. Allamandola, *et al.*, Astrophys. J. **461**, 210 (1996).
26. D. Whittet, M. Bode, A. Longmore, *et al.*, Macmillan J. **102**, 218 (1983).
27. D. Whittet, R. Smith, A. Adamson, *et al.*, Astrophys. J. **458**, 363 (1996).

Translated by L. Yungel'son

Astronomy Reports, Vol. 49, No. 5, 2005, pp. 425–430. Translated from Astronomicheskiĭ Zhurnal, Vol. 82, No. 5, 2005, pp. 474–480.

Geometry of Solar Prominences and Magnetic Fields in the Corona

A. M. Zagnetko, B. P. Filippov, and O. G. Den

Institute of Terrestrial Magnetism, Ionosphere, and Radio Wave Propagation, Troitsk, 142190 Russia

Received May 18, 2004; in final form, December 3, 2004

Abstract—The spatial location of the surface at which most of the prominence mass is concentrated is compared with the location of the "neutral surface" where $B_r = 0$ (B_r is the magnetic field) calculated in a potential approximation using photospheric data. More than fifty prominences (filaments) observed in 1999–2003 are studied. The vertical deviations of the prominences (predominantly toward the west) correspond well to the inclination of the neutral surface. The results provide evidence for the magnetic support of filaments of opposite polarities (the magnetic-rope model). © *2005 Pleiades Publishing, Inc.*

1. INTRODUCTION

Quiescent prominences (filaments) frequently take the form of thin ribbons standing on end, or curtains [1, 2]. The typical thickness of the ribbons (5–6 Mm) is much smaller than both their height (30–35 Mm) and their length along the solar surface (>200 Mm). If the surface on which the prominence material is concentrated were strictly vertical, filaments extending from north to south would display their narrowest apparent widths at the central meridian when rotating with the Sun. However, the study of [1] showed that most filaments display their minimum width in the eastern hemisphere, i.e., they are inclined toward the west, in the direction of the solar rotation. d'Azambuja and d'Azambuja [1] determined that the median inclination of the prominences is about 10°. In [3], the prominences were found to be tilted toward the weaker magnetic field, leading Rust [4] to suggest that the prominence inclinations were associated with the inclinations of the magnetic loops of asymmetrical sources. Using the model of Kippenhahn and Schluter [5], in which the prominence is supported at a point where the photospheric magnetic-field lines "sag," the observed tilt was explained as a shift with height of such a dip in the magnetic lines due to two rows of vertical antiparallel dipoles [6]. This explanation can no longer be considered valid, since it is now known that quadrupolar magnetic-field lines with dips are not typical for most prominences. Our calculations of the magnetic fields in the corona and near prominences show an absence of such dips. We compare the prominence inclination with that of the surface $B_r = 0$ (where B_r is the radial magnetic field), which can be considered a "neutral surface" in the corona, by analogy with the neutral lines in the photosphere. The equilibrium conditions for electric currents flowing opposite to the currents in the model of Kippenhahn and Schluter [5] is possible on this neutral surface. Models with such opposite currents in prominences are called inverse-polarity models [7, 8].

The locations of prominences on the Sun reflect their magnetic origin. Comparisons with maps of the photospheric longitudinal magnetic field show that filaments are always located above lines separating opposite polarities of the radial field [9–12]. A belt extended along the polarity-dividing line (neutral line) forms an inversion zone that corresponds to the filament channel. A simple potential extrapolation of the photospheric field yields an arcade of loops in this inversion zone. The magnetic-field lines should be horizontal directly above the inversion line and predominantly transverse to this line. In fact, the field in the filament channel is much more complex. Zeeman [4, 13–16] and Hanle [17, 18] effect measurements of the magnetic fields in prominences have shown that, as a rule, the field in the channel is horizontal, but directed nearly along the filament axis and polarity-inversion line. The angle to the axis is 25°, on average. Moreover, the component transverse to the axis is predominantly opposite to that calculated in the potential approximation.

The classical Kippenhahn–Schluter and Kuperus–Raadu models are fairly schematic, and are concerned only with the principle of equilibrium, taking into account the main forces responsible for the support of the prominence. In particular, these models are two-dimensional, and neglect components directed along the filament axis, whereas the magnetic fields in prominences are in reality directed predominantly along the axis. However, this component B_l does not appreciably affect the equilibrium, since, owing to its geometry, the total filament current J can be directed solely along the axis, so that $\mathbf{J} \times \mathbf{B}_l = 0$. Of course, the axial component must be taken into account if we wish to clarify the

1063-7729/05/4905-0425$26.00

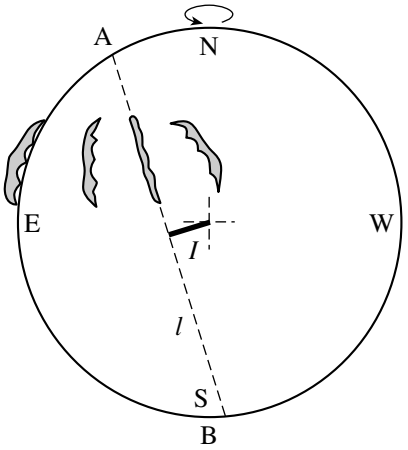

Fig. 1. Schematic of the passage of a filament through the solar disk.

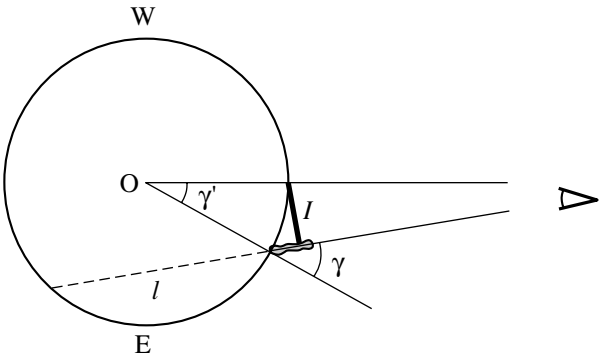

Fig. 2. Schematic of the position of a filament displaying its minimum width. The plane of the sky is perpendicular to the chord AB.

correspondence between the magnetic field lines in a model and the threads in a filament. Adding the axial field shifts the magnetic field lines above the dividing line in a simple arcade. Closed circular magnetic field lines are transformed into three-dimensional spirals winding on a cylindrical surface extended along the filament axis. The three-dimensional magnetic field in inverse-polarity models takes the form of a rope of magnetic field lines inside a simple arcade. Since the plasma parameter β is small, the field in the flux rope must be close to force-free. Among the various flux-rope models for filaments [19–21], the model of Aulanier *et al.* [22] provides the most accurate correspondence to the observed structures. We do not aim here to obtain a precise agreement between the calculated magnetic field and the fine structure of observed prominences. We wish to obtain a general approximation for the prominence structure based on a surface tilted at some angle to the vertical line and a comparison of the positions of this surface and of the magnetic neutral surface. We disregard the magnetic fields of coronal currents. Of course, these fields can significantly affect the distribution of the matter in prominences, although the general structure is probably determined by the photospheric field.

2. CALCULATION TECHNIQUE AND ORIGINAL DATA

We estimated the inclinations of the prominence planes to a vertical line dropped to the solar surface using the method of d'Azambuja and d'Azambuja [1], which they applied to a large number of prominence measurements obtained in the 1940s. We can determine the prominence inclination γ if we can measure I—the distance between the center of the disk and the line AB passing along the filament axis when the filament's projection onto the disk takes on its minimum width (Fig. 1). It is evident that we will observe the minimum width when the prominence plane contains the line of sight (Fig. 2). This plane forms a circular cross section l of the spherical solar surface. Since the secant plane makes the same angle to the vertical radius everywhere on the circumference l, it is sufficient to determine the central angle γ', which does not differ from the angle γ by more than 0.25°. Within the required accuracy, we can assume that the distance I is equal to the length of the arc traced on the solar sphere between the circle l and the line of sight, directed to the disk center. Then, $\gamma = I/R_\odot$, where $R_\odot$ is the solar radius.

We determined the positions and geometries of the prominences using H_α filtergrams from the site of the Big Bear Solar Observatory (http://www.bbso.njit.edu). We first selected images with large prominences displaying developed but not excessively irregular structures. For this purpose, we examined successive images tracing the prominence's evolution over 7–10 days, enabling us to verify that the prominence did not considerably change its shape. We selected fifty filaments among the Hα images obtained at three different observatories (Big Bear, Kanzelhoehe, and Yunnah) within intervals of several hours to a day in 1999, 2002, and 2003. We mainly selected prominences located near the equator (within 50° in latitude) and near the zero meridian, since the errors in the sizes of polar objects increase toward the edge of the corresponding sphere, and the prominence orientation becomes predominantly east–west when the prominence moves away from the equator, preventing foreshortening with the line of sight along the surface of the prominence rotating with the Sun. Typical observations are presented in Fig. 3.

Unfortunately, coronal magnetic-field measurements are not currently technically feasible, except for a few indirect estimates. At the photosphere, beyond

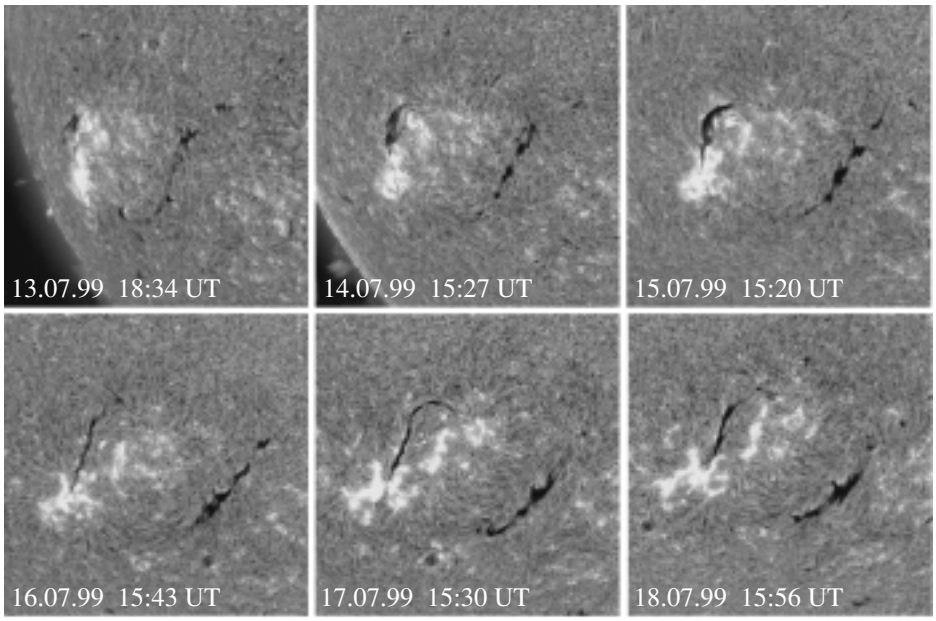

Fig. 3. Hα filtergrams for the passages of two filaments across the solar disk (Big Bear Observatory). The left and right filaments are numbered 4 and 2 in the table, respectively.

the regions of strong magnetic fields, Zeeman effect measurements determine only the field component along the line of sight. The magnetic field in the corona must be calculated using these data and some physical assumptions.

To a first approximation, we can assume that the coronal magnetic field is potential. Strong large-scale electrical currents are required to appreciably change the potential of the magnetic field. The potential field determines the general topology of active regions and the locations of flares, prominences, and other active objects. However, the fields in the prominences themselves and in their immediate vicinity are far from potential. Ropes and bundles of thin spiral threads are often observed in the fine structure of filaments and prominences, indicating the presence of strong coronal electric currents, although the potential field of the photospheric sources remains the dominant field governing the overall behavior and morphology of the prominences. This is supported by the fact that prominences (filaments) very accurately follow lines separating opposite polarities of the photospheric field.

There are two well-known methods for solving the Neumann boundary problem for the calculation of a potential magnetic field with specified boundary conditions. The first employs the integral form of the potential using Green functions, while the second employs expansions in series of eigenfunctions satisfying the Laplace equation. Fourier series expansions and expansions in series of the associated Legendre polynomials are most often used. The boundary conditions determine the expansion coefficients. This method is the best choice for calculating the magnetic field of the Sun as a whole. The Green-function method is preferable for calculating the magnetic field of a comparatively small region in the corona, since it provides high spatial resolution at the cost of a moderate increase in computation time [23].

To calculate the potential fields near filaments, we used the distribution of the field over a rectangular region whose size was appreciably larger than the filament height. At the same time, the sizes of the regions were not too large, and we could neglect the sphericity of the surface and assume the boundary is planar. The field component normal to the boundary surface is used to solve the Neumann problem, whereas the magnetographic measurements supply

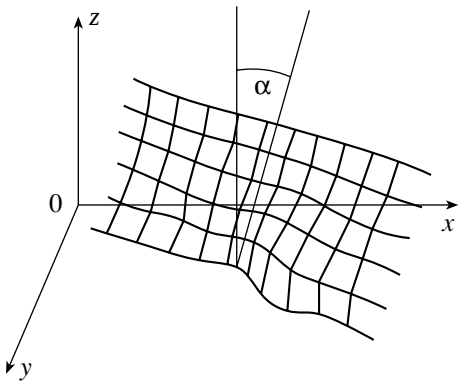

Fig. 4. Neutral surface calculated for the region of filament 2 in the table; α is the vertical deviation angle for this surface.

Vertical deviation angles for prominences and neutral surfaces

No.	Date	Prominence center coordinates, degrees	Vertical deviation angles for neutral surfaces α, degrees	Vertical deviation angles for prominences γ, degrees
1	07.07.99	S 45 E 45	15–60	20–40
2	15.07.99	S 30 E 30	56	30
3	15.07.99	N 40 E 45	10–30	20–30
4	15.07.99	S 30 E 35	48	30
5	16.07.99	N 50 E 25	24	20
6	26.04.00	S 30 E 30	17	20
7	02.05.00	N 30 E 30	34	30
8	04.03.02	S 10 E 20	−10	5
9	08.03.02	S 00 E 05	16	15
10	05.05.03	N 20 E 20	33	25
11	04.06.03	S 30 E 25	29	25
12	10.06.03	S 60 E 40	53	35
13	10.06.03	N 40 E 50	−5	10
14	10.06.03	N 45 E 60	12	20
15	13.06.03	N 50 E 30	21	20

us with the component parallel to the line of sight, which does not coincide with the normal component when our region is far from the center of the solar disk. In such cases, the normal component is first calculated from the detected inclined component via integral iterations [24].

We used SOHO/MDI magnetograms to calculate the magnetic field. Matching the Hα image and magnetogram and correcting for the solar rotation when necessary (i.e., when we could not use a magnetogram and image obtained at the same time), we determined the coordinates of the region containing the prominence in the Hα image. We then used the selected region of the magnetogram as the boundary condition for the numerical computation of the three components of the coronal magnetic field and of the profiles $B_r = 0$ for various altitudes above the photosphere, which provides us with a three-dimensional image of the neutral surface (Fig. 4). We choose the local coordinate frame so that the z axis was vertical, i.e., $B_r = B_z$. The computations were performed to z values corresponding to the mean prominence height, or until a clear neutral line was distinguished. When we had accumulated sufficient data containing the coordinates of the $B_z = 0$ lines at various heights, we found the angle α of the neutral surface created by these lines to a vertical line dropped to the solar surface.

Let us say a few words about the measurement and computational errors. The main sources of error in the inclination of the prominence surface are changes in the shapes and sizes of the prominences during their passage across the disk; the complex shapes of the surfaces, which could not always be approximated well by a single plane; the lack of observations for a required time; and the limited resolution of the images used. Only the last type of errors can be accurately estimated, while the others can be estimated only statistically. One pixel in the image corresponds to 0.7 Mm ($1''$) on the solar surface, although the quality of typical images was at least twice as poor. Since the mean thickness of the prominences is about 6 Mm, the errors in the prominence inclinations are about 25%, at best.

The errors in the calculated inclinations of the neutral surfaces are determined by the errors in the original data (the saturation of the magnetograms, limited resolution, sphericity of the surface), the errors in the computed magnetic-field components (the accuracy was specified to be one percent), and errors related to deviations of the neutral surface from its mean plane. The final error in the inclination of the neutral surface is about 20%.

3. RESULTS AND DISCUSSION

About 70% of the fifty prominences considered displayed vertical deviations in the direction of the

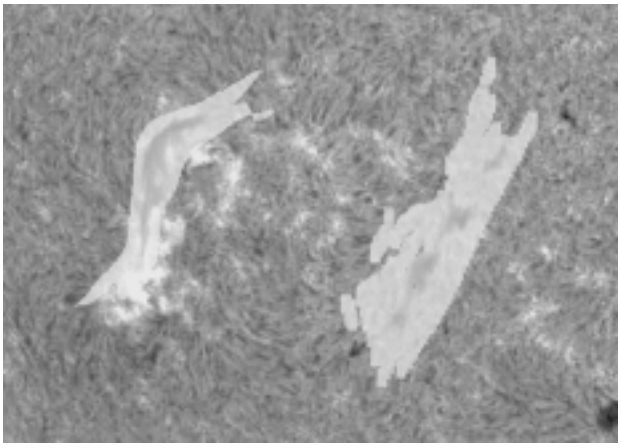

Fig. 5. Profiles of neutral surfaces and their superpositions on the corresponding Hα filtergram (Big Bear Observatory). The light shade shows the projections of the neutral surfaces onto the plane of the sky against the background of the chromosphere; the filaments appear through them as darker formations. Filaments 4 (left) and 2 (right) in the table are presented. The neutral-surface profile for filament 2 is shown in Fig. 4.

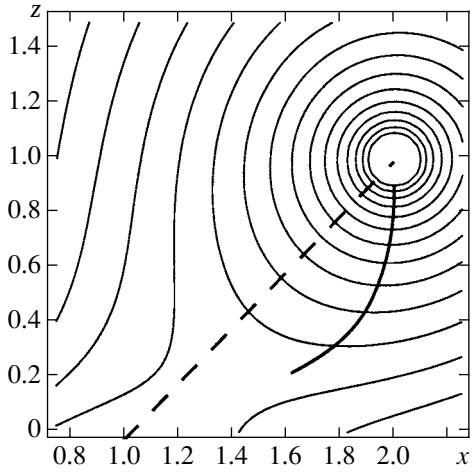

Fig. 6. Field lines of a straight current in equilibrium above a conducting plane placed in the field of a vertical linear dipole. The dashed curve shows the projection of the neutral surface of the dipole field; the thick solid curve indicates the magnetic sags where the prominence plasma can accumulate.

solar rotation (toward the west). The deviation angles varied from $-7°$ to $40°$, with the relative errors in these estimates being no less than 25%. In general, the results agree with those presented in [1], though the statistics used in [1] are considerably better than ours. Comparing the results, we can see that our data (see the table) show larger prominence inclinations, on average. This may be due to the fact that, in contrast to d'Azambuja and d'Azambuja [1], who analyzed all available observations within a certain period, we studied primarily pronounced, large prominences near the central meridian, whose relatively large widths were probably associated with considerable vertical deviations. Thus, the discrepancy between our results and those of [1] can likely be attributed to selection effects.

The table presents the measured vertical deviations for fifteen prominences and the calculated inclinations for the neutral surfaces of the corresponding potential magnetic fields. We can see that the inclinations of the prominences and neutral surfaces coincide within the errors, except for filaments 8 and 13. This indicates that the prominence material is mainly concentrated at the magnetic neutral surface. Figure 5 shows a filtergram with the projections of neutral surfaces superposed onto one of the regions with filaments studied. Segments of neutral surfaces extending from the photosphere to heights of $\sim$30 Mm are projected onto the plane of the sky. These projections are superposed on the Hα filtergrams and are shown by a lighter shade. The filaments appear through them as darker formations. As a rule, the filaments are located within the edges of the projections of the neutral surfaces, and partially reproduce their shapes. We would not expect better correspondence, since the potential approximation describes only the most general features of the field, as we noted above.

As we noted in the Introduction, the observed prominence inclinations were explained in [6] as a shift in the height of a "sag" in the magnetic-field lines of two rows of vertical antiparallel dipoles with different moments. Though such a quadrupolar magnetic configuration seems quite plausible for filaments located between two active regions, the calculations of the potential fields based on the original magnetograms show no sags of the magnetic-field lines at the filaments.

A dense plasma cannot be stable at the apex of an arch of magnetic-field lines. This is not the case if a sufficiently strong electric current flows in the proper direction. Such a current can provide a stable equilibrium at the arch apex (taking into account the interaction with induction currents in the photosphere). As we noted above, this idea forms the basis for inverse-polarity models for the magnetic equilibrium of filaments. Direct measurements and indirect estimates of the magnetic fields in prominences provide growing evidence for this type of equilibrium.

The presence of a strong current in the corona reduces the support of the prominence against the equilibrium of this current. When the weight of the plasma is small compared to the electromagnetic forces, equilibrium can easily be realized for the relevant geometry of the current magnetic field lines. Figure 6 shows the magnetic field lines of force for a straight current in equilibrium above a conducting

plane in the field of a vertical linear dipole. Such a filament model was considered in [25]. The linear dipole (two neighboring linear currents) is located beneath the photosphere at the point $x = 0$, $z = -1$. The dashed curve in Fig. 6 shows the position of the neutral surface of the dipole field in the absence of currents. The coronal current creates its own image in the photosphere, inducing currents that prevent the penetration of the field of the coronal current into the solar interior. The thick solid curve shows the locus of the upward curvature of the magnetic-field lines, i.e., the locus of sags in the magnetic field. These sags can accumulate and confine the prominence plasma. The curve does not coincide with the projection of the neutral surface, although it approaches it. Thus, the prominence will have an inclination similar to that of the neutral surface for a source located beneath the photosphere.

4. CONCLUSIONS

We have studied the geometries of solar prominences (filaments) and their relation to the structure of the magnetic field generated in the corona by subphotospheric sources (currents). Our analysis of about forty filaments supports previous conclusions that large, quiescent filaments at moderate latitudes display systematic vertical deviations toward the west. The surface at which the prominence material is concentrated is close to that passing through the apices of arches of the potential magnetic-field lines (the surface $B_r = 0$, or the neutral surface) calculated using photospheric magnetograms.

We can construct a detailed map of the distribution of the material for this magnetic configuration only if we adopt certain fairly arbitrary assumptions. At the same time, it is clear that the apices of arches should somehow be distinguished, since they are places of equilibrium of the currents. Our study shows that the prominence matter is, indeed, concentrated near the surface passing through the apices of the magnetic arches—the neutral surface. Thus, the geometric form of the prominences and their vertical deviations correspond to the structures of magnetic fields generated in the corona by subphotospheric currents. This correspondence supports the inverse-polarity model for quiescent prominences.

ACKNOWLEDGMENTS

This work was supported by the Russian Foundation for Basic Research (project no. 03-02-16093) and the Federal Science and Technology Program in Astronomy.

REFERENCES

1. M. d'Azambuja and L. d'Azambuja, Ann. Observ. Paris, Meudon **6**, Fasc. VII (1948).
2. B. Rompolt, Bull. Harv. Obs. **14**, 37 (1990).
3. U. Becker, Z. Astrophys. **40**, 65 (1956).
4. D. M. Rust, NCAR Cooperative Thesis, No. 6 (Univ. of Colorado, Boulder, 1966).
5. R. Kippenhahn and A. Schluter, Z. Astrophys. **43**, 36 (1957).
6. G. Godoli, S. Motta, V. Sciuto, and R. A. Zappala, in *Skylab Solar Workshop*, Ed. by G. Righini; Oss. Mem. Oss. Astrofis. Arcetri **104**, 204 (1974).
7. M. Kuperus and M. A. Raadu, Astron. Astrophys. **31**, 189 (1974).
8. E. R. Priest, *Dynamics of Quiescent Prominences*, Ed. by V. Ruzdjak and E. Tandberg-Hanssen (Springer-Verlag, New York, 1990); Lect. Notes Phys. **363**, 150 (1990).
9. H. W. Babcock and H. D. Babcock, Astrophys. J. **121**, 349 (1955).
10. R. F. Howard and J. W. Harvey, Astrophys. J. **139**, 1328 (1964).
11. S. F. Smith and H. E. Ramsey, Sol. Phys. **2**, 158 (1967).
12. P. S. McIntosh, Rev. Geophys. Space Phys. **10**, 837 (1972).
13. B. A. Ioshpa, *Structure and Development of Solar Active Region*, Ed. by K. O. Kipenheuer (1968), p. 261.
14. I. S. Kim, V. Yu. Klepikov, S. Kuchmi, *et al.*, Soln. Dannye, No. 1, 75 (1988).
15. I. S. Kim, V. Yu. Klepikov, S. Kuchmi, *et al.*, Soln. Dannye, No. 5, 77 (1988).
16. I. S. Kim, *Dynamics of Quiescent Prominences,* Ed. by V. Ruzdjak and E. Tandberg-Hanssen; Lect. Notes Phys. **363**, 49 (1990).
17. J.-L. Leroy, *Dynamics and Structure of Quiescent Solar Prominences,* Ed. by E. R. Priest (1982), p. 77.
18. V. Bommier, E. Landi degl'Innocenti, and J.-L. Leroy, Solar Phys. **154**, 231 (1994).
19. A. A. van Ballegooijen and P. C. H. Martens, Astrophys. J. **343**, 971 (1989).
20. P. A. Isenberg, T. G. Forbes, and P. Demoulin, Astrophys. J. **417**, 368 (1993).
21. T. G. Forbes and E. R. Priest, Astrophys. J. **446**, 377 (1995).
22. G. Aulanier, P. Demoulin, L. van Driel-Gesztelyi, *et al.*, Astron. Astrophys. **335**, 309 (1998).
23. O. G. Den, O. E. Den, E. A. Kornitskaya, and M. M. Molodenskii, Soln. Dannye, No. 1, 97 (1979).
24. O. G. Den, Pis'ma Astron. Zh. **28**, 393 (2002) [Astron. Lett. **28**, 345 (2002)].
25. M. M. Molodenskii and B. P. Filippov, Astron. Zh. **64**, 1079 (1987) [Sov. Astron. **31**, 564 (1987)].

Translated by V. Badin